THÈSE

En vue de l'obtention du

DOCTORAT DE L'UNIVERSITÉ DE TOULOUSE

Délivré par :

Institut National Polytechnique de Toulouse (Toulouse INP)

Discipline ou spécialité :

Génie Électrique

Présentée et soutenue par :

Mme HUONG THAO LE LUONG

le jeudi 18 octobre 2018

Titre :

Optimal Design of Modular High Performance Brushless Wound Rotor Synchronous Machine for embedded systems

---

Ecole doctorale :

Génie Electrique, Electronique, Télécommunications (GEET)

Unité de recherche :

Laboratoire Plasma et Conversion d'Energie (LAPLACE)

Directeur(s) de Thèse :

MME CAROLE HENAUX

M. FREDERIC MESSINE

Rapporteurs :

M. FRÉDÉRIC GILLON, ECOLE CENTRALE DE LILLE

M. JEAN-FREDERIC CHARPENTIER, ECOLE NAVALE

Membre(s) du jury :

M. PASCAL BROCHET, ECOLE CENTRALE DE LILLE, Président

M. FREDERIC MESSINE, INP TOULOUSE, Membre

Mme CAROLE HENAUX, INP TOULOUSE, Membre

Mme SONIA CAFIERI, ECOLE NATIONALE DE L'AVIATION CIVILE, Membre

To my family and my husband

and most specially to my mother Luong Thi.

Acknowledgement

The work presented in this thesis has been carried out at the group of GREM3, LAPLACE laboratory - INP Toulouse, between December 2015 and November 2018 in a research project with Mitsubishi Electric R&D Centre in Europe.

I would like to thank my supervisor, MdC. Carole HENAUX, for providing me the opportunity to do this thesis and for her guidance, help and encouragement during my study. My deepest thanks to my co-supervisor, Prof. Frédéric MESSINE, for always helping me when in need and getting me out of tough situations. Thanks to both of you for your dedication during these years, for having time for me. I also wish to thank Dominique HARRIBEY for helping me to develop the prototype machine always with a smile on his face.

I really appreciate the support I got from Guilherme MARIANI, Stefan MOLLOV, and Nicolas VOYER. I would like to thank MERCE France for its financial support.

I would like to thank all my colleagues from the GREM3 group and my friends, especially Sarah TOUHAMI for your friendship and all your support. You inspired me during difficult times of the thesis.

I am grateful to the human manager, Magali BRANCHEREAU, the secretary, Marie PLANTARD, of MERCE-France and the secretary, Valerie SCHWARZ, of LAPLACE laboratory for your indirectly contribution to my achievement.

Lastly, but not least, I would like to express my deeply gratitude towards my parents and my husband. You always accompany me in the moments of joy and difficulty with your love. This thesis is dedicated to you.

Thank you very much!

LE LUONG Huong Thao

Abstract

This thesis is dedicated to the design and the optimization of modular brushless wound rotor synchronous machine for embedded systems. This machine is constructed based on POKI-POKI™ structure with integrated drive electronics.

Finite element analysis based optimization becomes more popular in the field of electrical machine design because analytical equations are not easily formalized for the machines which have complicate structures. Using electromagnetic analysis to comparatively study different modular brushless wound rotor synchronous machines and therefore, to select the structure which offers the best fault tolerant capability and the highest output performances. Firstly, the fundamental winding factor calculated by using the method based on voltage phasors is considered as a significant criterion in order to select the numbers of phases, stator slots and poles. After that, 2D finite element numerical simulations are carried out for a set of 15 machines to analyze their performances. The simulation results are then compared to find an appropriate machine according to torque density, torque ripple and machine efficiency. The 7-phase/7-slot/6-pole machine is chosen and compared with a reference design surface-mounted permanent magnet synchronous machine in order to evaluate the interesting performance features of the wound rotor synchronous machine.

In the second design stage, this machine is optimized by using derivative-free optimization. The objective is to minimize external volume under electromagnetic, thermal and mechanical constraints. Given that an accurate finite element analysis for machine performance takes a long time. Moreover, considering that the average torque can be obtained by simulating the model with only four rotor positions instead of one electric period, optimization strategy is proposed to reduce computational time and therefore, obtain a fast convergence ability by defining relaxed problems which enable minimizing the external volume of the machine under only several constraints such as average torque, torque ripple and copper losses. By testing relaxed problems, two different optimization methods (NOMAD and *fmincon)* are compared in order to select an appropriate method for our optimization problem. Using NOMAD method based on Mesh Adaptive Direct Search, we achieve optimal results which satisfy all of the constraints proposed.

In the third design stage, all constraints are validated by 3D electromagnetic and thermal simulations using finite element and computational fluid dynamics methods. The 3D results show that the average torque obtained is lower than the desired value. By increasing the length of the machine, a new corrected machine is thus obtained. It can be observed that the iron losses obtained in 3D are higher than that in 2D due to the leakage flux in the end-winding. Then, the machine temperature is analyzed by using ANSYS Fluent. Note that the surface temperature is higher than that calculated in the optimization and the coil temperature is 8.48°C higher than the desired value (105°C). However, some dissipation by the

shaft and the bearings of the machine are expected to reduce the machine temperature. Finally, a machine prototype is built and some experimental tests are carried out. The results show that the electromotive force has a similar waveform compared to 3D prediction and the difference of the measured and predicted maximum static torques is small.

Keywords:

Wound rotor synchronous machine, modular structure, fractional slot concentrated winding, finite element method, numerical optimization, mesh adaptive direct search algorithm, NOMAD solver, *fmincon* solver, 3D electromagnetic simulation, 3D thermal analysis, computational fluid dynamics method.

Résumé

Cette thèse est dédiée à la conception optimale de la machine synchrone à rotor bobiné modulaire sans balais pour les systèmes embarqués. Cette machine est basée sur une structure POKI-POKI™ développée par Mitsubishi Electric Coopération avec les convertisseurs de puissance intégrée pour augmenter la capacité de tolérance aux défauts.

L'analyse électromagnétique est utilisée pour étudier les différentes machines synchrones à rotor bobiné et donc, pour sélectionner la structure qui offre la meilleure tolérance aux défauts et les performances les plus élevées. D'abord, le choix des nombres de phases, d'encoches et de pôles est un point critique. Ensuite, quelques machines sont analysées et comparées selon les critères tels que la densité de couple, le rendement, l'ondulation de couple. La machine avec 7 phases, 7 encoches et 6 pôles est alors choisie. Cette machine est ensuite comparée à la machine synchrone à aimant permanent monté en surface. Le résultat démontre que la machine synchrone à rotor bobiné modulaire sans balais possède le potentiel de remplacer la machine synchrone à aimant permanent dans notre application parce qu'elle présente des performances similaires avec une capacité de tolérance aux défauts élevée.

Dans un second temps, une fois la structure 7phases/7encoches/6pôles choisie, cette machine est optimisée en utilisant NOMAD (qui est un logiciel d'optimisation de boîte noire) afin de minimiser le volume externe sous les contraintes électromagnétiques, thermiques et mécaniques. Comme ce problème d'optimisation est extrêmement difficile à résoudre, quelques relaxations ont été effectuées pour tester les différents algorithmes d'optimisation : *fmincon (*de Matlab) et NOMAD. Nous remarquons que NOMAD est plus efficace que *fmincon* pour trouver des solutions à ce problème de conception où certaines contraintes sont calculées par des simulations numériques (ANSYS Maxwell ; code éléments finis). En utilisant la méthode NOMAD basée sur l'algorithme Mesh Adaptive Direct Search, nous obtenons des résultats optimaux qui satisfont toutes les contraintes proposées.

Il est nécessaire de valider ce design optimisé en vérifiant toutes les contraintes par des simulations électromagnétiques et thermiques en 3D. Les résultats montrent que le couple moyen obtenu par la simulation en 3D est inférieur à la valeur souhaitée. Par conséquent, en augmentant la longueur de la machine, une nouvelle machine corrigée est ainsi obtenue. Nous observons que les pertes de fer obtenues en 3D sont plus élevées qu'en 2D en raison du flux de fuite dans la tête de bobinage. En prenant les valeurs des pertes analysées par la simulation en 3D, la température de surface de la nouvelle machine analysée par la méthode Computational Fluid Dynamics est plus élevée que celle calculée dans l'optimisation.

Enfin, un prototype de machine est construit et quelques tests expérimentaux sont réalisés. Le résultat montre que la force électromotrice à vide a une forme d'onde similaire par rapport à la prédiction numérique en 3D et la différence de couple statique maximum entre les tests expérimentaux et les simulations par éléments finis en 3D est faible.

Mots-clés :

Machine synchrone à rotor bobiné, structure modulaire, bobinage concentrique à pas raccourci, méthode des éléments finis, optimisation numérique, algorithme Mesh adaptive direct search, méthode NOMAD, méthode *fmincon*, 3D simulation électromagnétique, 3D simulation thermique, méthode Computational fluid dynamics.

List of contents

List of figures

List of tables

General introduction

The present thesis aims to the design optimization of a Modular Brushless Wound Rotor Synchronous Machine (MB-WRSM) for Heating, Ventilation and Air Conditioning (HVAC) application. Modular machine with integrated drive electronics has been widely investigated in many applications, particularly in embedded systems. Its advantage is the best compromise between fault tolerant capability and overall system cost. In this thesis, a multiphase modular machine based on the POKI-POKI™ structure developed by Mitsubishi Electric Cooperation is investigated.

In Chapter 1, a comparative study of different machine structures is presented. Rare-earth magnet machines are commonly used in many applications due to their high torque density and high efficiency. However, the price of rare-earth magnets rose significantly in the last years and the future world supply of these magnets may be restricted. Therefore, electrical machines without magnets are considered to replace permanent magnet machines in the future in which MB-WRSM is selected for our application. Firstly, it is important to list the advantages and the disadvantages of MB-WRSM compared to Permanent Magnet Synchronous Machines (PMSM). Though by comparison, the main features and important characteristics of MB-WRSM can be clearly specified. Additionally, the description of fault tolerance is indicated to illustrate the advantages of the modular machine and then, the special manufacturing technique for POKI-POKI™ machine is also presented. In this introductory chapter, we present a brief description of our optimization type and of two algorithms used for solving our design problem.

In Chapter 2, the description of non-overlapping fractional slot concentrated winding is shown. The goal of this part is to define winding construction and winding layout for different phase, slot and pole combinations. Fundamental winding factor will be calculated as a significant criterion in order to select the most appropriate winding configurations. Then, an electromagnetic model based on Finite Element (FE) method of a salient pole synchronous machine is described and the machine efficiency is calculated. With selected phase/slot/pole combinations, several machines will be analyzed and compared in order to select an appropriate machine in term of several criteria. Finally, the selected WRSM will be compared to a reference design Surface-Mounted Permanent Magnet Synchronous Machine (SM-PMSM) in order to evaluate its interest.

Chapter 3 proposes an optimization study of the chosen MB-WRSM to achieve the desired performances. Numerical optimization algorithms based on FE analysis are widely used to design electrical machines, especially with complex geometries. The advantage of these approaches is that they have high accuracy by taking into account nonlinear properties of the materials. However, the computational time is important. In this chapter, Quasi-Newton based algorithm using *fmincon* solver and Mesh Adaptive Direct Search (MADS) based algorithm using NOMAD solver are compared by

testing several numerical design problems. The selected algorithm will be employed for optimal design of a MB-WRSM.

Chapter 4 validates the optimal design results obtained by using 3D electromagnetic/thermal simulations and experimental tests. 3D FE simulations via ANSYS Maxwell is used in order to achieve electromagnetic performances more precisely by taking into account the effect of the end-winding zone. Besides, the machine temperature is verified by Computational Fluid Dynamics (CFD) method via ANSYS Fluent. Then, the constructed prototype is submitted to some tests and compared to 3D FE predictions.

Finally, the conclusions of the thesis are presented and future research works are also suggested.

Chapter 1

State of the Art of Modular Brushless Wound Rotor Synchronous Machine

HVAC systems are typically the largest consumers of electrical energy in homes and office buildings. Saving energy needs to be considered due to the increase of recent environmental concerns. Since the power is mainly consumed by the motor used in the compressor so that the use of high efficiency and high torque density motors is an important issue for HVAC application. Nowadays, compressors for HVAC (an example is shown in Figure 1.1) frequently use PMSM because of its high torque density and high efficiency [1], [2]. However, the price of rare-earth magnet material such as NdFeB increases sharply and the rapid depletion of rare-earth magnet resources is an issue due to the future extensive use of the material in automotive drives, home appliance application and wind generators [4]. Therefore, other machines without rare-earth magnet material and high performance are considered to replace PMSM.

Figure 1. 1: LG compressor and permanent magnet motor

1.1 Comparison between Different Machines

The aim of the following study consists in investigating several electrical machines with high torque density, high efficiency and low cost for our application.

1.1.1 Rare-earth Permanent Magnet Synchronous Machine

PMSM is the best attractive motor in term of torque mass ratio and torque mass volume ratio. The PMSM has magnets mounted on the rotor and armature windings mounted on the stator. In fact, rare-earth magnet such as NdFeB generates a very strong magnetic field in a small volume and therefore, allow electrical machines to operate with very high torque density. Nevertheless, the use of PMSMs remains difficult to reach a significant constant power zone under good efficiency conditions, risk of demagnetization of the magnets at high temperature. Also, the loss of control of electronics at high speed operations may lead to high terminal voltages, which can become dangerous for the equipment. The

extensive use of rare-earth materials in a large number of applications can cause a strong exploitation of magnets and therefore, causes the sharply increase of the price. In 2011 and 2012, China, a country which has large rare-earth magnet resources, reportedly threatened to cut off international magnet supplies [3]. Moreover, recent sharp augmentation in the price of NdFeB magnets to more than 150 USD/kg is due to the increase areas of application [4].

PMSMs has two principle configurations with interior or surface magnets on the rotor. The position and the shape of the magnets can have a significant effect on the mechanical and electrical characteristics of the motor, especially on the inductances of the machine and the capability to operate on a wide range of speed at constant power.

Interior Permanent Magnet Synchronous Machine (refer to Figure 1.2)

Interior Permanent Magnet Synchronous Machines (IPMSMs) are built with magnets positioned inside the rotor. They are widely used in many variable speed applications which require wide flux-weakening operations such as electrical vehicles, domestic appliances [5]. One of the advantages of these machines is the torque generated by two components: one is generated by permanent magnet flux and the other by the rotor saliency. Besides, the rotor position can be detected without using a position sensor because of the anisotropic rotor [6]. However, due to the rotor structure, torque ripple and cogging torque which cause noise and vibration are critical problems in the IPMSM.

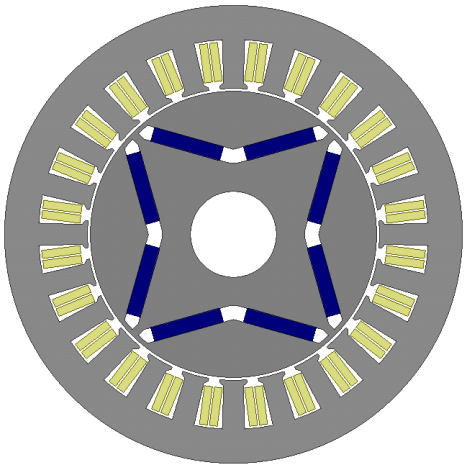

Figure 1. 2: Example of an interior permanent magnet synchronous machine

Surface-mounted Permanent Magnet Synchronous Machine (refer to Figure 1.3)

SM-PMSMs are constructed with magnets mounted on the surface of the outer periphery of the rotor. This configuration has several advantages such as easy manufacturing, higher remanent flux density and low torque ripple [7], [8]. However, the synchronous inductance of the machine is low such that it causes a high characteristic current and therefore, a low field weakening capability [9]. The mechanical robustness is lower than IPMSM due to high centrifugal forces. Therefore, it is not suitable for high speed applications without a sleeve which increases the air gap and decreases the torque. At slow speed,

the use of a glass fiber bandage is enough to withstand these forces. Moreover, the torque is only produced by the interaction between the stator currents and the magnets because this machine has no saliency.

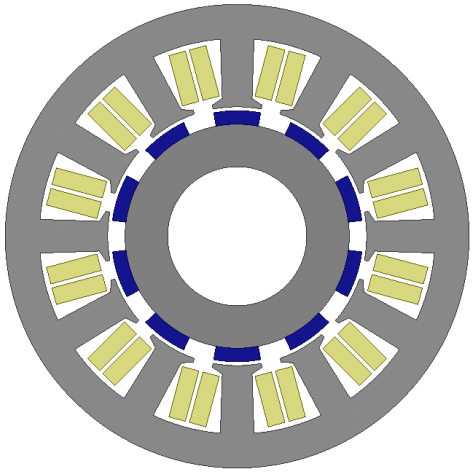

Figure 1. 3: Example of a surface-mounted permanent magnet synchronous machine

1.1.2 Alternatives to Rare-earth Magnets in Electrical Machines

Rare-earth permanent magnet machines are still the best solutions for high performance applications. However, for several applications, it may be not the best long-term solution due to the price spikes and the supply uncertainty of rare-earth magnets. Moreover, electrical machines with magnets are not efficient during a wide operating range. The exploitation of other electrical machines which do not have rare-earth magnetic materials are investigated. These machines are discussed in the following sections:

- Induction machine,
- Reluctance machine,
- Wound rotor synchronous machine.

Induction machine

Induction machines (IMs) do not contain magnets and they are widely used in many industrial applications due to their low cost, high reliability, mechanical robustness and wide constant power range in generating mode. IMs operate by inducing electrical currents in the rotor. Thus, the losses in the rotor are significant, which can cause total losses typically two or three times higher than in a PMSM [10]. The efficiency of these machines is thus lower than other machines and they may quickly become overheated. It is much more difficult to cool the rotating rotor than the stationary stator due to high losses occurred in the rotor. The biggest drawback of the IM is the lagging power factor.

Improvements can be obtained through the use of squirrel cage rotor and therefore, nowadays most IMs used are the squirrel cage machine shown in Figure 1.4. Rotor conducting bars usually use aluminum or copper. They are connected together with an end ring to form a closed electric circuit and a slightly skewed to the axis of the rotor for reducing the cogging torque. Copper cage IMs have been utilized in HEV and EV such as Renault Kangoo, Chevrolet, Silverado, Daimler Chrysler Durango and BMW 5

[33]. They improve efficiency and reduce temperature rising during the operation. However, the manufacturing cost of the cooper rotor cages can be higher [11].

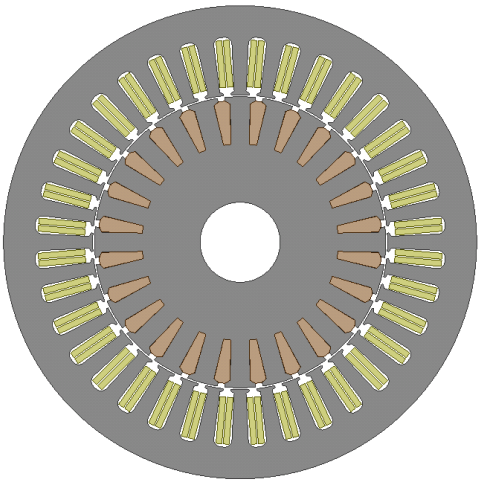

Figure 1. 4: Example of a squirrel cage induction machine

Reluctance machine

The generation of reluctance torque is produced by rotor saliency with non-isotropic magnetic reluctance that interacts with a stator magneto-motive force. There are two types of reluctance machines as:

- Synchronous reluctance machine,
- Switch reluctance machine.

Switched Reluctance Machines (SRMs) represented in Figure 1.5 do not contain PMs. They have a number of benefits such as robust structure, low cost and operating at high temperatures. Nevertheless, their disadvantages are complex control, high torque ripple and acoustic noise [12], [13].

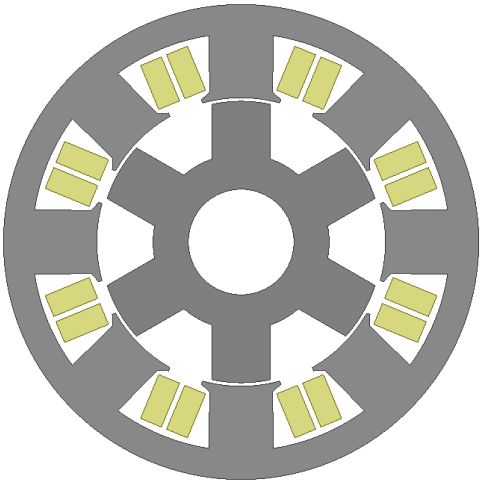

Figure 1. 5: Example of a switched reluctance machine

Like SRMs, Synchronous Reluctance Machines (SynRMs) shown in Figure 1.6 have no magnet. The SynRM conventionally uses a stator very similar to that used in an IM and a PMSM. This stator is

excited by sinusoidal currents to create a rotating field. The rotor which contains neither magnets nor copper winding is salient, offering a low reluctance in one axis and a high reluctance in the other axis. It allows the machine to lock synchronously onto the rotating stator field. The SynRM have a high efficiency due to the absence of the Joule losses in the rotor. However, the machine has several main problems such as a moderate torque density (SynRM < PMSM), a low power factor and a reduced field weakening zone [10].

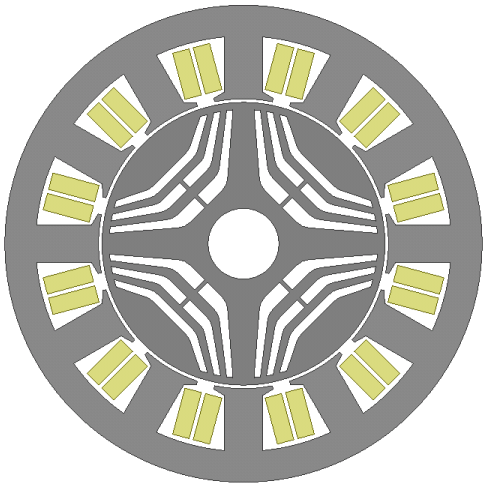

Figure 1. 6: Example of a synchronous reluctance machine

Wound rotor synchronous machine

Wound Rotor Synchronous Machines (WRSMs) shown in Figure 1.7 are widely used in electrical power generation worldwide at high power levels with high efficiency and reliability. WRSMs have several advantages including a low cost, a wide field weakening region at high speed and a significant improvement of the safety thanks to the possibility of canceling of the field current, and therefore, this limits the risks of high voltages for high speed operation [14], [18]-[22] which match well with the requirements of HVAC applications. However, the rotor windings cause Joule losses, and it is difficult to evacuate the heat. Additionally, the torque density of WRSM is usually lower than that of PMSM.

Moreover, the stator is fed with sinusoidal currents to generate AC rotating field, while the rotor contains copper windings which are excited by a DC current to set up a magnetic field. It is necessary to have a mechanism for passing current from the stationary part to the rotating part of the machine. The brushes and the slip rings can be thus required to supply the field current, leading to maintenance issues.

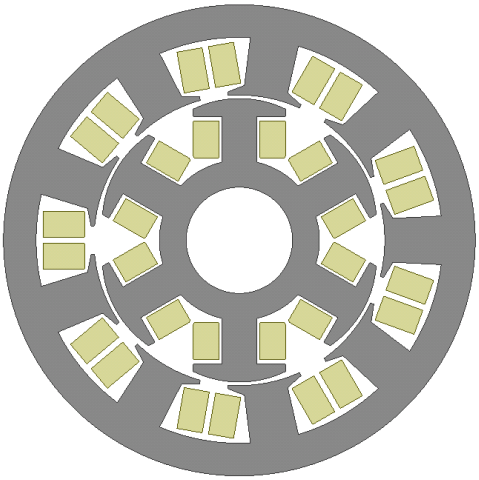

Figure 1. 7: Example of a wound rotor synchronous machine

Unfortunately, a perfect machine does not exist. The selection of a machine structure is always a compromise between the specifications of the application and the specificities of the partner company in terms of manufacturing cost, power density, machine efficiency and control strategies. In our study, MB-WRSMs are selected to be investigated; these machines have several advantages such as low cost, wide field weakening region, high fault tolerant capability, etc. In order to validate the relevance of this choice against Permanent Magnet Machine (PMM) which are widely used across a wide range of applications, a small comparative study will be conducted in the next section.

1.2 PMM and WRSM Performance Comparison

In order to replace PMMs in HVAC application, the torque density and the efficiency are a key issue to find an appropriate machine without magnet. Here, some comparisons between the WRSM and others machines are listed, especially PMM. The efficiency comparisons between the WRSM and the IPMSM in [15] is indicated in Table 1.1.

Table 1. 1: Efficiency comparison between WRSM and IPMSM

	Torque (Nm)	**Power (W)**	**Armature Current (A)**	**Field Current (A)**	**Line Voltage rms (V)**	**Power Factor**	**Efficiency (%)**
			2150rpm				
WRSM	18	4053	68.2	2.0	48.1	0.828	80.2%
IPMSM	18	4053	60.5	-	50.7	0.877	87.1%
			9000rpm				
WRSM	4.30	4053	34.02	1.1	77.25	0.975	89.72%
IPMSM	4.30	4053	43.2	-	77.30	0.852	84.50%

Note that the WRSM operates efficiently at high speed, due to an easier field weakening control. In Table 1.2, the comparison among the WRSM derived from the Prius IPM with different sizes of rotor and Prius Toyota PMM, IM at 1500 rpm in [16] are shown.

Table 1. 2: Comparison between PMM, WRSM and IM

	Peak Torque (Nm)	**Line Current rms (A)**	**Copper Loss (W)**	**Iron Losses (W)**	**Efficiency (%)**
PMM Prius Toyota	297	145	4547	202	90.8
WRSM	283	145	8400	200	86.0
IM	270	147.4	8063	-	83.8

Note that the efficiency of WRSM seems significantly lower than PMM at low speed due to higher copper losses.

The efficiency, cost comparison among different types of machine such as NdFeB magnet machine, ferrite PMM, WRSM, IM, and SRM in [10] is displayed in Table 1.3.

Table 1. 3: Comparison of electrical motor technologies

	Peak power (kW)	**Efficiency (%)**	**Torque density (Nm/kg)**	**Active material cost ($)**	**Active material cost per kW ($/kW)**
Reduced NdFeB Magnet M	80	98	15	223	2.78
Ferrite PMM	80	96	11	154	1.93
WRSM	50	96	10	144	2.88
Copper rotor IM	50	96	10	144	2.88
SRM	75	97	15	118	1.57

Note that the torque density of the WRSM is lower than that of the PMM. Although the price of active material cost of the WRSM is smaller than that of PMM, the active material cost per kW of the WRSM is higher than PMM.

Indeed, the WRSM and PMSM have the similar stator; however, the rotor of WRSM contains the winding and of PMM contains the magnets. The main drawbacks of WRSM compared to PMSM are a lower torque density and a lower efficiency at low speed due to losses in the rotor winding. Additionally, the slip ring and brushes require frequent maintenance, having a high copper loss, etc. In order to overcome this issue, a brushless system is implemented for the rotor field excitation [17]. Moreover, with the development of power converters, the modular model is proposed to increase fault tolerant capability which is an important requirement of embedded systems.

MB-WRSM can be a good candidate for embedded systems in which significant fault tolerant capability is required if its performances can be improved on the following points:

- Increase of its power/torque density,

- Increase of the efficiency.

Consequently, the MB-WRSM will be investigated with the objective to achieve high performances.

1.3 Modular Brushless Machine

1.3.1 Brushless Machine

Brushes and slip rings showed in Figure 1.8 which are usually used to excite the field current of WRSM is a demanding problem. Its disadvantages are losses, maintenance and debris issues.

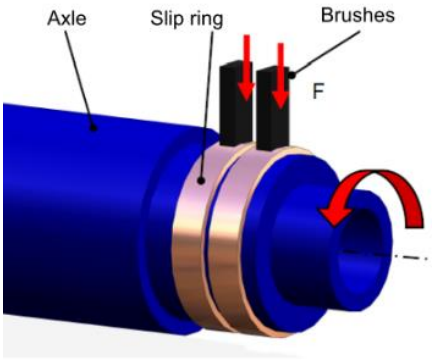

Figure 1. 8: Brush excitation [35]

In this study, a brushless system with a rotary transformer which have successfully demonstrated system efficiency > 90% with a lower lifetime cost is used. It causes lower frictional losses, and an easier maintenance compared to a brush system. A rotary transformer shown in Figure 1.9 is a transformer with an axial symmetry and an air-gap between the primary side and the secondary side. The air-gap allows the rotation of one half of the core, without influencing the flux lines and the inductive power transfer between the primary and secondary side [34].

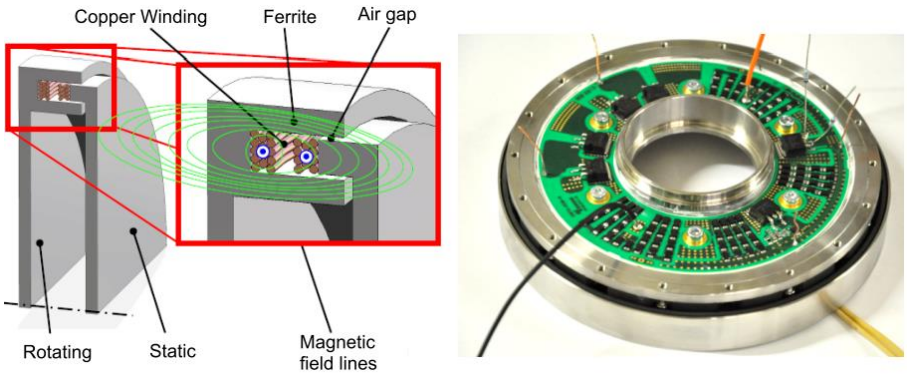

Figure 1. 9: Rotating transformer [35]

1.3.2 Modular Machine

1.3.2.1 Fault tolerant capability

Fault tolerance of a system is a key issue in embedded systems. Safety must be considered in the event of a failure into the system. As consequence of the failure, some damages of the equipment and danger for the system operators can occur [23]. In WRSM drives, several faults, both in the machine and in the power converter must be considered. [24], [25] show many potential faults that can occur in electrical machines such as:

- Winding open circuit,
- Winding short circuit: phase to phase, phase to ground, turn to turn,
- Short circuit at the machine terminals.

Phase to phase short circuit faults are among the most common faults in AC machine. The combination of the above faults can occur because they tend to be cumulative and therefore, one fault induces other faults. Here, a modular system is proposed in order to prevent this type of short circuit.

The use of modular machine drive increases the redundancy and improves reliability of the system [29]-[31]. The integration of the drive electronics into the housing of the machine shown in Figure 1.10 has been widely investigated in a wide range of applications [26].

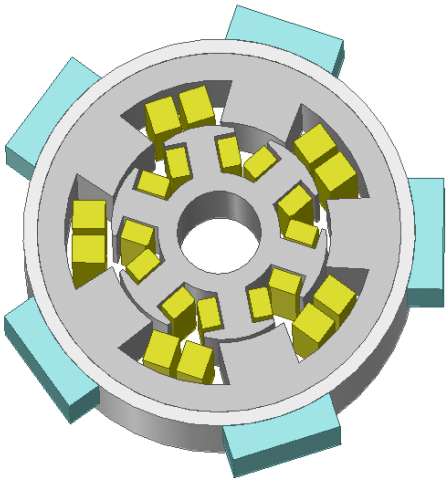

Figure 1. 10: Single phase modular configuration

Integration of the machine and drive has several advantages in [27], [28] as:

- Reduction of the total drive volume and weight,
- Elimination of interconnects and reduce the risks of generating high voltage transients on the winding.

However, the use of integrated motor drive can cause an increase of losses and therefore, of the temperature.

In this study, each phase of the machine is connected to a separate single-phase converter (see Figure 1.11). Each phase drive module is considered as a single module and every phase can operate independently of the others. These structures are highly redundant and the effects on the other phases are minimized in case of having fault at one phase. It means that the system is well able to continue the operation when a fault occurs.

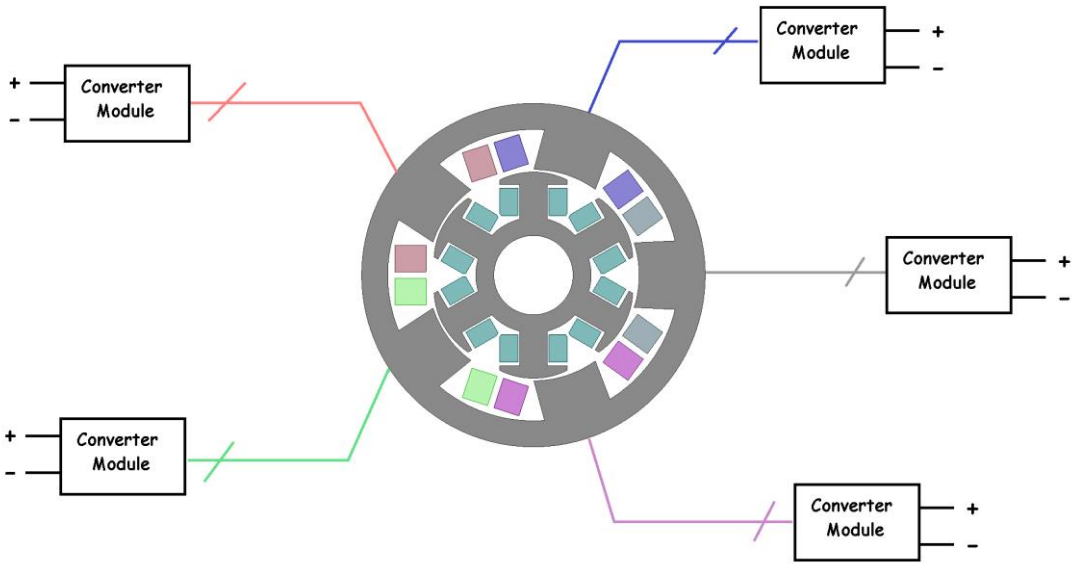

Figure 1. 11: Integrated machine and power supply concept

1.3.2.2 Multiphase machine

The multiphase machine has recently become a competitive candidate for safety critical applications due to its enhanced fault tolerant capacity compared to a conventional three-phase machine. The higher number of phases increases the number of freedom degrees for the machine supply which is used to achieve a better performance and a higher fault tolerance. There are several considerable benefits from the use of multiphase machines [23], including:

- Improved fault tolerant behavior

Multiphase machine has an improved fault tolerant capability because more phases can provide partial retention of functionality even in the eventuality of a power component die.

- Reduced phase current

In a multiphase AC drive, the phase current can be reduced without increasing the voltage per phase since the power is evenly divided among a larger number of phases. This reduces the size and the power rating of the individual power semiconductor switches.

- Improved armature magneto-motive force waveform

Multiphase machines can improve Magneto-Motive Force (MMF) waveforms. The reduction in the armature air-gap MMF harmonic components has several advantages such as the torque ripple reduced, acoustic noise reduced and lower rotor losses.

Nevertheless, the multiphase machine has several drawbacks such as:

- Higher number of power semiconductor switches are needed. It can increase the volume, the weight and the cost of the power converter, leading to a higher complexity and possibly to a lower reliability of the overall system,
- Non fundamental harmonics of the current must be considered by the control.

Finally, the increase in the number of phases could finally make the whole system more complex and expensive. However, it increases the fault tolerant capability as well as better reliability.

1.3.2.3 Stator segmentation

An interesting concept for achieving higher modularity in the machine is the segmentation in the stator core. For this structure, high fault tolerant capability can be achieved due to physical separations. These advantages are presented in [26]. Indeed, the faulty components can be replaced quickly and cheaper. Moreover, the copper slot fill factor is higher and the machine can be wound automatically. One of different types of the segmented stator is a 'T-core' segment as shown in Figures 1.12 and 1.13.

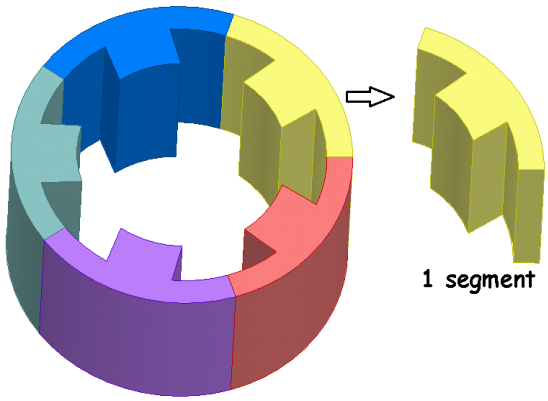

Figure 1. 12: Stator segmentation

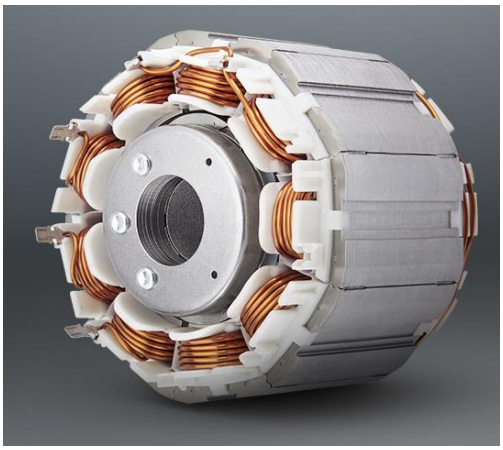

Figure 1. 13: Modular motor in LG compressor

Mitsubishi Electric Corporation developed this type of machine called POKI-POKI™ shown in Figure 1.14. The stator slots are fully open (e.g. the teeth have no tip) and therefore, it is easier to pre-wind the coil for each segment of the stator core with non-overlapping concentrated winding. After the coils are wound, the stator is formed into a cylindrical shape and is press fitted into a frame. Its advantages are the modularity, the fast automatic winding manufacturing, the easiness to assemble and to remove, and therefore, it is easier to replace faulted components and this simplifies the connections in the machine. Moreover, the slot fill factor can be increased, leading to a decrease of copper losses [32]. It should be noticed that the POKI-POKI™ machine is only suitable for short active length due to the mechanical assembly.

Figure 1. 14: Modular structure of POKI-POKI^{TM} machine [32]

1.4 Optimization Methods for Machine Design

1.4.1 Mathematical Optimization Formulations

Everything in our daily life needs to be optimized in order to look for a better solution. Especially, optimization is an important tool in science and industry. Since 1980, with the increasingly need of electrical machines, design optimization methods which solve problems about machine weight, volume, cost and efficiency have been developed. The goal of optimization methods is to find the values of the variables that minimizes or maximizes an objective function subject to several constraints.

Generally, mathematical optimization problems involve continuous and integer variables and twice differentiable functions. However, from different domains of physics, design problems have to be formulated by considering some integer variables yielding Mixed-Integer Non-Linear Programs (MINLP):

$$\begin{cases} \min\limits_{x\in\mathbb{R}^n, z\in\mathbb{N}^m} f(x,z) \\ \text{Under constraints:} \\ \quad g_i(x,z) \le 0 \;\forall i \in \{1,\dots,p\} \\ \quad h_j(x,z) = 0 \;\forall j \in \{1,\dots,q\} \end{cases} \tag{1.1}$$

Where: x is the vector of variables, f is the objective function, g_i are the inequality constraints and h_j are the equality ones.

The objective and the constraint functions depend on continuous and integer variables. Generally, the design of electrical machines has this formulation and several different algorithms can be used and developed to solve this mixed-integer non-linear optimization problem. Examples of applications for solving the MINLP can be found in [36]-[41]. [36] presented the optimization problem of designing electromagnetic actuators with many types of variables such as real, integer, categorical and logical variables; e.g. categorical variables are used to characterize materials.

Actually, several optimization algorithms need some information about the derivatives of the functions and also an explicit analytical formulation of them. Several examples in [36], [42] and [43] described the optimization problem using analytical models for electrical machines, actuators. In this case, efficient deterministic global algorithm, named IBBA (an exact global optimization method based on an interval Branch and Bound technique) is used. Several stochastic algorithms like Genetic Algorithms can also be used to solve problems of type (1.1), see [44]-[46].

The multiphase salient pole WRSM owns a complicated structure. To develop analytical models, normally, we must simplify the machine geometry and linearize the magnetic properties by using some form of equivalent permeability. Nowadays, obtaining an accurate analytical model for salient pole WRSM design is a really challenging task. Considering that, one of the solution is to use numerical models based on FE method. Indeed, with the development of computer technology, the design of electrical machines using numerical simulations has been widely used because they are able to take both saturation and complicated geometry into account. One of the drawbacks with the numerical simulation is the computation of the derivatives which is very expensive in CPU time (finite difference method). This leads to the idea that achieving the global minimum of the problem MINLP (Equation (1.1)) seems to be unreachable. Thus, in this thesis we focus on the search of local minimums by trying to find the best possible one. Moreover, in order to investigate a complete design problem formulated as a MINLP, all of our calculations which are carried out by numerical simulations via FE code appears to be very difficult at this stage. Hence, the interesting structures of the WRSM are previously studied in Chapter 2 and the most efficient structure is selected. This allows us to consider a continuous optimization problem where the functions are performed via a FE code. The optimization problems that we study in this thesis are:

$$\begin{cases} \min\limits_{x\in\mathbb{R}^n} f(x) \\ Under\ constraints: \\ \quad g_i(x) \le 0\ \forall i \in \{1,\dots,p\} \\ \quad h_j(x) = 0\ \forall j \in \{1,\dots,q\} \\ \quad a_i \le x_i \le b_i \end{cases} \tag{1.2}$$

The design of electrical machines including electromagnetic, mechanical and thermal requirements should be considered in the optimization. This makes the composition of an electrical machine more complex. Using efficient tools is thus necessary in order to obtain good solutions. Within the past decade, many optimization algorithms have been investigated for the design of electrical machines [36], [45]. The algorithms are evaluated and compared in order to find efficient solutions for the applied optimization problems. Therefore, the choice of the algorithm is an important task because it may determine whether the problem is solved rapidly or slowly and whether the solutions are good or not. In the next subsection, we present the two optimization algorithms we use in this thesis.

1.4.2 Optimization Algorithms (*fmincon* & NOMAD)

The two different optimization algorithms used on this thesis are: Quasi-Newton based algorithm and MADS based algorithm. The Quasi-Newton based algorithms are implemented in the *fmincon* routine

of Matlab, it is a gradient based method [47]-[49]. In contrary, NOMAD solver based on MADS method does not use derivative computations [50]-[52].

The main difference between these two optimization algorithms is the computations or not of the derivatives, else they use the same iterative following steps:

$$x^{[k+1]} := x^{[k]} + d^{[k]} \tag{1.3}$$

Where: $x^{[k]}, x^{[k+1]}$ is the vector variable at $k, k+1$ optimization iteration, $d^{[k]}$ is a direction of descent; e.g. a direction which makes it possible to assure the convergence of a suite of point $x^{[k]}$ to a local optimal solution.

Thus, these two optimization methods always require a starting point $x^{[0]}$ which is a key issue in the convergence of those algorithms. Based on that, the two algorithms search for the next point by determining $d^{[k]}$; the computation of $d^{[k]}$ is the main difference between local optimization algorithms.

fmincon code

Quasi-Newton based algorithms which are widely used to optimize the design of electrical machines. It can solve nonlinear constrained problems of type (1.2) based on the computations of derivatives of the objective function and of the constraints. *fmincon* solver which is based on Quasi-Newton updating method is available in Matlab Toolbox. It requires a gradient to define a search direction and calculate the search distance in which the Hessian of Lagrangian function is approximated by updating at each iteration thanks to the function values and gradients from previous iterations [48]-[49].

The basic form of the use of this Matlab routine is:

$$X = fmincon(FoncObj, x_o, A, b, A_{eq}, b_{eq}, lb, ub, Cont, option) \tag{1.4}$$

Where: X is the optimal solution, $FoncObj$ is the objective function, x_o is the starting point, A, b are the inequality constraint $Ax < b$, A_{eq}, b_{eq} are the equality constraint $A_{eq}x = b_{eq}$, , lb and ub are the interior and exterior bounds of the variables, $Cont$ is the constraint function, $option$ is the selected algorithm.

Active-set, *sqp* and *interior-point* optimization algorithms can be selected in the *fmincon* routine. These algorithms differs also on the way to compute the descent direction $d^{[k]}$, for details on these algorithms see [47].

NOMAD code

NOMAD solver which is available in Matlab Toolbox can solve nonlinear constrained problems of type (1.2). It is well suited to solve black-box optimization (where the function or/and the constraints are computed via a numerical code) [50], [51]. Its architecture is shown in Figure 1.15 where the objective function and/or constraints could be computed via the use of numerical simulations (non-accessible information). Actually, NOMAD can be used when:

- There is no access to the derivative,
- The evaluation of the function may be polluted by noise,
- The evaluation of the objective function may fail even on admissible points.

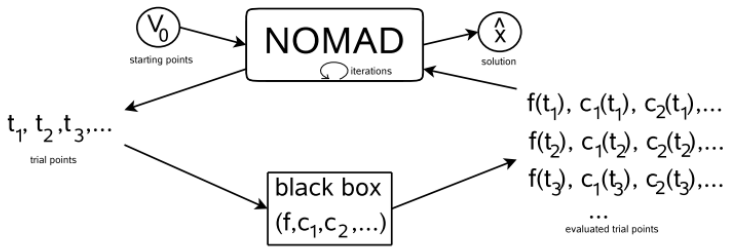

Figure 1. 15: NOMAD solves black-box problem [50]

MADS is a kind of the local direct search method, it is proved that NOMAD converge to a local solution [53]-[56]. It includes the search step and the poll step. At each search step, trial points are generated on the mesh using a mesh size parameter. At the poll step, random points are chosen among mesh points in the frame with a poll size parameter. For the current solution (found at iteration *k* of the algorithm), the frame center is the center of a mesh. When an improved solution is located in the neighborhood, it becomes a new frame center. A frame is regenerated from this new frame center. The mesh size shown in Figure 1.16 is controlled to look for a solution. It can be increased for successful searches and decreased for unsuccessful searches. When the mesh size is inferior to a tolerance value, an optimal solution can be obtained and the search is terminated.

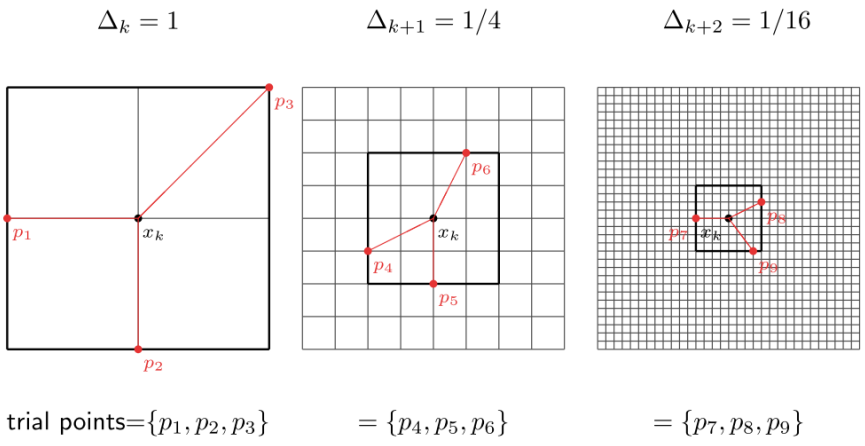

Figure 1. 16: An example for explaining NOMAD algorithm [51]

NOMAD can also use surrogate functions [57] instead of the real objective function for the poll step and use the real objective function only to check the accuracy of the value found (Figure 1.17). In this way, test points are evaluated through the substitute function (which is easier and more rapidly computed) and so, most promising points are evaluated by the real objective function. This makes it possible to explore the search space better and reduce the computational time.

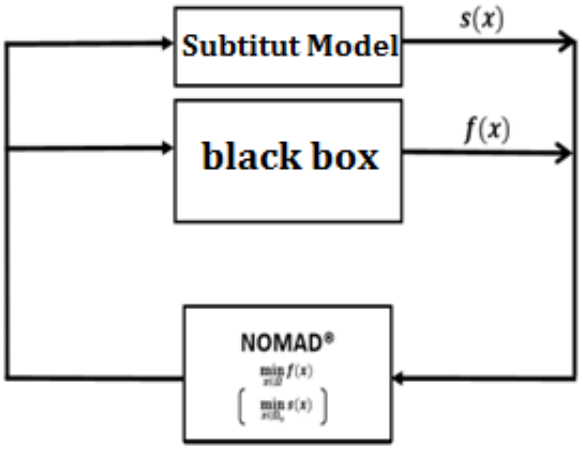

Figure 1. 17: Substitute model can be used in NOMAD [57]

1.5 Chapter conclusion

The machine in the compressor of HVAC system often use expensive rare-earth permanent magnet materials, but manufacturers are keen to develop drive machines without magnet. The different types of electrical machines have been reviewed with theirs advantages and drawbacks. Based on that, we justified the choice to study a MB-WRSM used for our HAVC application. This machine has no rare-earth magnet material and needs to reach the high performance that PMSM provides. In order to achieve a high performance WRSM as best as possible, optimization methods are key issues in our study. Therefore, optimization is presented and the two algorithms which are used in this thesis, are detailed at the end of this chapter.

Indeed, the key issue of machines without magnet is the torque density and the efficiency. Therefore, in the next chapter, a precise study of the WRSM is conducted to determine the structure which is the most interesting one. Moreover, this structure is then compared to a reference design SM-PMSM in order to evaluate its potential for the application.

Chapter 2

Choice of WRSM Structure

FE analysis becomes more popular in the field of electrical machine design since analytical equations are not easily formalized for the machines which have complicate structures. Using electromagnetic analysis, we comparatively study different WRSMs and therefore, select the structure which offers the best fault tolerant capability and the highest output performances. For this propose, firstly, the winding characteristics and the numbers of phases, slots and poles must be selected. With suitable winding configurations, several machines are analyzed by using 2D FE simulations which allows us to compute the machine performances. According to the torque density, the torque ripple and the machine efficiency, an appropriate machine is chosen and then compared to a reference design SM-PMSM in order to evaluate the interesting performance features of the WRSM.

2.1 Fractional Slot Concentrated Winding

Fractional Slot Concentrated Winding (FSCW) machines have been widely investigated for many applications. They are well suited for fault tolerant applications [58]. Several advantages of employing a FSCW are listed in [59] - [61] as:

- Higher copper slot fill factor if coupled with segmented stator structures,
- Short end-winding and therefore, copper losses can be reduced,
- Suitable for automatic manufacturing and reduced manufacturing costs in modular designs,
- A high leakage inductance and a low mutual inductance, leading to the improvement of the flux weakening capabilities,
- The contact among the phases is reduced due to high leakage inductance and low mutual coupling among the phases. It is an interesting solution for fault tolerant applications.

Considering the thermal aspect of the machine, FSCW ensures physical and magnetic isolation is maintained to increase fault tolerant capability [63]:

- Physical insulation: In concentrated windings, the coils are wound around a single tooth, and there is non-overlapping between phases. Thus, the electric fault between machine phases is limited in this phase. In double layer winding machines, a separator between coil sides may be required in order to guarantee the insulation between phase windings.
- Magnetic insulation: A high linkage inductance can limit the short-circuit currents. Moreover, a low mutual inductance among the phases enables preventing the impact of one phase on other phases.

Nevertheless, the use of FSCWs can lead to undesirable effects such as eddy current losses, torque ripple, acoustic noise and vibration due to an increase in the harmonic content of MMF waveform [62].

2.1.1 Number of winding layers

Figure 2.1 illustrates both type of windings: double layers and single layer. Single layer windings have coils wound only on alternate teeth, whereas each tooth of the double layer windings carries a coil. The selection of number of layers is based on the characteristics of the machine which is suited for a particular application.

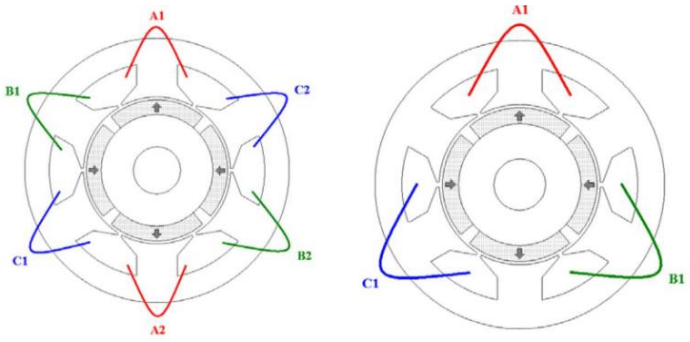

Figure 2. 1: Double layer and single layer windings [59]

Table 2.1 presented in [59] indicates the comparison of double layer windings and single layer windings.

Table 2. 1: Comparison of double layer and single layer windings

	Double layer windings	**Single layer windings**
Difference of coils/slot	2	1
Mutual phase coupling	Significant phase-phase coupling through mutual slot leakage	Very low mutual phase coupling
End turns	Shorter end turns	Longer end turns
Phase inductance	Lower phase inductance due to lower phase leakage inductance	Higher phase inductance due to higher phase leakage inductance
Rotor losses	Lower rotor losses mainly due to lower fundamental stator MMF space harmonic component	Higher rotor losses mainly due to higher fundamental stator MMF space harmonic component
Slot/pole combination	Many slot/pole combinations possibility	Few slot/pole combinations possibility
Ease of manufacturing	More difficult	Easier
Synchronous winding factor	Lower	Higher
Back electromotive force	More sinusoidal	Less sinusoidal

The double layer FSCWs shown in Figure 2.2 can cause lower rotor losses, torque ripple, vibration and noise due to the lower air-gap MMF harmonic content compared to the single layer FSCWs. Nevertheless, in the single layer, physical separation between phases is better and the phase inductance is higher. This makes it possible to improve thermal issues and fault tolerant capability. In this study, torque density, machine efficiency and torque ripple are the important requirements so that double layer winding seems to be more appropriated.

Figure 2. 2: An example of double layer concentrated winding [64]

Besides, the open slot type is selected because of the advantage of permitting easy installation of form wound coils and their easy removal in case of repair. Nevertheless, its drawback is that the air-gap flux can be distributed into bunches or tufts, and therefore, the ripples can be produced in the wave of generated Electro-Motive Force (EMF) and electromagnetic torque.

2.2 Phase, Slot and Pole Combination

Winding factor plays an important role in the torque production. The winding factor for the main harmonic should be as high as possible in order to maximize the EMF and consequently the average torque of the machine. In case of low fundamental winding factor, the stator winding needs to be fed with higher currents in order to generate the same torque compared to the machine with higher fundamental winding factor. Considering that the winding factor depends on slot and pole combination as well as winding layout, the selection of phase, slot and pole combination is thus a critical issue in order to maximize the fundamental winding factor.

In general, AC machine windings can be classified according to the number of slots per pole per phase (q). The windings are distributed when $q \geq 1$. And the windings are concentrated when $q \leq 1$. When q is not an integer, the winding is a fractional slot winding. Otherwise, it is referred to as integral slot winding. Additionally, there are a set of rules for the pole and slot combinations that makes non-overlapping windings valid [65]:

- The number of poles must be even,
- The number of slots must be a multiple of the number of phases,
- The number of coils and slots are equal in double layer windings,
- The number of slots cannot be equal to the number of poles.

The various combinations of phase, slot and pole numbers which enable achieving a balanced winding can be determined by the following condition:

$$\frac{Q}{|GCD(Q,2p)|} = km \tag{2.1}$$

Where: Q is the number of slots, p is the number of pole pairs, m is the number of phases and k is an integer number.

For a specific slot/pole combination and number of phases, there are many possibilities to arrange the coils of each phase in the slots to form the winding layout. For non-overlapping double layer FSCW, the fundamental winding factor can be calculated by different methods: Cros' method and Star of Slots.

2.2.1 Cros' method

The Cros' method based on EMF phasors consists in defining the winding layout of double layer FSCW which makes it possible to maximize the fundamental winding factor of the fundamental EMF. This method was investigated by some authors [65]-[67]. A review of these papers is presented in this part.

The number of slots per pole per phase q must be defined in its most simplified fraction. For values below unity, q must be reduced to a fraction of two non-divisible integers (b and c) as:

$$q = b/c \tag{2.2}$$

A one-zero sequence can be established thanks to this equation. The number of "1" in the sequence is equal to b, and the number of "0" is equal to c - b. For a given structure, the winding with the highest fundamental winding factor can be obtained by the most regular distribution of the number "1" among the numbers "0". The structure of the whole winding can be determined in five steps:

- In a first step, the one-zero sequence created is based on the number of slots per pole per phase.
- The sequence is repeated Q/b times.
- The usual phase sequence (e.g. AC'BA'CB' for a three-phase machine) is assigned to the aforementioned number sequence (A' characterizes the return conductor corresponding to conductor A).
- The conductors corresponding to the numbers "1" are selected to make the first layer of the double layer winding.
- The second layer of the winding is obtained by shifting the first layer in the other side of the tooth and reversing the phase direction.

The final winding layout of one phase is created. This layout is described by a vector S which contains the number of filled slots. For each slot which contains the conductor of the phase A, the number of the slot with the sign of the phase is written in S. If the two layers of one slot contains phase A, then the number of the slot is A'. For the conductor A', a minus is added to the corresponding slot numbers. The last step is essentially used to calculate the fundamental winding factor for double layer windings. The vector S is used to obtain the EMF phasor E_i of conductor i from the one phase for the main harmonic rank of p or the fundamental is represented as:

$$\overrightarrow{E_i} = sign(S(i))e^{j\pi\times 2p\left|\overrightarrow{S(i)}/Q\right|}. \tag{2.3}$$

Thanks to that, the fundamental winding factor is calculated by:

$$k_{w1} = \frac{\left|\sum_{i=1}^{2Q/m} \overrightarrow{E_i}\right|}{2Q/m}. \quad (2.4)$$

An example for the three-phase machine with 9 stator slots, 8 poles is given to illustrate the Cros' method. The configuration for double layer FSCW is established as follows:

- The number of slots per pole per phase is:

$$q = 3/8$$

- The optimum one-zero sequence is:

1 0 0 1 0 0 1 0

- The complete sequence is:

10010010 10010010 10010010

- The usual nested phase sequence AC'BA'CB' is assigned as:

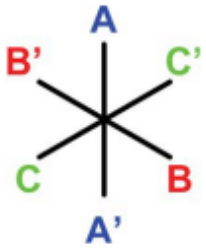

10010010 10010010 10010010
AC'BA'CB'AC' BA'CB'AC'BA' CB'AC'BA'CB'

- The conductors associated to the number "1" are:

A A' A B B' B C C' C

- The second layer is:

A' A A' B' B B' C' C C'

- The final winding layout is created as follows:

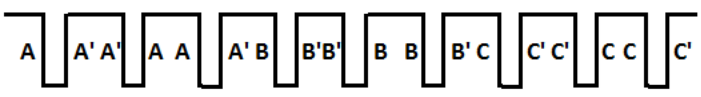

- The vector *S* is calculated for phase A as:

S = [1 -2 -2 3 3 -4]

- The EMF vector of the conductor corresponding to the element i of vector S is:

$$\overrightarrow{E_i} = sign\big(S(i)\big)e^{j\pi p\left|\frac{\overrightarrow{S(i)}}{Q}\right|} = e^{j\frac{8\pi}{9}} - e^{2j\frac{8\pi}{9}} - e^{2j\frac{8\pi}{9}} + e^{3j\frac{8\pi}{9}} + e^{3j\frac{8\pi}{9}} - e^{4j\frac{8\pi}{9}}$$

- The fundamental winding factor is thus calculated as:

$$k_{w1} = \frac{\left|\sum_{i=1}^{2Q/m}\overrightarrow{E_i}\right|}{2Q/m} = \frac{\left|e^{j\frac{8\pi}{9}} - e^{2j\frac{8\pi}{9}} - e^{2j\frac{8\pi}{9}} + e^{3j\frac{8\pi}{9}} + e^{3j\frac{8\pi}{9}} - e^{4j\frac{8\pi}{9}}\right|}{6} = 0.9452$$

Considering that many one-zero sequences can be created from the specific number of slots per pole per phase when the position for number "1" and number "0" are changed in the one-zero sequence. Each sequence can form different winding layout with different fundamental winding factor.

As the example above, the other one-zero sequence is:

1 0 1 0 1 0 0 0.

- The complete sequence is:

10101000 10101000 10101000.

- The usual nested phase sequence AC'BA'CB' is assigned as:

1	**0**	**1**	**0**	**1**	**0**	**0**	**0**	**1**	**0**	**1**	**0**	**1**	**0**	**0**	**0**	**1**	**0**	**1**	**0**	**1**	**0**	**0**	**0**
A	C'	**B**	A'	**C**	B'	A	C'	**B**	A'	**C**	B'	**A**	C'	B	A'	**C**	B'	**A**	C'	**B**	A'	C	B'

- The conductors associated to the number "1" are:

A B C B C A C A B

- The second layer is:

A' B' C' B' C' A' C' A' B'

- The final winding layout is created as below:

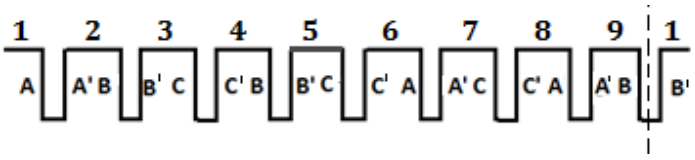

- The vector S is calculated for phase A as:

S = [1 -2 6 -7 8 -9]

- The EMF vector of the conductor corresponding to the element i of vector S is represented as:

$$\overrightarrow{E_\iota} = sign\big(S(i)\big)e^{j\pi p\left|\frac{\overrightarrow{S(\iota)}}{Q}\right|} = e^{j\frac{8\pi}{9}} - e^{2j\frac{8\pi}{9}} + e^{6j\frac{8\pi}{9}} - e^{7j\frac{8\pi}{9}} + e^{8j\frac{8\pi}{9}} - e^{9j\frac{8\pi}{9}}$$

- The fundamental winding factor for double layer FSCW is:

$$k_{w1} = \frac{\left|\sum_{i=1}^{2Q/m}\overrightarrow{E_\iota}\right|}{2Q/m} = \frac{\left|e^{j\frac{8\pi}{9}} - e^{2j\frac{8\pi}{9}} + e^{6j\frac{8\pi}{9}} - e^{7j\frac{8\pi}{9}} + e^{8j\frac{8\pi}{9}} - e^{9j\frac{8\pi}{9}}\right|}{6} = 0.8312$$

It can be noted that with the same phase/slot/pole combination, for the optimum one-zero sequence 10010010, the fundamental winding factor is equal to 0.9452 and for the other one-zero sequence 10101000, the fundamental winding factor is 0.8312. Therefore, for the specific number of slots per pole per phase, it is necessary to select the optimum one-zero sequence which allows us to achieve the highest fundamental winding factor.

2.2.2 Star of Slots

Star of Slots is a technique to assign phases and polarities to each coil side to determine the winding layout. It represents the phasors of the main harmonic of the EMF induced in a coil side of each stator slot. The distribution of the air-gap flux density is assumed as sinusoidal and Faraday's law in the BLv form is applied. Each phasor is numbered according to the number of the slot that contains the corresponding conductor in order to represent the EMF induced in a coil [63]. The star of slots makes it possible to compute not only the distribution factor but also the pitch factor as described in [68]-[70]. The winding factor k_{wv} of a rank harmonic v is thus calculated as:

$$k_{wv} = \frac{sin\frac{v\pi}{2}}{Z}\sum_{\rho=1}^{Z}\cos\alpha_\rho \tag{2.5}$$

Where: α_ρ is the angle of the phasors with respect to this symmetry line, Z is the number of phasors of one phase and v is the harmonic rank.

In order to maximize the EMF, it is interesting to calculate these phase shifts. It is thus necessary to define several parameters. Firstly, the electrical periodicity of the machine is defined by the greater common divisor between the number of slots Q and the number of pole pairs p as:

$$t = GCD(Q, p) \tag{2.6}$$

Where: t is the number of layers of a voltage phasor diagram.

The winding contains symmetrical coils to create a rotating magnetic field. The feasibility of a winding requires that each phase is composed of an integer number of coils. The symmetry condition that has to be satisfied to have the same number of phasors for each phase is written in Equation (2.1).

The condition of symmetry for double layer windings is:

$$2p/c \in \mathbb{N} \text{ and } \frac{c}{m} \notin \mathbb{N} \tag{2.7}$$

The angle in electrical radians between the EMF phasors of two adjacent slots is:

$$\alpha_u = p \times 2\pi/\mathrm{Q} \tag{2.8}$$

The angle between two adjacent radii is given by:

$$\alpha_s = 2\pi\mathrm{t}/\mathrm{Q} \tag{2.9}$$

Then, the star of slots is characterized by Q/t radii, each of them formed by t phasors.

The star of slots represents the main harmonic EMF phasor and gives the position of the coils of each phase. In fact, the EMF of each phase is obtained by summing those EMF phasors with minimum angular displacement. The phasors of one phase are determined by superimposing to the star of slots two opposite sectors of plane spanning π/m radians (for an m phase machine). Hence, the coil sides of the first layer that correspond to the selected phasors are assigned and then the coil sides of the second layer are determined. This is useful to compute the winding factors for the different harmonics.

As an example, let consider the design of a double layer FSCW with $Q = 9, 2p = 8, m = 3, q = 3/8$.

- The greater common divisor between 9 slots and 4 pole pairs is $t = 1$.
- The condition of symmetry $\frac{Q}{t \times m} = \frac{9}{3} = 3$ is satisfied.

The parameters of the voltage phasor diagram of a winding are described as follows:

- The number of layers in the voltage phasor diagram is:

$$t = 1$$

- The number of phasors of a single turn in a voltage phasor diagram is:

$$Q' = Q/t = 9$$

- The angle between the EMF phasors of two adjacent slots is:

$$\alpha_u = {}^{8\pi}/_{9}\ (rad)$$

- The angle between two adjacent radii is:

$$\alpha_z = {}^{2\pi}/_{9}\,(rad)$$

The number of phasors Q' is 9 and there are 3 phasors for each phase which are divided into negative and positive phasors. The angle $\alpha_z = 2\pi/9$ corresponds to the angle between two adjacent vectors. Phasor 1 is positioned to point straight upwards. The next phasor 2 is located at an electrical angle of $\alpha_u = 8\pi/9$ in clockwise direction from the first phasor. The voltage phasors are built in Figure 2.3.

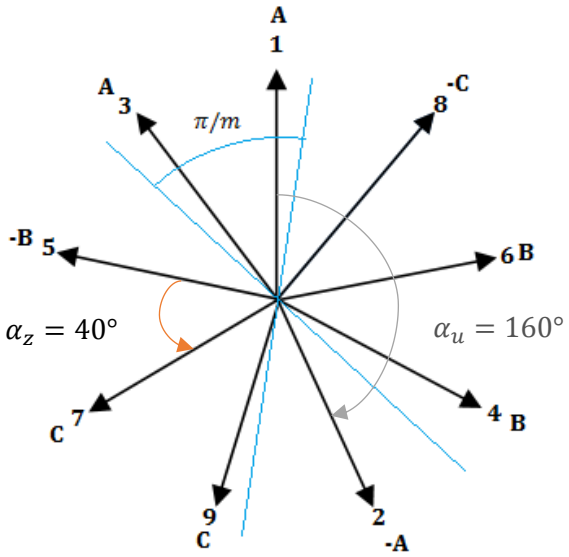

Figure 2. 3: Voltage phasor diagram of 3-phase/9-slot/8-pole machine

Using two opposite sectors of plane spanning π/3 radians, 3 phasors included in these sectors are assigned to each phase. The layout of one coil side is:

A A' A B B' B C C' C

For each coil, only the EMF induced in one coil side is represented and placed at left coil sides of each coil. The number of each phasor corresponds to the number of the slot containing the corresponding coil side. The layout of non-overlapping double layer FSCW is shown in Figure 2.4.

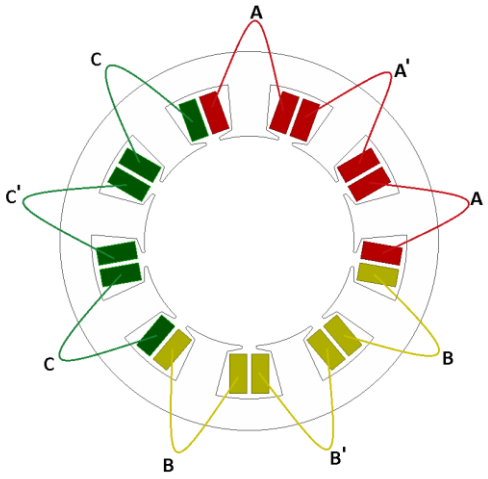

Figure 2. 4: Winding layout of 3-phase/9-slot/8-pole machine

The phasors of the phase A for the calculation of the winding factor is shown in Figures 2.5 and 2.6.

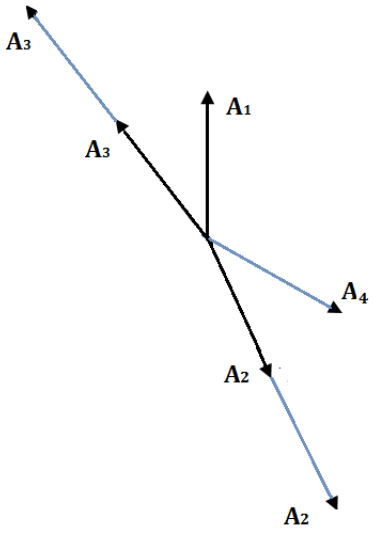

Figure 2. 5: Phasors of phase A

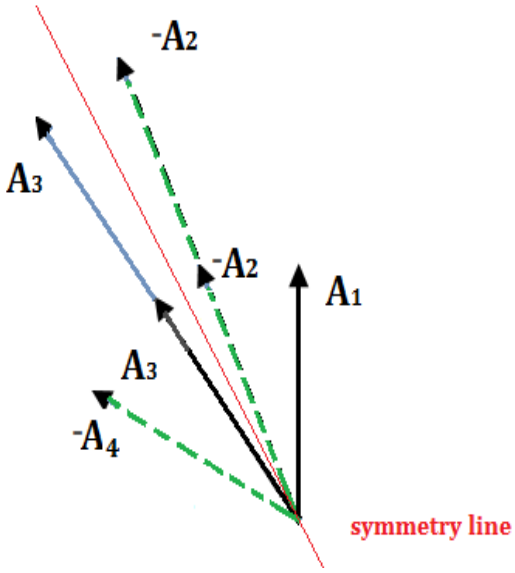

Figure 2. 6: Phasor distribution

After finding the angle with respect to the symmetry line, the maximum fundamental winding factor may be calculated using Equation (2.5) as:

$$k_{w1} = \frac{1}{Z}\sum_{\rho=1}^{Z}\cos\alpha_\rho = \frac{4\cos(10°) + 2\cos(30°)}{6} = 0.9452$$

2.2.3 Winding Factor Results

In Table 2.2, the fundamental winding factors for FSCWs are shown with the number of rotor poles smaller than 10. The number of rotor poles is limited due to manufacturing considerations for small machines (the limited value is considered as a specification). It should be noticed that the fundamental winding factor of 6-phase/12-slot/10-pole machine is the highest. The fundamental winding factors of the three-phase machines with 9 slots/8 poles or 10 poles and 12 slots/10 poles are higher than 0.9. For the 4-phase machine, the fundamental winding factors with 8 slots and (6 or 10) poles are 0.9239. Besides, the fundamental winding factors of five-phase machine with 5 slots and (4 or 6) poles; 10 slots and 8 poles are high as 0.9511.

Table 2. 2: Fundamental winding factors of 3, 4, 5 and 6 phase windings

3 phase winding					
Q|2p	2	4	6	8	10
3	0,866	0,866	-	0,866	0,866
6	-	0,866	-	0,866	0,500
9	0,328	0,617	0,866	0,945	0,945
12	-	-	-	0,866	0,933
15	0,199	0,389	-	0,711	0,866
18	-	0,328	-	0,617	0,735
4 phase winding					
Q|2p	2	4	6	8	10
4	-	-	-	-	-
8	-	-	0,924	-	0,924
12	-	-	-	-	-
16	-	-	0,545	-	0,816
20	-	-	-	-	-
24	-	-	-	-	0,595
5 phase winding					
Q|2p	2	4	6	8	10
5	0,588	0,951	0,951	0,588	-
10	-	0,588	0,809	0,951	-
15	0,205	0,401	0,588	0.732	-
20	-	-	0,448	0,588	-
25	0,123	0,245	0,362	0,474	0,588
30	-	0,205	-	0,401	-
6 phase winding					
Q|2p	2	4	6	8	10
6	-	-	-	-	-
12	-	-	-	-	0,966
18	-	-	-	-	-
24	-	-	-	-	0,605
30	-	-	-	-	-
36	-	-	-	-	0,418

The number of phases which is equal to the number of stator slots, which means that each phase at one slot can be separately supplied with a different power supply so that it operates independently of the others. It enables us to obtain a fully fault tolerant capability and therefore, the system can continue its operation even if a failure occurs.

An example for a seven-phase machine having 7 stator slots, 6 poles is given. The winding layout of double layer FSCW can be represented as follows:

The number of slots per pole per phase is:

$$q = \frac{7}{7\times 6} = \frac{1}{6}$$

There are 1 number ‘1’ and 5 number ‘0’. The one-zero sequence S_{10} is:

1 0 0 0 0 0

The complete sequence by repeating seven times of S_{10} is:

100000 100000 100000 100000 100000 100000 100000

The usual seven phase sequence AE'BF'CG'D A'EB'FC'GD' is assigned as:

1	0	0	0	0	0	**1**	0	0	0	0	0	**1**	0	0	0	0	0	**1**	0	0	0	0
A	E'	B	F'	C	G'	D	A'	E	B'	F	C'	G	D'	A	E'	B	F'	C	G'	D	A'	E

0	**1**	**0**	**0**	**0**	**0**	**0**	**1**	**0**	**0**	**0**	**0**	**0**	**1**	**0**	**0**	**0**	**0**	**0**
B'	**F**	C'	G	D'	A	E'	**B**	F'	C	G'	D	A'	**E**	B'	F	C'	G	D'

The conductors associated to the number "1" are:

A D G C F B E

The second layer is:

A' D' G' C' F' B' E'

The final winding layout is shown in Figure 2.7.

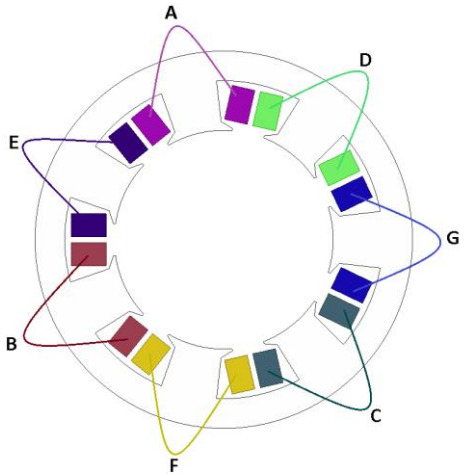

Figure 2. 7: Winding layout of 7-phase/7-slot/6-pole machine

Vector S is calculated for phase A as:

$$S = [1 \quad -2]$$

The EMF vector of the conductor corresponding to the element i of vector S is represented as:

$$\overrightarrow{E_\iota} = sign\big(S(i)\big)e^{j\pi p\left|\frac{\overrightarrow{S(\iota)}}{Q}\right|} = e^{j\frac{6\pi}{7}} - e^{2j\frac{6\pi}{7}}$$

The fundamental winding factor for double layer concentrated winding is calculated as:

$$k_{w1} = \frac{\left|\sum_{i=1}^{2Q/m}\overrightarrow{E_\iota}\right|}{2Q/m} = \frac{\left|e^{j\frac{6\pi}{7}} - e^{2j\frac{6\pi}{7}}\right|}{2} = 0.9749$$

In this case, the fundamental winding factors are presented in Table 2.3. It can be noticed that the seven-phase machines with 7 slots and (6 or 8) poles have high fundamental winding factors. For the nine-phase machine with 9 slots and (8 or 10) poles, the fundamental winding factors are 0.9848 and for the eleven-phase machine with 11 slots and (8 or 10) poles, the fundamental winding factors are higher than 0.9.

Table 2. 3: Fundamental winding factors of multiphase windings

$Q/2p$	2	4	6	8	10
3	0.8660	0.8660	-	0.8660	0.8660
4	-	-	-	-	-
5	0.5878	0.9511	0.9511	0.8090	-
6	-	-	-	-	-
7	0.4339	0.7818	0.9749	0.9749	0.7818
8	-	-	-	-	-
9	0.3420	0.6428	-	0.9848	0.9848
10	-	-	-	-	-
11	0.2817	0.5406	0.7557	0.9096	0.9898
12	-	-	-	-	-

The higher the fundamental winding factor is, the higher the EMF and the electromagnetic torque are if the machines have the same current loading and the number of turns. Fundamental winding factor higher than 0.9 is thus considered as a criterion to select the combination of phase, slot and pole. All of selected machines will be analyzed by FE method to evaluate machine performances. The optimum zero-one sequences and the layouts of one coil side of 15 phase/slot/pole combinations are presented in Table 2.4 with the number of rotor poles limited by 10.

Table 2. 4: Layouts of one coil side of selected phase/slot/pole combinations

Phase/slot/pole	Optimum zero-one sequence	Layout of one coil side
3/9/8	10010010	AA'ABB'BCC'C
3/9/10	1001001000	AA'ACC'CBB'B
3/12/10	10010	AA'B'BCC'A'ABB'C'C
4/8/6	100	ADC'BA'D'CB'
4/8/10	10000	AB'CD'A'BC'D
5/10/8	1000	ACEBDACEBD
6/12/10	10000	AEB'F'CDA'E'BFC'D'
5/5/4	1000	ACEBD
5/5/6	100000	ADBEC
7/7/6	100000	ADGCFBE
7/7/8	10000000	AEBFCGD
9/9/8	10000000	AEIDHCGBF
9/9/10	1000000000	AFBGCHDIE
11/11/8	10000000	AEIBFJCGKDH
11/11/10	1000000000	AFKEJDICHBG

2.3 WRSM Performance Comparisons

In this section, several machines with the selected phase, slot and pole combinations are designed and then compared according to three criteria: torque density, torque ripple and efficiency in order to choose an appropriate machine for our application. It is thus necessary to compute their machine performances; for that, 2D FE analysis which makes it possible to accurately evaluate electromagnetic performances of electrical machines is used.

2.3.1 2D Finite Element Design

A large number of numerical methods are considered to resolve flux equations in which FE method has been widely used in many applications. FE method is an effective tool for approximating an electromagnetic field by discretizing partial differential equations of a continuum domain into a finite number of parts known as elements. It means that the machine is divided into many small areas where the algebraic equations can be applied and solved easily using the specific numerical technique. The main advantage of FE method over analytical method for machine analysis is that it can achieve more accurate results by dealing with non-linear material behavior, complex geometry, magnetic field distribution, etc.

In this study, a salient pole synchronous machine is simulated using ANSYS Maxwell in 2D. This software makes it possible to perform magnetostatic and transient simulations for different operating conditions of the machine. In order to design the machine on the software, it is necessary to follow the steps shown in Figure 2.8.

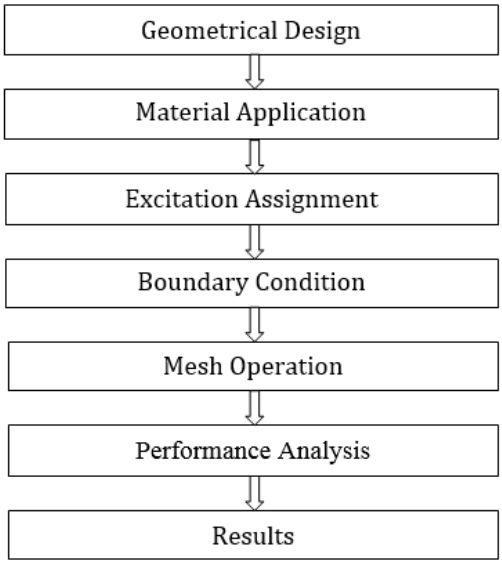

Figure 2. 8: Main steps of FE analysis

Firstly, the geometrical structure is drawn and then, material properties are assigned to various regions of the model. After that, the current sources and the boundary conditions are applied. The FE mesh is created with a selected mesh size. The analysis is carried out and finally, electromagnetic performances such as force, torque and losses are thus calculated.

The transient analysis program is utilized to solve the time variant magnetic field problems with non-linear permeability values. The mathematical formulation of magnetic field problems in closed, confined systems is based on the system of well-known Maxwell equations, by which a magnetic field is completely described. Assuming that the permeability is linear, the magnetic field distribution in an electrical machine is governed by:

$$\nabla \times \left(\frac{1}{\mu} \nabla \times A\right) = J \tag{2.10}$$

Where: A is the potential vector, J is the current density, μ is the magnetic permeability and ∇x is the rotational operator.

The vector potential formulation is used because all of the physical conditions are combined into a single equation. The current density J can be equal to 0 in the non-conductive area. In 2D, the field (B, H) is located in the plane (x, y) or (r, θ), while J and A have only one component along z. Moreover, end-winding effects are neglected. The vector potential only consists of an axial component and the magnetic field source is assumed to be constant. Therefore, the equation of the potential vector in 2D for a synchronous machine is:

$$\frac{\partial}{\partial x}\left(\nu \frac{\partial A}{\partial x}\right) + \frac{\partial}{\partial y}\left(\nu \frac{\partial A}{\partial y}\right) = J + \sigma \frac{\partial A}{\partial t} \tag{2.11}$$

Where: ν is the magnetic reluctivity and σ is the electric conductivity.

Machine structure

In order to predetermine the behavior of the machine, it is necessary to define its geometry (Figure 2.9). The two main parts of a synchronous machine are the stator and the rotor. The stator consists of a circular magnetic iron core, constructed from a thin steel sheet. The inner periphery of the stator has slots, where an armature winding is inserted. The rotor is fixed to the rotary shaft and is separated from the stationary stator by an air-gap. The rotor constructed by steel sheets includes field winding that generates magnetic field.

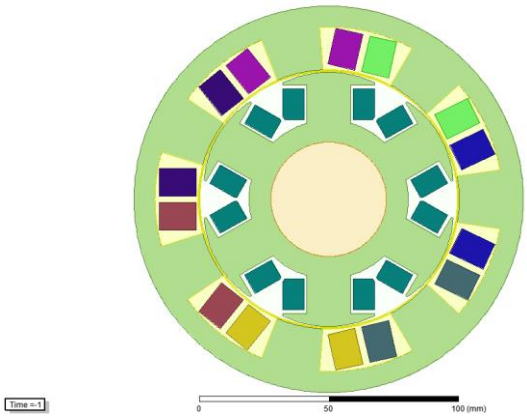

Figure 2. 9: Salient pole wound rotor synchronous machine

In theory, the torque depends on the angle between the EMF and the armature current as:

$$T_e = \frac{m \times p}{\omega}[EI_s cos(\theta_0 + \psi) + \frac{1}{2}(L_d - L_q)I_s^2 \sin 2(\theta_0 + \psi)] \quad (2.12)$$

Where: T_e is the electromagnetic torque, E is rms EMF at no load, θ_0 is the initial electrical angle of armature current, ψ is the angle between the EMF and armature current and L_d, L_q are the synchronous inductances ($L_d > L_q$) in salient pole WRSMs.

It is thus important to emphasize that to obtain the desired torque with the smallest currents, it is necessary to predetermine the initial position of the rotor of the machine [71],[72]. The simulation is carried out with the rotor rotating at nominal speed while the other parts are fixed, the rotor winding is fed with DC current and the stator windings are supplied by constant currents e.g. (I_s, -I_s/2, -I_s/2) for three-phase stator winding. The static torque vs. mechanical rotor position curve is shown in Figure 2.10.

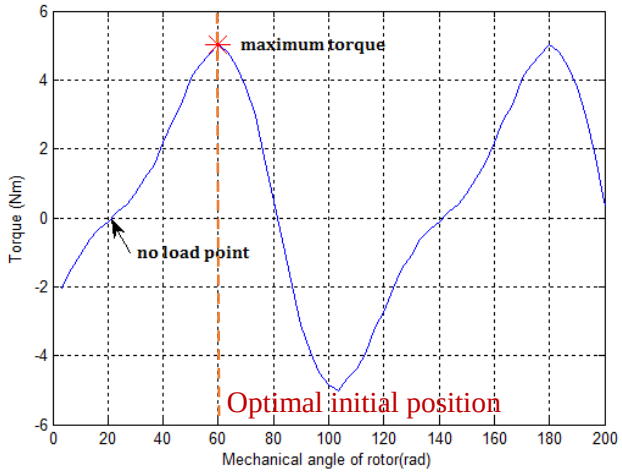

Figure 2. 10: Static torque vs. mechanical rotor angle

The initial angle of the rotor is selected as 60° for the example case since it presents the maximum torque.

Material properties

The magnetic material is important in order to determine the characteristics of the machine. There are three main regions with different types of materials. The rotor and the stator are usually manufactured with lamination. The conductive regions such as armature winding and field winding use copper. The other regions contain air, stainless steel described physically with linear magnetic properties.

Considering that the laminated yokes, steels are mainly use. Electrical steel choice considerations are based on the following factors [73], [74]:

- Reduce the magnetic iron losses over a wide speed range,
- Increase the flux density to improve the electromagnetic torque,
- At high speed operating, the mechanical properties and iron losses should be considered.

Low losses for wide frequency range

In international standards, materials are usually classified by lamination thickness and iron losses. Especially, for applications with high speed and supplied by power electronics inverters with varying switching frequencies, iron losses can become the dominant losses source. Eddy current losses increase proportionally with the square of the lamination sheet thickness.

High polarization and permeability

The operating principle of electrical machines is based on the magnetic flux density in the air-gap in electrical machines. If the core material used for the machine allows for an easier magnetization process, there will be less magnetizing current needed to achieve a high air-gap flux and hence a high torque. To achieve high torque with a low current, electrical machines are generally designed to operate just below the saturation of $B(H)$ magnetization curve of ferromagnetic materials.

High mechanical strength

For high speed machine, it is necessary to focus on yield strength level for rotor steel. The electrical steel with a high strength level for high speed rotors is important.

Thermal conductivity

High thermal conductivity allows easy evacuation of the heat. The thermal conductivity of electrical steels depends on their chemical composition and it is therefore strongly linked to their electrical resistivity, dynamic iron losses and saturation polarization.

Boundary conditions

Two boundary conditions are possible: Dirichlet condition and Neumann condition. Neumann condition imposes the normal derivative of the magnetic vector potential to zero. Homogeneous Neumann condition is defined as:

$$\partial \vec{A}/\partial n = 0 \tag{2.13}$$

Dirichlet condition specifies the initial value for the problem at a point and is part of given geometry. The boundary conditions in FE analysis of electrical machines are often the Dirichlet condition, specified in term of values imposed on a part of the surface. Assuming that the magnetic fields are constrained inside this boundary, the Homogeneous Dirichlet conditions on the outer line of the stator yoke has the $\vec{A} = 0$ shown in Figure 2.11. This condition implies that there is no leakage flux beyond this line.

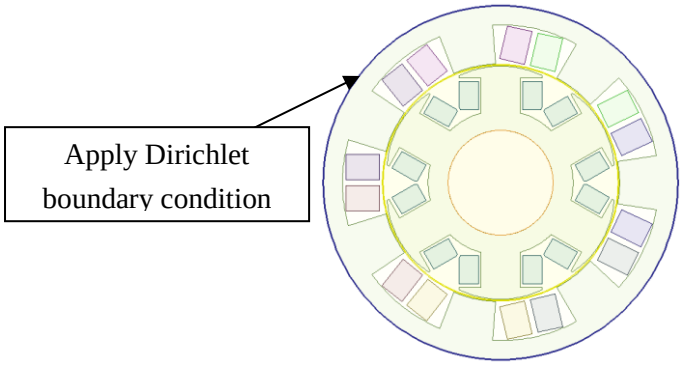

Figure 2. 11: Homogeneous Dirichlet boundary condition

Discretization

In order to analyze the machine performances, we must solve Maxwell equation to find the value of the vector potential. For doing this, it is necessary to subdivide the geometry into many small elements. This is the fundamental principle of the FE method [77], [88]. If elements are small enough, the potential vector equation is simple and easy to solve without losing accuracy. In fact, this equation is a linear function of x and y axis. Especially, the air-gap flux distribution plays an important role into an accurate computation of the magnetic flux and therefore, the torque of the machine. Moreover, the rotation of the rotor impacts the integrity of the mesh in the air-gap, which can cause the inaccuracy in the field solution. Therefore, the construction of a “moving band” in the air-gap is needed. Meshes are divided into two

parts: one moving part associated with the rotor; one fixed part associated with the stator. With the movement of the rotor provided, the nodal connection between rotor and stator are changed, and therefore, the air-gap region is re-meshed and shown in Figure 2.12.

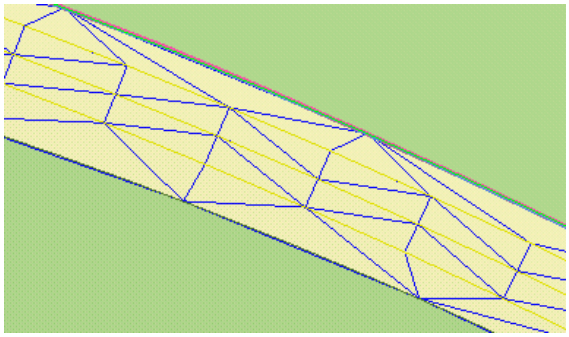

Figure 2. 12: An example of air-gap mesh

Before starting field calculations, the determination of the mesh size is very important for the accuracy of analysis results. More the mesh density is high, more the precision of the results is high, but unfortunately the computation time increases. It is thus necessary to find the best compromise between the density of the appropriate mesh and the computation time in order to obtain accurate results in a reasonable time duration. This is a main issue in the optimization process (which will be detailed in the next chapter).

Performance analysis

The design of electrical machines determines its reliability, lifetime and quality of energy provided. Those characteristics depend on the structure of the machine and the electromagnetic characteristics of the machine. FE analysis enables us to study these characteristics such as electromagnetic torque, induced voltage, losses, etc. In [76] and [77], the electromotive force and the electromagnetic torque can be calculated from the equations presented as follows:

Electromotive force calculation

The EMF induced in a winding is calculated from the flux φ:

$$E = -\frac{d\varphi}{dt} \tag{2.14}$$

Moreover, the magnetic flux passing through the section of length l and which is covered between the two points (x_1, y_1) and (x_2, y_2) is defined as:

$$\Phi = l(A_z(x_1, y_1) - A_z(x_2, y_2)) \tag{2.15}$$

In general, the proper flux of a winding is calculated from the field solution in 2D as:

$$\varphi = \frac{l}{S}\left(\sum_{n^+} \int_{S^+} A_z dS - \sum_{n^-} \int_{S^-} A_z dS\right) \tag{2.16}$$

Where: n^+, n^- are the number of positive and negative conductors, S^+, S^- are the correspondent area of conductor and A_z is the magnetic potential vector.

Electromagnetic torque calculation

There are many methods to compute the magnetic forces generated on a solid put into an electromagnetic field:

- The method of the derivative of the magnetic energy,
- The method based on the principle of local virtual work,
- The method using the Maxwell tensor.

In ANSYS Maxwell, the instantaneous electromagnetic torque is calculated by the local virtual work method. This method calculates the global and local forces [78]. In general, according to the principle of virtual work and based on the law of energy conversion into a thermodynamic system, the energy balance of an electromechanical system without losses is:

$$dW_{el} = dW + Fdx \tag{2.17}$$

Where: W_{el} is the electric energy, W is the magnetic energy, F is the applied force and x is the displacement.

The electric energy is presented as:

$$dW_{el} = eidt = I\frac{d\Phi}{dt}dt = Id\Phi \tag{2.18}$$

Where: Φ is the magnetic flux, i is the instantaneous value of the current, and e is instantaneous value of the induced voltage.

From Equation (2.18), we have:

$$id\Phi = dW + Fdx \tag{2.19}$$

The differential of the magnetic energy is given below:

$$dW = \frac{\partial W}{\partial u}dx + \frac{\partial W}{\partial \Phi}d\Phi \tag{2.20}$$

From Equations (2.19) and (2.20), the global magnetic force which is applied to the system is equal to the derivation of magnetic energy with respect to the displacement u, when the flux is considered as constant:

$$F = \left[\frac{\partial W}{\partial u}\right]_{\Phi=cste} \tag{2.21}$$

Besides, the co-energy is:

$$W_{co} + \mathrm{W} = \Phi i \tag{2.22}$$

Under the assumption of an unsaturated machine, the torque must be calculated from the variation of energy or the magnetic co-energy in the machine as:

$$F = \left[\frac{\partial W_{co}}{\partial u}\right]_{i=cste} \tag{2.23}$$

The choice of the energy or co-energy depends of the original description system. Because the current i is a controllable state variable and therefore, it is more accessible than the flux, co-energy is often chosen for calculating the value of the electromagnetic torque.

In ANSYS Maxwell, the force calculated by the virtual work method is applied to nodes in the FE mesh elements. With E_{nk} all the elements attached to the node n_k, the magnetic force applied to the node is:

$$F_{nk} = \sum_{e\in E_{nk}} F_e = \sum_{e\in E_{nk}} \left[\frac{\partial W_e}{\partial x}\right]_{\Phi=cste} = \sum_{e\in E_{nk}} \left[\frac{\partial W_{co}}{\partial x}\right]_{i=cste} \tag{2.24}$$

2.3.2 Loss and Efficiency Computation

The machine efficiency constitutes a main criterion of machine selection. As consequence, it is important to well evaluate the losses. Typically, there are three principle types of losses in electrical machines: 1) the iron losses; 2) the copper losses; and 3) the mechanical losses.

Mechanical losses

Mechanical losses include bearing friction losses, windage losses and ventilator loss. Bearing friction losses depend on the shaft speed, the bearing type, the properties of the lubricant and the load on the bearing. Windage losses are a consequence of the friction between the rotating surfaces and the surrounding gas, usually air. These losses become more significant when the speed of the machine increases. Besides bearing losses and windage losses, ventilator loss is considered in the mechanical losses. The ventilator used for cooling can be coupled to the shaft of the machine or it can be driven by another motor, as is usual in speed-controlled drives [13]. Smoother air-gap surfaces can reduce mechanical losses. In our case of low speed machine, mechanical losses can be neglected.

Iron losses

The iron losses are the losses confined in the magnetic parts of the machine, e.g. in the yoke, the pole teeth. Iron losses can be distinguished into three components: hysteresis loss, eddy current losses and excess losses [79] as:

$$p_{iron} = p_{hys} + p_{edd} + p_{ex} \tag{2.25}$$

Where: p_{iron} is the iron losses, p_{hys} is the hysteresis losses, p_{edd} is the eddy current losses and p_{ex} is the excess losses.

A magnetic material is magnetized with an increasing magnetic field H and afterwards demagnetized with an opposing magnetic field $-H$. However, the magnetization curve does not have the same path

back. The area enclosed by this hysteresis curve is equal to the specific energy for each cycle and thus proportional to the hysteresis losses.

Losses due to eddy currents in the winding are created due to the cyclic alternative magnetization. In the case of an alternating flux in the iron core, the alternation of the flux induces voltages in the conductive core and therefore, eddy currents occur in the core. They tend to resist changes in magnetic flux. The use of laminations or high resistivity compounds instead of solid ferromagnetic metal cores is considered to reduce eddy current losses.

In order to reduce iron losses, we propose some strategies as:

- Reduce the lamination thickness because eddy current losses are proportional to the square of the thickness,
- Increase the resistivity of the laminations to reduce eddy current losses.

These losses can be calculated by FE simulation. In ANSYS Maxwell, the iron losses (in watts per cubic meter) in the iron laminations is calculated [78] as:

$$p_{iron} = K_h B_{max}^2 f + K_c (B_{max} f)^2 + K_e (B_{max} f)^{1.5} \quad (2.26)$$

Where: K_h is the hysteresis coefficient, $K_c$is the classical eddy coefficient, K_e is the excess or anomalous eddy current coefficient due to magnetic domains, f is the frequency and B_{max} is maximum amplitude of the flux density.

In fact, this equation is valid under conditions of sinusoidal magnetic fields in electrical machines. In our study, the waveform of magnetic field is not really sinusoidal. However, for the moment, we use this equation due to the limitations of the available FE simulation software (ANSYS Maxwell).

Copper losses

The copper losses in electrical machines are the losses created by the current in the winding of the machine. With the assumption that the stator slots are filled with conductors which their diameters are small enough, the skin effect of AC currents at high frequency is neglected. The average length of the end-winding of non-overlapping concentrated winding is calculated by using the length of tooth and the length of machine as shown in Figures 2.13 and 2.14.

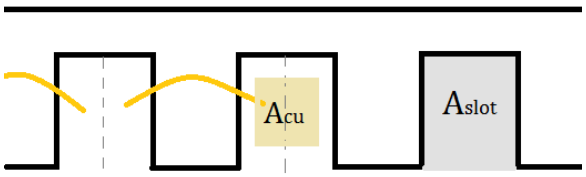

Figure 2. 13: Axial direction for stator winding

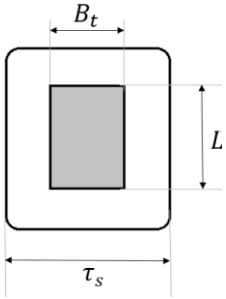

Figure 2. 14: Axial direction for stator winding

The copper losses in electrical machines are the losses created by the current in the windings of the machine. The average length of end-winding of non-overlapping concentrated winding is:

$$l_{ew} = \frac{1}{2}(2B_t + \pi\frac{\tau_s - B_t}{2}) \tag{2.27}$$

Where: l_{ew} is the end stator winding length, B_t is the width of the stator tooth, τ_s is the length of the slot pitch.

Thanks to that, the length of one coil is defined as:

$$l_{coil} = 2(L + l_{ew}) \tag{2.28}$$

Where: l_{coil} is the length of one coil, L is the length of the machine.

With the length of one conductor and the area of one conductor, the resistance of one stator slot is described by:

$$R_{slot} = \rho N_s \frac{l_{coil}}{A_{coil}} \tag{2.29}$$

Where: R_{slot} is the resistance of one slot, ρ is the conductivity coefficient, N_s is the number of the conductors per slot, and A_{coil} is the coil area calculated as:

$$A_{coil} = k_r \times A_{slot}/N_s \tag{2.30}$$

Where: k_r is the copper slot fill factor, A_{slot} is the slot area. Indeed, the copper slot fill factor affects so much on the copper area, and therefore, the slot resistance as well as the copper losses of the machine. With high copper slot fill factor, for given profiles (torque, currents, machine dimensions, etc.), the copper losses can be reduced.

Considering the resistivity of copper as a function of the temperature, ρ is calculated as:

$$\rho = \rho_o(1 + \alpha(T - 20)) \tag{2.31}$$

Where: ρ_o is the conductivity coefficient at 20°C, T is the working temperature, α is the temperature coefficient of resistance for the conductor material.

The resistance of one phase R_{ph} is:

$$R_{ph} = R_{slot} \times \frac{Q}{m} \tag{2.32}$$

Based on the value of the current I_{rms} and the resistance of one phase R_{ph}, the copper losses for m phases are determined as:

$$p_{copper} = m \times {I_{rms}}^2 R_{ph} \tag{2.33}$$

The method of rotor copper losses calculation is similar. Considering higher conducting area due to better winding technologies can reduce the resistance of the winding.

Additional losses

Additional losses are all of other electromagnetic losses which are not included in the copper losses and iron losses. It is difficult to calculate and measure the additional losses. In general, they are usually assumed to be 0.1-0.2% of the apparent power in the synchronous machine with salient poles. In Table 2.5, additional losses in the windings, frame and other parts built, etc. presented in [70] are shown.

Table 2. 5: Additional losses for different types of machine

Type of machine	Additional losses in respect to input power
Squirrel cage motor	0.3-2% (sometime up to 5%)
Slip ring asynchronous machine	0.5%
Salient pole synchronous machine	0.1-0.2%
Non salient pole synchronous machine	0.05-0.15%
DC machine without compensating winding	1%
DC machine with compensating winding	0.5%

The efficiency of the motor is determined by:

$$\eta = {P_{out}}\Big/{(P_{out} + P_{copper} + P_{iron})} \tag{2.34}$$

Where: P_{out} is the mechanical power, P_{copper} is the total copper losses of the windings, and P_{iron} is the total iron losses of the lamination cores.

2.3.3 Selection of an Appropriate WRSM

Based on FE method, several salient pole WRSMs with different phase, slot and pole combinations are analyzed. The stator windings are supplied with sinusoidal currents and the rotor winding is excited by DC current. The magnitudes of currents are adjusted in order to reach the rated torque required. The other performances of the machine such as the torque ripple, the efficiency are compared in order to select the most appropriate machine for our application.

It should be mentioned that the design choice made for electrical machines affects not only on the performance but also the manufacturing cost. Recent publications [83]-[85] demonstrated that the segmented approach can reduce the production cost, (e.g. ease in the manufacturing process, reduce material wastages because no large stator laminations must be punched), enhances fault tolerant characteristics of the machine, allows the windings to be pre-wound around each segment easily and therefore, a simple automatization of the manufacturing system. However, due to manufacture limitations and tolerances, the segments which are assembled together may cause the material degradation (the magnetic flux in the stator core is crossing multiple boundaries between individual segments, leading to the change of the flux pattern of the whole machine) and unavoidable additional air-gaps between adjacent segments, which may cause errors and defects on the electromagnetic performance if these air-gaps are large enough [85].

In Section 2.2, fifteen preferred phase/slot/pole combinations are selected based on the fundamental winding factor higher than 0.9 with the number of poles lower than 10. The FE simulations are run at 7000rpm and 5Nm to evaluate the torque ripple and the machine efficiency with the aim of finding the most appropriate machine for our application. Figures 2.15 and 2.16 show all of the machine configurations analyzed and Tables 2.6 and 2.7 represent the values linked to the criteria of comparison.

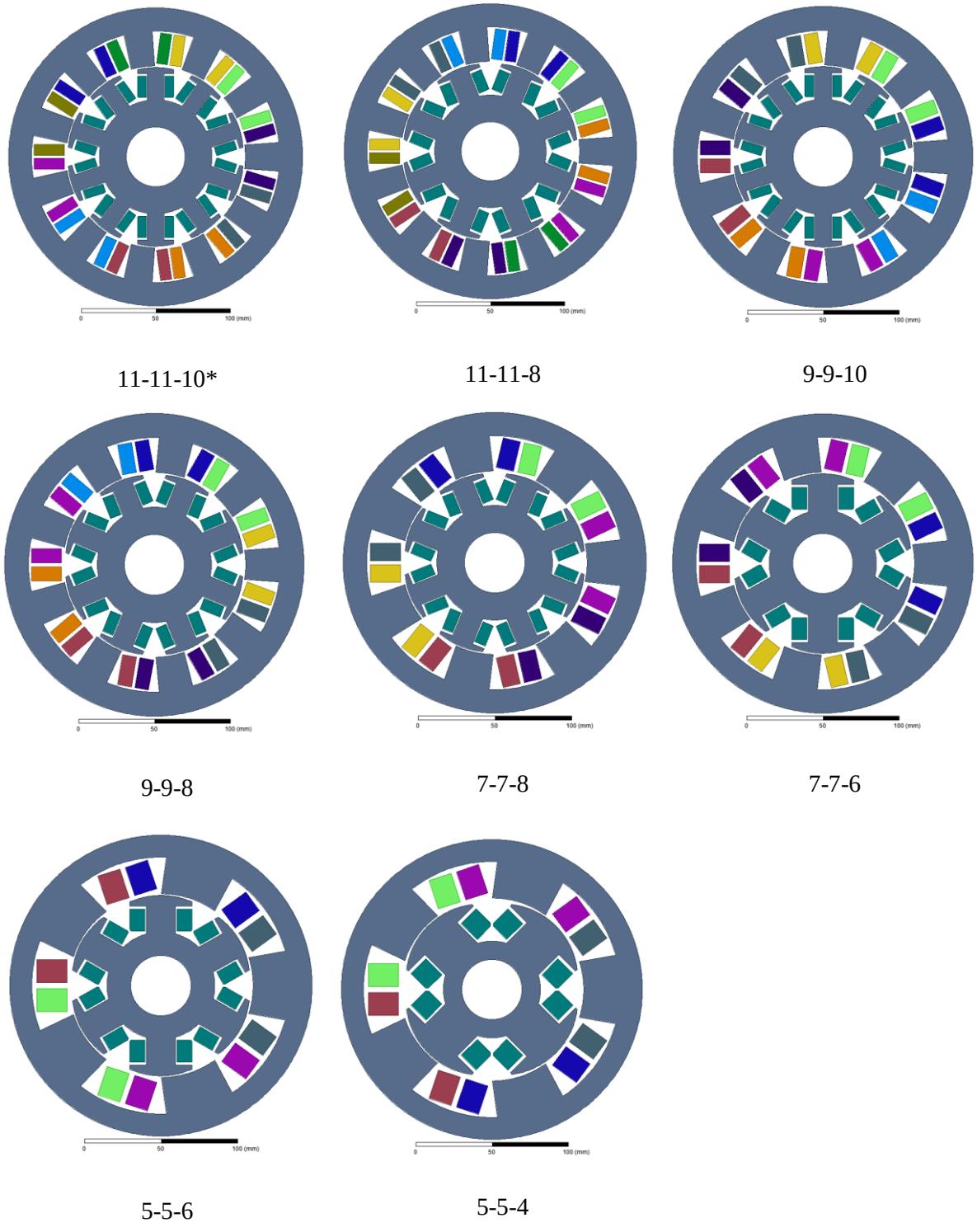

Figure 2. 15: Configurations of studied machines (* phase-slot-pole number)

Table 2. 6: Performances of the different WRSMs

	11-11-10*	**11-11-8**	**9-9-10**	**9-9-8**	**Unit**
Initial rotor position	36.72	37.80	43.20	44.10	deg
Field current	11.97	13.99	11.14	13.30	A
Peak armature current	4.26	4.42	5.00	5.00	A
Field current density	3.02	2.82	2.81	2.68	A/mm^2
Armature current density	1.39	1.44	1.35	1.34	A/mm^2
Torque ripple	**2.46%**	**2.98%**	**3.68%**	**4.78%**	
Stator copper losses	21.78	23.44	21.44	21.44	W
Rotor copper losses	42.40	38.74	36.72	34.98	W
Rotor iron losses	47.01	39.74	61.88	42.99	W
Stator core losses	57.96	75.09	58.56	52.32	W
Machine efficiency	**95.39%**	**95.20%**	**95.16%**	**95.83%**	

	7-7-8	**7-7-6**	**5-5-6**	**5-5-4**	**Unit**
Initial rotor position	56.70	55.99	41.99	66.59	deg
Field current	12.20	15.58	13.07	19.30	A
Peak armature current	5.85	5.90	7.57	7.57	A
Field current density	2.64	2.36	1.98	1.95	A/mm^2
Armature current density	1.26	1.28	1.24	1.24	A/mm^2
Torque ripple	5.62%	**4.48%**	**4.32%**	**4.77%**	
Stator copper losses	19.66	19.99	20.19	20.19	W
Rotor copper losses	29.46	28.96	20.39	22.42	W
Rotor iron losses	63.12	37.29	64.45	48.84	W
Stator core losses	68.70	52.91	88.87	86.57	W
Machine efficiency	**95.10%**	**96.15%**	**94.79%**	**95.18%**	

*Order: Number of phases – Number of stator slots – Number of poles

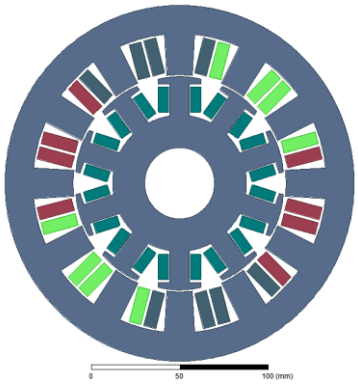

3-12-10*

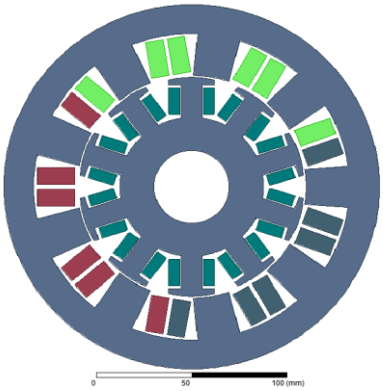

3-9-10

3-9-8

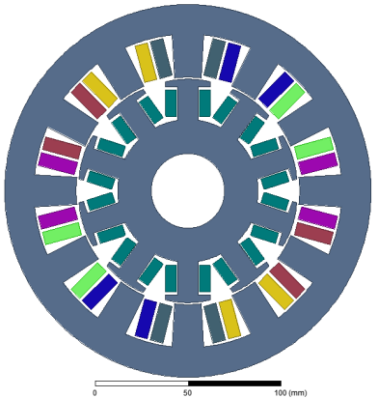

6-12-10

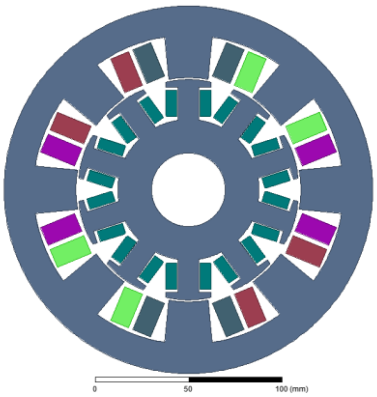

4-8-10

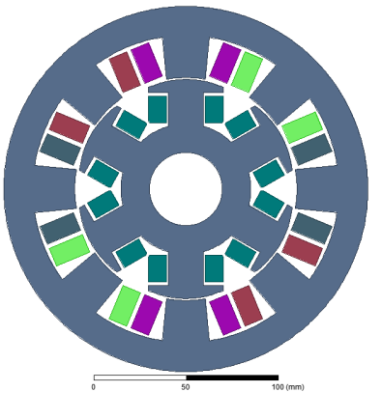

4-8-6

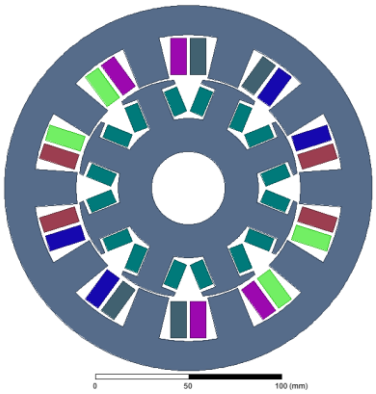

5-10-8

Figure 2. 16: Configurations of studied machines

*Order: Number of phases – Number of stator slots – Number of poles

Table 2. 7: Performances of the different WRSMs

	3-12-10*	**3-9-10**	**3-9-8**	**6-12-10**	**Unit**
Initial rotor position	30.24	46.08	40.50	35.28	deg
Field current	10.29	9.95	11.67	10.00	A
Peak armature current	4.90	5.85	5.80	4.79	A
Field current density	2.60	2.51	2.36	2.53	A/mm^2
Armature current density	1.74	1.58	1.57	1.70	A/mm^2
Torque ripple	13.91%	6.57%	8.54%	9.44%	
Stator copper losses	33.47	29.35	28.85	32.05	W
Rotor copper losses	31.36	29.31	26.94	29.62	W
Rotor iron losses	52.14	74.47	55.38	49.66	W
Stator core losses	66.81	69.08	64.68	65.08	W
Machine efficiency	**95.03%**	94.58%	**95.23%**	**95.22%**	

	4-8-10	**4-8-6**	**5-10-8**	**Unit**
Initial rotor position	50.40	49.19	18.90	deg
Field current	9.30	13.743	12.80	A
Peak armature current	6.20	6.40	5.70	A
Field current density	2.31	2.08	2.58	A/mm^2
Armature current density	1.51	1.56	1.70	A/mm^2
Torque ripple	18.19%	25.43%	81.99%	
Stator copper losses	27.25	29.03	33.19	W
Rotor copper losses	24.69	22.54	32.43	W
Rotor iron losses	97.99	42.22	52.47	W
Stator core losses	98.94	69.62	71.79	W
Machine efficiency	93.45%	**95.54%**	94.88%	

*Order: Number of phases – Number of stator slots – Number of poles

Considering that the machines are sized on the basis of the same value of active volume and same value of torque 5Nm at rated speed, the main criteria of the comparison are the machine efficiency and the torque ripple. The torque ripple is a source of noise and vibration, especially in low speed machine. Thus, the torque ripple limited to 5% is one of main criteria to select the appropriate machine.

Consequently, 7-phase/7-slot/6-pole WRSM is selected because it presents the highest efficiency (96.15%) and the torque ripple is below 5% (4.48%). This structure has a fully fault tolerant capability in which each phase at each slot can be supplied independently by each drive module.

2.4 WRSM and SM-PMSM Comparison

A comparison between the selected WRSM with a reference SM-PMSM is made in order to well evaluate the interest of this structure. A 3-phase/9-slot/8-pole SM-PMSM with non-overlapping double layer FSCW has been chosen due to its high performance provided in many studies [23]-[25]. The SM-PMSM and WRSM are re-sized on the base of the following criteria:

- Same value of the active volume,
- Same value of the torque 5 Nm at rated speed (7000rpm),
- The stator core structure, the slot type and the material are common for both two types of synchronous machines.

2.4.1 SM-PMSM Design

The parameters for the re-sized SM-PMSM are summarized in Table 2.8.

Table 2. 8: SM-PMSM stator dimension

Parameter	Value	Unit
Phase number	3	
Pole number	8	
Stator slot number	9	
Stator exterior diameter	135	mm
Stator interior diameter	72	mm
Machine length	60	mm
Air-gap length	1	mm

The dimensions of the stator slot are shown in Table 2.9 and Figure 2.17.

Table 2. 9: SM-PMSM stator slot dimension

Parameter	Value	Unit
Tooth height (H_{s2})	15	mm
Tooth tip height (H_{s01})	2	mm
Slot width (B_{s1})	16	mm
Slot width (B_{s2})	26	mm
Slot tip width (B_{s0})	5	mm
Slot radius (R_s)	0	mm

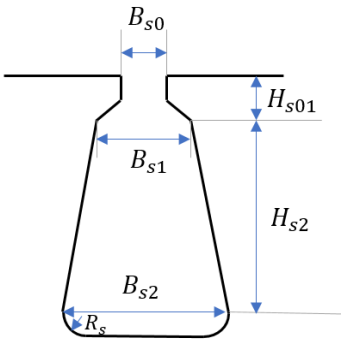

Figure 2. 17: SM-PMSM stator slot dimension

The dimensions of the permanent magnet rotor are presented in the Table 2.10.

Table 2. 10: SM-PMSM rotor dimension

Parameter	Value	Unit
Shaft diameter	36	mm
Rotor interior diameter	70	mm
Magnet thickness	3.5	mm
Magnet embrace ratio	0.6	

The parameters of the winding are shown in Table 2.11.

Table 2. 11: SM-PMSM stator winding parameters

Parameter	Value
Layer number	2
Turn number per layer	75
Stator slot fill factor	0.6

DW310-35 material in the Maxwell library is used for both rotor and stator. The $B(H)$ curve of this material is shown in Figure 2.18.

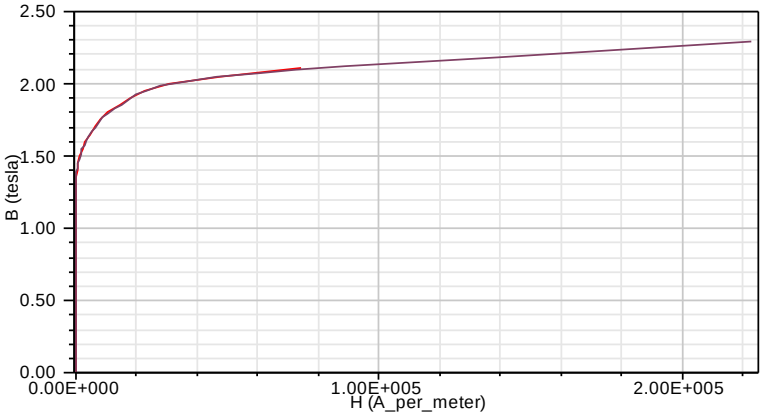

Figure 2. 18: $B(H)$ curve of DW310-35 material

The numerical simulation provides the induction of the machine shown in the Figure 2.19.

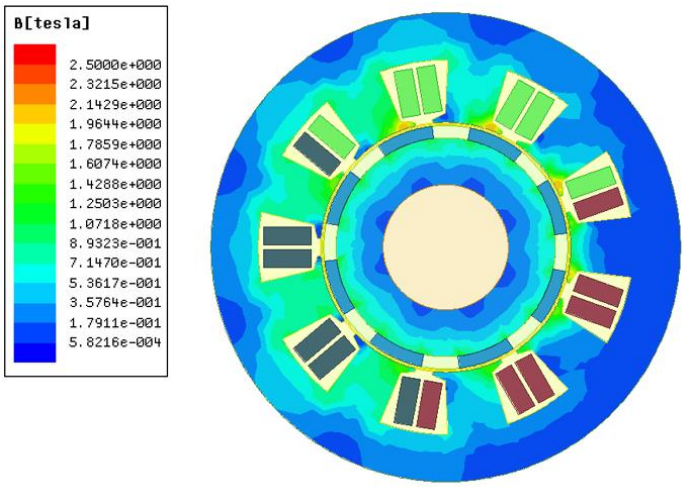

Figure 2. 19: Stator and rotor induction of the SM-PMSM

The performances of SM-PMSM at 7000rpm are indicated in Table 2.12. The waveforms of armature current, voltage, torque, eddy current losses, core losses are shown in Annex 1.

Table 2. 12: SM-PMSM performances

Performance	Value	Unit
Active volume	5.92×10^5	mm^3
Armature current	3.544	A
Phase voltage	369.55	V
Output power	3.6674	kW
Average torque	5.0029	Nm
Torque ripple	**4.71%**	
Efficiency	**95.66%**	

2.4.2 WRSM Design

The parameter of the WRSM is indicated in Table 2.13.

Table 2. 13: WRSM stator dimension

Parameter	Value	Unit
Phase number	7	
Pole number	6	
Stator slot number	7	
Stator exterior diameter	152	mm
Stator interior diameter	102	mm
Machine length	60	mm
Air-gap length	1	mm

Figure 2.20 shows the shape of the stator. The dimension of stator slot is shown in Table 2.14.

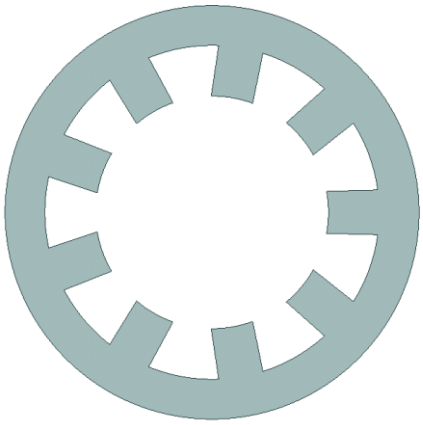

Figure 2. 20: Cylindrical stator of WRSM

Table 2. 14: WRSM stator slot dimension

Parameter	Value	Unit
Tooth height (H_{s2})	16	mm
Tooth tip height (H_{s01})	0	mm
Slot width (B_{s1})	27	mm
Slot width (B_{s2})	37	mm
Slot tip width (B_{s0})	0	mm
Slot radius (R_s)	0	mm

The shape of the rotor is shown in Figures 2.21 and 2.22. The geometrical parameters of salient pole rotor are summarized in Table 2.15.

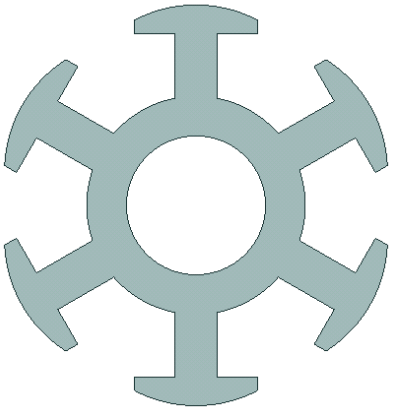

Figure 2. 21: WRSM rotor in 2D

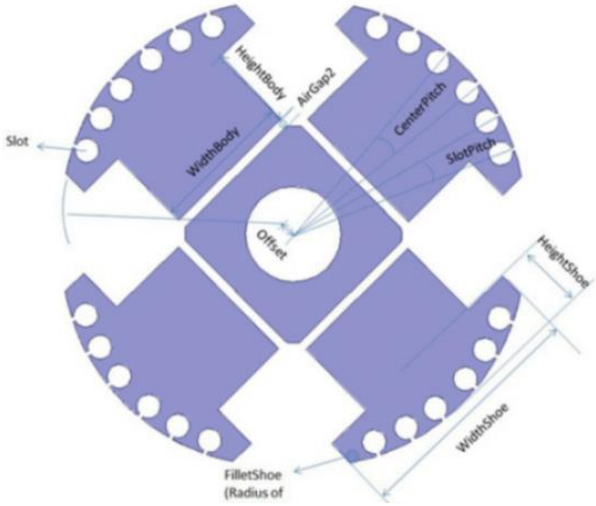

Figure 2. 22: Salient pole rotor [21]

Table 2. 15: WRSM rotor dimension

Parameter	Value	Unit
Shaft diameter	45	mm
Rotor diameter	100	mm
Pole shoe width	35.60	mm
Pole shoe height	5	mm
Pole body width	17	mm
Pole body height	15.13	mm
Pole arc offset	10	mm

The parameters of the winding are shown in Tables 2.16 and 2.17.

Table 2. 16: WRSM stator winding parameters

Parameter	Value
Layer number	2
Turn number per layer	189
Stator slot fill factor	0.6

Table 2. 17: WRSM rotor winding parameters

Parameter	Value
Turn number per pole	100
Rotor slot fill factor	0.6

Assuming that the natural air-cooled machine design, the maximum current density is set to less than $6.5A/mm^2$ for the stator winding and $4A/mm^2$ for the rotor winding. By considering the manufacturing of the machine, the copper slot fill factors of the field winding and the armature winding are set to 0.6 in which the slot area and the area between two rotor poles are indicated in Figures 2.23 and 2.24.

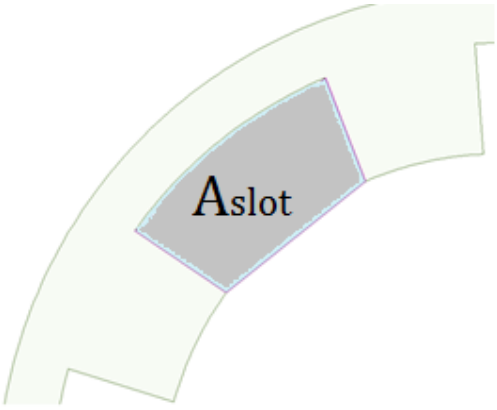

Figure 2. 23: WRSM slot area

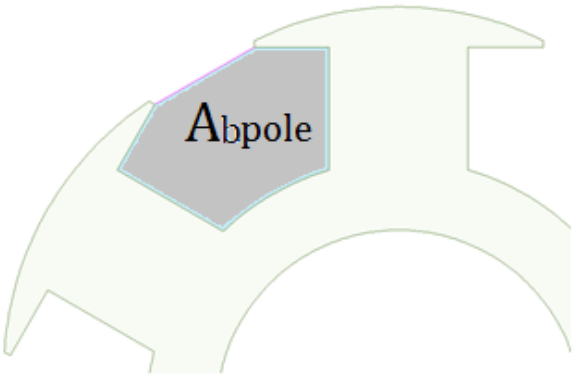

Figure 2. 24: Area between two rotor poles

The numerical simulation provides the induction of the machine shown in Figure 2.25 with a small saturation on the pole shoe.

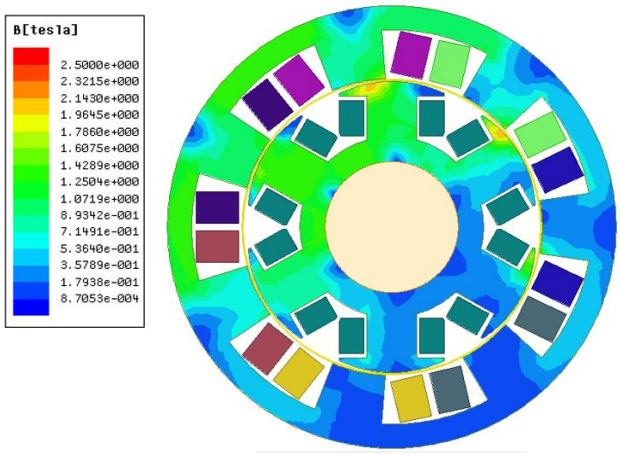

Figure 2. 25: Stator and rotor induction of the WRSM

The performances of WRSM at 7000rpm are presented in Table 2.18. The waveforms of armature current, voltage, torque, core losses are shown in Annex 1. The waveform of the induced voltage is not sinusoidal due to MMF harmonic components.

Table 2. 18: Machine performances of the designed WRSM

Performance	Value	Unit
Active volume	5.92×10^5	mm^3
Field current	3.616	A
Armature current	2.912	A
Phase voltage	369.43	V
Output power	3.6671	kW
Torque	5.0026	Nm
Torque ripple	**3.89%**	
Efficiency	**95.03%**	

Table 2.19 gives the difference between the performances provided by the SM-PMSM and the WRSM computed as:

$$value = \frac{X_{WRSM} - X_{PMSM}}{X_{PMSM}} * 100\ \% \tag{2.35}$$

Table 2. 19: Comparison performances between SM-PMSM and WRSM

Performance	Value
Armature current	-17%
Torque ripple	-17%
Efficiency	-0.6%

At 7000rpm, the torque ripple of both WRSM and SM-PMSM is low. In addition, the efficiency of WRSM is lower than that of SM-PMSM due to higher copper losses presented in WRSM. The performances of the WRSM at rated speed are close to the SM-PMSM performances.

2.4.3 Torque Speed Characteristics

The motor has two operation regions: a constant torque region and a constant power region. The constant torque region operates from standstill to the base speed. In this region, the inverter operates using the PWM mode to supply adjustable voltage and frequency to the motor. The AC voltage is adjusted as speed (frequency) changes to maintain constant flux density in the motor. The AC voltage, basically increases proportionally with the speed. This produces the nearly constant torque. Of course, the output power is proportional to the speed, so the output power increases linearly with the machine speed. In constant power region, the AC voltage reaches its maximum value because of the limit of the voltage source (battery, etc.). This decreases the flux density and the torque as the reciprocal of speed, while power out of the motor is nearly constant.

SM-PMSM torque speed curve

Assuming the limitation of the voltage source is about 370V, the numerical simulations for different operating points are carried out in order to estimate the machine performances. Varying the armature current and the initial rotor angle, the torque and the efficiency are analyzed in Annex 2. The torque speed characteristics are shown in Figures 2.26 - 2.28. It can be seen that the constant power region of SM-PMSM is not wide (from 5000rpm to 8000rpm). Moreover, the machine efficiency at overload is lower due to the increase of stator copper losses.

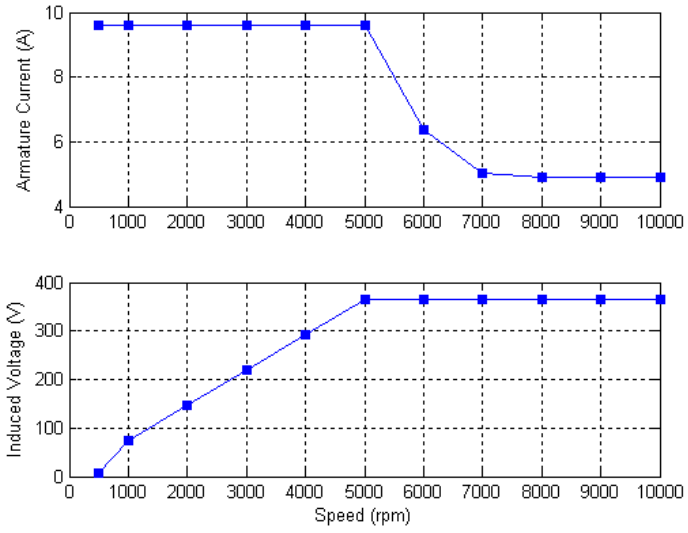

Figure 2. 26: Armature current and voltage of SM-PMSM

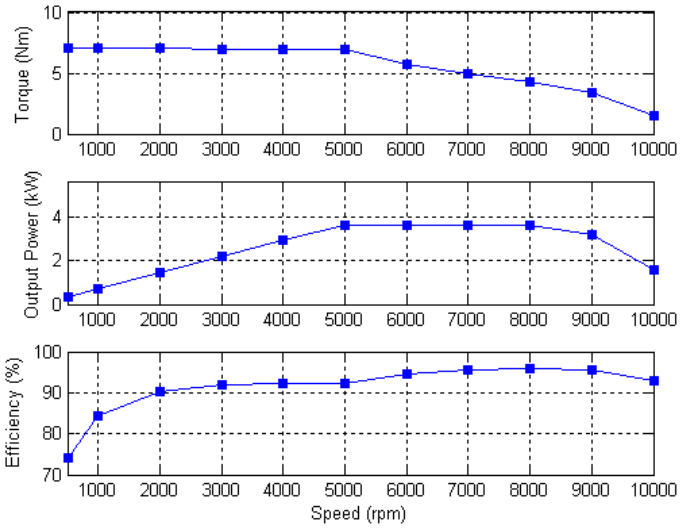

Figure 2. 27: Torque power and efficiency of SM-PMSM

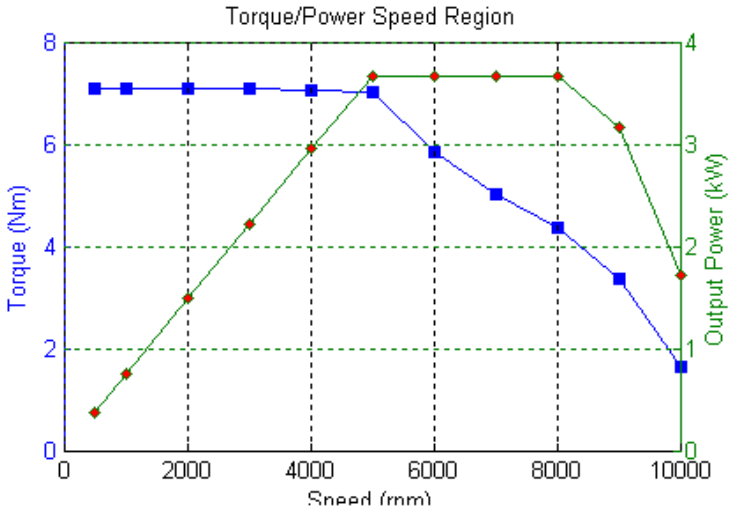

Figure 2. 28: Torque and power vs. speed of SM-PMSM

WRSM torque speed curve

The machine performances of the WRSM for different operating points are analyzed and shown in Annex 2. The currents, the induced voltage, the average torque and the output power vs. speed curves are indicated in Figures 2.29 - 2.31.

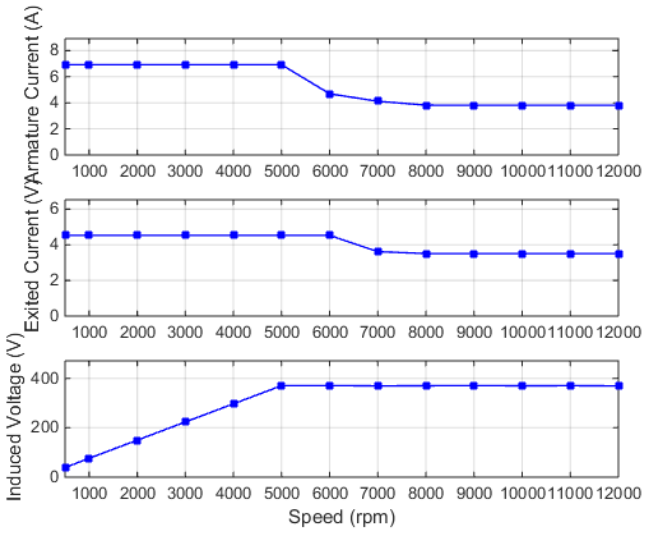

Figure 2. 29: Armature/field currents and voltage of the WRSM

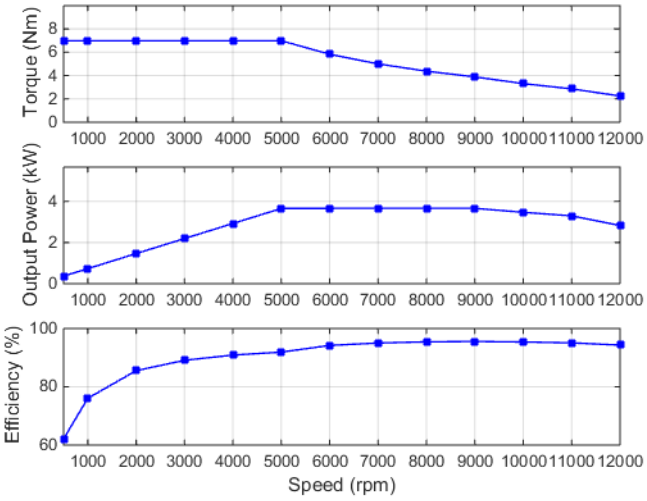

Figure 2. 30: Torque, power and efficiency of the WRSM

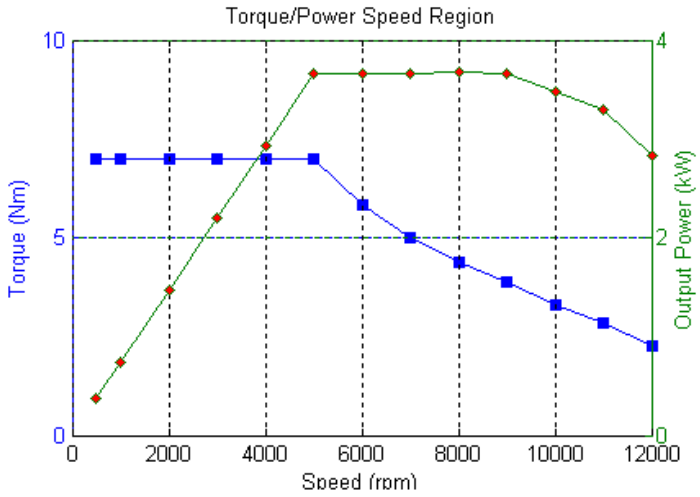

Figure 2. 31: Torque/power vs. speed of the WRSM

WRSM and SM-PMSM torque speed comparison

The comparisons of the torque, the output power and the efficiency for different operating points between WRSM and SM-PMSM are shown in Figures 2.32 - 2.34.

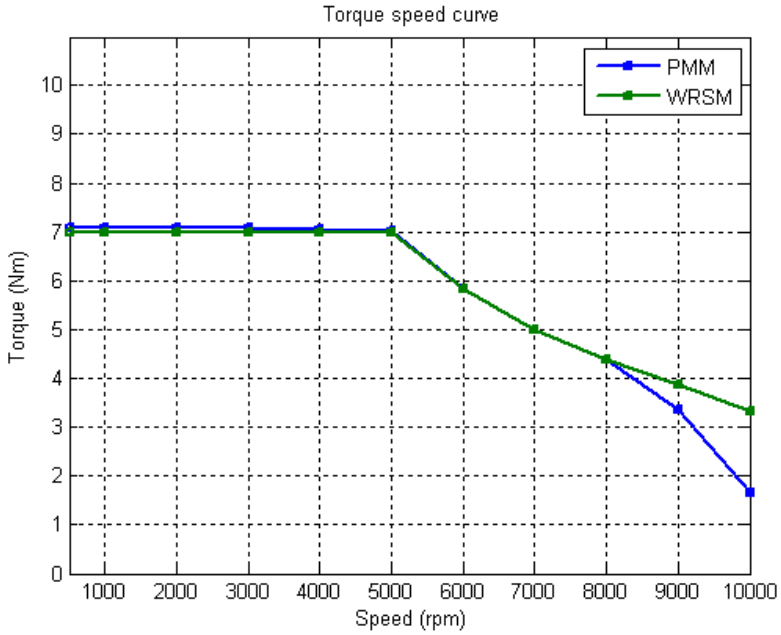

Figure 2. 32: Torque vs. speed of the SM-PMSM and WRSM

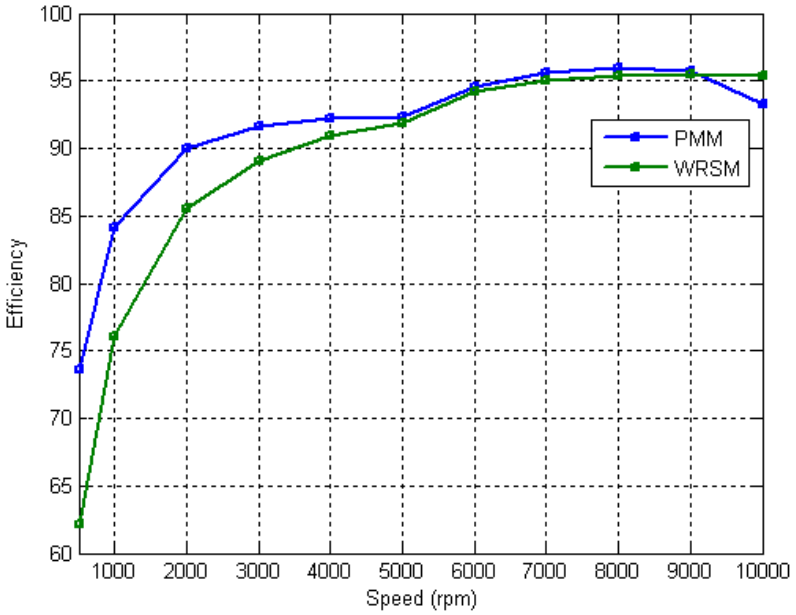

Figure 2. 33: Efficiency vs. speed of the SM-PMSM and WSRM

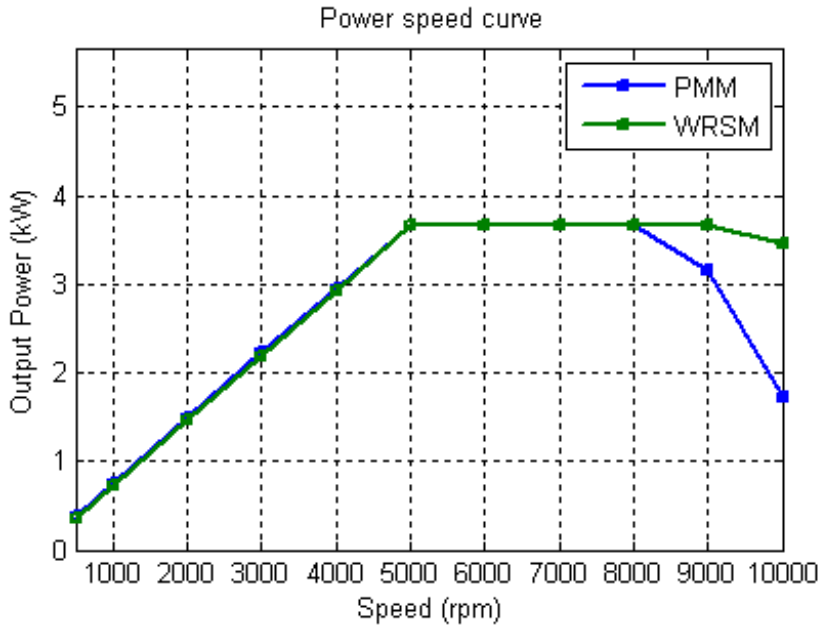

Figure 2. 34: Power vs. speed of the SM-PMSM and WRSM

As can be seen in Figures 2.33 and 2.34, from a speed of 8000rpm, the output power and the machine efficiency of WRSM have a tendency to be better compared to the SM-PMSM. It should be noticed that the constant power region of the WRSM is wider than the SM-PMSM one due to the possibility in decreasing the field current density.

The efficiency and the torque ripple at several speeds are summarized in Table 2.20. It can be seen that the torque ripple of the WRSM is typically lower than the one of the SM-PMSM and at high speed, the efficiency of the WRSM seems to be higher than the one of the SM-PMSM. However, the efficiency at low speed of the WRSM is lower than the SM-PMSM efficiency. This can be explained that for the same active volume, the flux generated by the rotor winding is maybe smaller than the flux generated by the magnet material. In order to obtain the same value of torque, the stator winding of WRSM must generate high flux so that the copper losses of WRSM are significant.

Table 2. 20: Performance comparisons between WRSM and SM-PMSM at specific speeds

Speed	Performance	WRSM (%)	SM-PMSM (%)
5000 rpm (Based speed)	Efficiency	91.90	92.33
	Torque ripple	2.74	3.72
7000rpm (Rated speed)	Efficiency	95.03	95.66
	Torque ripple	3.89	4.71
10000rpm	Efficiency	95.37	93.28
	Torque ripple	6.60	12.61

2.5 Heptagonal based WRSM

For the POKI-POKI^{TM} machine type, the stator consists of a number of the segments. Each segment includes integrated yoke segment and stator tooth with its own winding as shown in Figures 2.35 – 2.36.

Figure 2. 35: An example of one segment of the 11kW high speed PMSM [86]

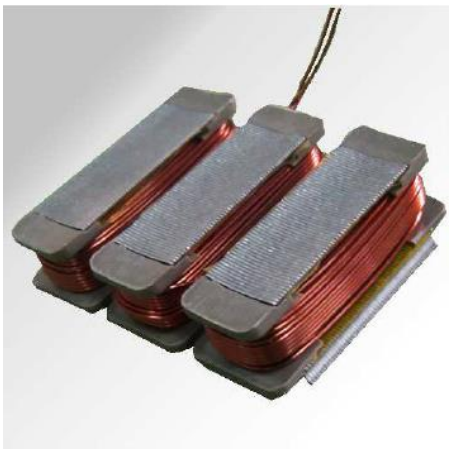

Figure 2. 36: Tooth winding coils wound on stator segments [87]

The winding is automatically wound around the tooth for each segment before the stator are formed and press fitted into a frame. Hence, the winding has a high slot fill factor with a segmented stator. However, because it was the first time that we construct those kind of machines in the laboratory, it is difficult to make sure that we can obtain the high slot fill factor of 0.5 for the stator winding. Considering that we can only obtain the slot fill factor of the stator winding is 0.4 if the slot width is large. Therefore, a new machine based on a heptagonal structure is proposed. This new structure enables increasing the slot fill factor and provides more space to integrate the power converters on the machine frame. Two types of WRSM with different stator forms are represented in Figures 2.37 and 2.38.

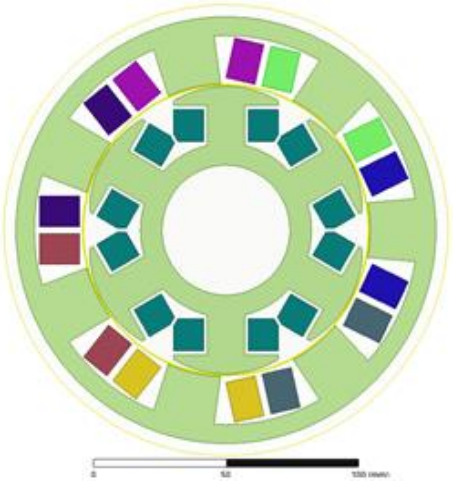

Figure 2. 37: Cylindrical based WRSM

Figure 2. 38: Heptagonal based WRSM

The performances of two machines shown in Table 2.21 are compared to consider the advantages and the drawbacks of the new machine with the heptagonal stator. In this case, the exterior volume of the heptagonal based WRSM is 4.9% higher compared to the exterior volume of the conventional (cylindrical) WRSM.

Table 2. 21: Comparison of cylindrical and heptagonal based WRSMs

Performance	**Cylindrical based WRSM**	**Cylindrical based WRSM**	**Heptagonal based WRSM**
Stator slot fill factor	0.4	0.5	0.5
Average torque (Nm)	3.99	4.98	4.95
Torque ripple (%)	3.06	4.76	5.15
Total losses (W)	116.88	138.23	144.57
Exterior volume ($10^6 mm^3$)	1.1681	1.1681	1.2281

With a stator slot fill factor of 0.4, the performances of the conventional WRSM are not as good as that of the heptagonal new machine which has a stator slot fill factor about 0.5. Nevertheless, if the slot fill factor of the conventional WRSM is increased to 0.5, the performances of the conventional WRSM are a little better than the heptagonal based WRSM performances with a higher mean torque and a lower torque ripple. Due to the easiness of production and equivalent performances, we decide to study the heptagonal WRSM. This machine will be optimized in order to minimize the exterior volume using a numerical optimization algorithm as we will see in the next chapter.

2.6 Chapter conclusion

This chapter provides the simulation performances of new MB-WRSMs using multiphase non-overlapping double layer FSCW. Firstly, the fundamental winding factor is calculated as a criterion to select the preferred numbers of phases, stator slots and poles. With the limited number of poles for a small machine (3.67kW/7000rpm), 15 different machines for different phase/slot/pole combinations are analyzed using 2D FE method and compared according to three criteria: torque density, torque ripple and machine efficiency. The 7-phase/7-slot/6-pole WRSM is chosen with the best compromise of high torque density, small torque ripple and highest nominal efficiency. This machine is then compared with a reference design SM-PMSM. The simulation results are discussed and they demonstrate that the MB-WRSM has potential to replace PMSM in HVAC application since it presents similar performances with high fault tolerance capability. Finally, considering the requirements of prototype manufacturing, the heptagonal base WRSM is studied.

Chapter 3

Optimization of the WRSM Design

In Chapter 2, we provide an electromagnetic analysis of MB-WRSMs. The machines with the fundamental winding factors higher than 0.9 were selected and then analyzed by using FE method. The stator windings were fed with a sinusoidal current source and the rotor winding was excited with a DC current in order to obtain the target value of torque density. The machine performances such as the torque ripple, the machine efficiency were compared and therefore, the 7-phase/7-slot/6-pole machine was selected for our application. A heptagonal stator for the WRSM was proposed in Chapter 2 in order to increase the copper slot fill factor and to have more space for integrating the power converters.

In this chapter, the optimization of a WRSM design is presented. In order to perform the optimization process, an optimization-based model is introduced and an optimization algorithm is selected. Finally, a 2D electromagnetic validation and an evaluation of the optimal result shape are carried out.

3.1 Optimization Model

The basic components of our optimization problem are a set of fixed parameters and variables, a mono-objective function and a set of constraints. The goal of the optimization problem is to find the value of the variables that minimize the objective function while satisfying the constraints.

In our case, the objective function is the external volume which is well analytically defined; however, the constraints such as the average torque, the iron losses, and the phase voltage are evaluated using an expensive simulation tool which is based on FE method via ANSYS Maxwell software.

3.1.1 Fixed Parameters

Several parameters are fixed or estimated based on the application and the design such as:

- A rated speed of 7000rpm is selected for the HVAC application.
- The designed prototype is a 7-phase/7-slot/6-pole machine with FSCW, see Chapter 2.
- Standard non-grain-oriented electrical steel for both the stator and the rotor is M330-35A. This lamination has good magnetic characteristics such as high permeability and low loss density.
- Air-gap length, copper slot fill factors for field and armature windings are considered as fixed parameters. Their values are determined due to the limit of the prototype manufacturing.

This imposes a NLP optimization problem instead of a MINLP one which is numerically more complicated to solve.

3.1.2 Design Variables

The goal of the design optimization is to determine the optimal dimensions of the machine. Two different optimizations are proposed, the first one is a WRSM with a cylindrical shape stator and a second one with a heptagonal stator. All of the geometrical variables of the stator are shown in Figures 3.1 and 3.2. The width of the tooth (B_t), the height of the tooth (H_t), the height of the stator yoke (H_{ys}) are the parameters that define the stator for both shapes.

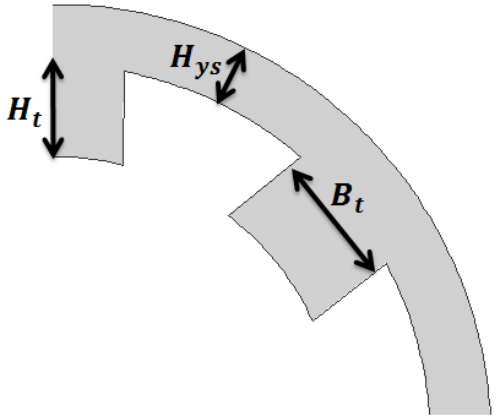

Figure 3. 1: The cylindrical stator variables

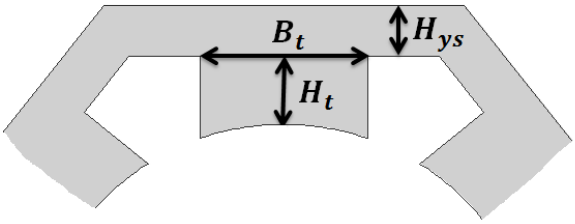

Figure 3. 2: The heptagonal stator variables

The geometrical variables of the rotor shown in Figure 3.3 include the height of the rotor yoke (H_{yr}), the diameter of the shaft (D_{sh}), and the dimensions of the rotor poles such as the width of the pole body (W_b), the height of the pole body (H_b), the width of the pole shoe (W_s), and the height of the pole shoe (H_s), the pole arc offset ($offset$). The pole arc offset is usually used to vary the shape of the pole shoe; a parameter affects the value of the torque ripple.

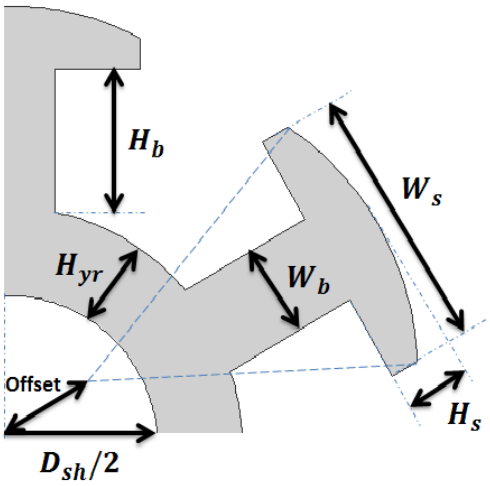

Figure 3. 3: The geometrical variables of the rotor

The other parameters of the machine such as the diameter of the rotor D_r, the diameter of the stator D_h (for two both stators; for the heptagonal stator, D_h is the distance which is used to calculate the external volume) are calculated as:

$$D_r = D_{sh} + 2 \times H_{yr} + 2 \times H_b + 2 \times H_s \tag{3.1}$$

$$D_h = D_r + 2 \times e + 2 \times H_t + 2 \times H_{ys} \tag{3.2}$$

Where: e is the air-gap length.

Furthermore, we have four variables in order to represent the supply source such as the current densities and the conductor numbers of the windings. All of the optimization variables are thus presented in Table 3.1.

Table 3. 1: Fixed parameters for the optimization

Name	Symbol	Unit
Machine length	L	mm
Stator yoke height	H_{ys}	mm
Tooth height	H_t	mm
Tooth width	B_t	mm
Rotor yoke height	H_{yr}	mm
Pole shoe height	H_s	mm
Pole shoe width	W_s	mm
Pole body height	H_b	mm
Pole body width	W_b	mm
Pole arc offset	$Offset$	mm
Shaft diameter	D_{sh}	mm
Armature current density	J_{cu_s}	A/mm^2
Field current density	J_{cu_r}	A/mm^2
Stator conductor number	N_s	
Rotor conductor number	N_r	

3.1.3 Objective Function

The objective function expresses the main goal of the optimization model which has to be minimized; in this thesis we only deal with a mono-objective function. Our optimization objective is the external volume of the machine.

Cylindrical stator, see Figure 3.4:

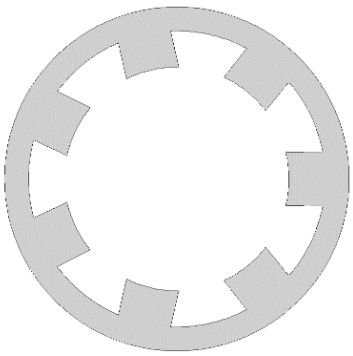

Figure 3. 4: Cylindrical stator of the WRSM

Without the zone of end-winding, the external volume of the machine is calculated as follows:

$$V_{ext}^{c} = {}^{\pi D_h^2}/_{4} \times L \tag{3.3}$$

The axial height of one side end-winding h_{ew} is calculated as:

$$h_{ew} = max(^{B_{s1} + B_{s2}}/_{2}; W_s - W_b) \tag{3.4}$$

Where: B_{s2} and B_{s1} are the largest and smallest widths of the stator slot calculated thanks to the interior diameter of the stator D_{is} as:

$$B_{s1} = {}^{\pi D_{is}}/_{7} - B_t \tag{3.5}$$

$$B_{s2} = {}^{\pi(D_{is} + 2H_t)}/_{7} - B_t \tag{3.6}$$

By taken into account the end-winding zone, the external volume of the machine is defined as:

$$V_{ext\_ew}^{c} = {}^{\pi D_h^2}/_{4} \times (L + h_{ew}) \tag{3.7}$$

Heptagonal stator, see Figure 3.5:

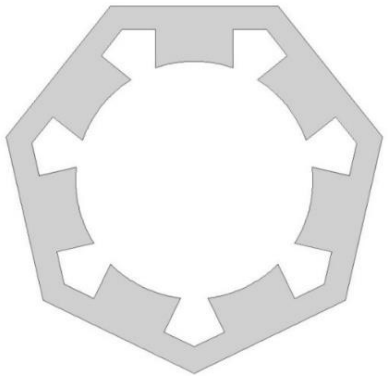

Figure 3. 5: Heptagonal stator of the WRSM

Without the zone of end-winding, the external volume of the machine is calculated as:

$$V_{ext}^{h} = 7 \times (\frac{D_h}{2})^2 \times \tan\left(\frac{\pi}{7}\right) \times L \tag{3.8}$$

Taken into account the end-winding zone, the external volume of the machine is defined as:

$$V_{ext\_ew}^{h} = 7 \times (\frac{D_h}{2})^2 \times \tan\left(\frac{\pi}{7}\right) \times (L + h_{ew}) \tag{3.9}$$

Where: h_{ew} is the axial height of the one side end-winding calculated as above in the case of a cylindrical stator.

3.1.4 Constraints

The machine specifications required for our application such as the average torque which equals to 5Nm, the torque ripple limited by 5% for realistic operation, the peak value of the phase voltage lower than 800V due to the control requirement, the machine efficiency higher than 94% and the temperature of the coil lower than 105°C for ensuring the integration of the power converters without cooling system are considered as our constraints. In addition, several mechanical and geometrical constraints need to be considered.

The average value of electromagnetic torque T_{em}, the phase voltage and the core losses are computed based on a FE modelling where a large number of simulations are ran for different time steps corresponding to two electrical periods. The torque ripple ΔT is defined by:

$$\Delta T = {(T_{max} - T_{min})}/{T_{em}} \tag{3.10}$$

Where: T_{max} is the maximal value of the torque, T_{min} is the minimal value of the torque.

It should be emphasized that the numerical optimization which carries out the number of FE simulations requires too much time. Indeed, the computational time is about 20 minutes, in our computer configuration, for only one FE simulation (120 rotor positions and a large mesh size) in order to compute the electromagnetic torque (the average value T_{em}^{120p}) and the iron losses with an acceptable error. With the aim of reducing the computational time, the machine is only analyzed at some rotor positions (here, four rotor positions with the same large mesh size) to obtain the average torque T_{em}^{4p} (relative error ≤ 1%) with the simplified torque ripple ΔT^{4p}. In this case, the torque ripple is not precise enough and validation steps has to be provided afterwards.

For the mechanical constraint, the highest stress caused by the centrifugal force in the rotor is proportional to the square of the angular speed as:

$$\rho_m r_r^2 \Omega^2 < s \times \sigma \tag{3.11}$$

Where: σ is the maximal mechanical stress (370N/mm^2 for M330-35A), s is the safety factor, r_r is the radius of the rotor, Ω is the mechanical angular speed, ρ_m is the density of the material. The maximum radius of the rotor is determined thanks to this equation with a specific maximal mechanical stress of the material.

Furthermore, several geometrical constraints are considered in our optimization. For the rotor, the pole shoe width should be limited according to a compromise between leaving enough room for the field coils and limiting the interpole flux linkage:

$$\propto = {W_s}/{\tau_p} < 0.85 \tag{3.12}$$

Where: τ_p is the pole pitch.

In order to avoid the saturation of magnetic induction, the pole body width is limited as:

$$0.2 \leq {W_b}/{W_s} \leq 0.9 \tag{3.13}$$

For the stator, the tooth width per slot pitch is defined in order to have the space for the armature winding as:

$${(\tau_z - B_t)}/{\tau_z} \geq 0.25 \tag{3.14}$$

Where: τ_z is the slot pitch.

In order to avoid the saturation of the magnetic induction in the stator tooth, the tooth height is limited as:

$${H_t}/{B_{s1}} \geq 0.25 \tag{3.15}$$

Where: B_{s1} is the smallest width of the stator slot.

Considering the robustness of the numerical parametric model, the other geometrical dimensions are computed from the values of the variables and the fixed parameters must be positive.

The list of constraints is summarized in Table 3.2.

Table 3. 2: Optimization constraints

Symbol	Name	Relation
C_1	Average torque	$T_{em} = 5\ Nm$
C_2	Torque ripple	$\Delta T \leq 5\%$
C_3	Peak phase voltage	$V_{peak} \leq 800$ V
C_4	Machine efficiency	$\eta \geq 94\%$
C_5	Coil temperature	$T_{coil} \leq 105°C$
C_6	Maximal stress	$\rho_m r_r^2 \Omega^2 < s \times \sigma$

3.2 Comparison of Two Optimization Algorithms

There is no ideal optimization algorithm which is well adapted for solving our design problem. Due to the constraints which have to be computed with expensive FE numerical simulations, the optimization is less efficient. In this study, we use and compare two distinct software: *fmincon* from the Matlab optimization toolbox and NOMAD form the GERAD laboratory with the objective of selecting an appropriate algorithm for our optimization problem, see Chapter 1 for explanations on those algorithms.

Considering that our optimization problem is hard to solve directly (because of high computational time on each evaluations), some relaxations are proposed in order to test the two different optimization

methods. For reducing the computational time, the relaxation use the average torque T_{em}^{4p} for the torque constraint with the simplified torque ripple with respect to $\Delta T^{4p} \leq \Delta T \leq 5\%$. Based on that, the relaxed

optimization problem ($\boldsymbol{\mathcal{P}_{R1}}$) is established to minimize the external volume of the cylindrical machine without the end-zone of the machine as:

$$(\boldsymbol{\mathcal{P}_{R1}}) = \begin{cases} \min & V_{ext}^{c} \\ x \in \mathcal{B}^{14} & \\ Under\ Constraints: & \\ & T_{em}^{4p} = 5Nm \\ & \Delta T^{4p} \leq 5\% \\ & \rho_m r_r^2 \Omega^2 < s \times \sigma \\ & geometrical\ constraints \end{cases} \tag{3.16}$$

In this case, the diameter of the shaft is fixed with a constant ratio compared to the diameter of the rotor considering the machine fabrication. In order to evaluate the efficiency of the two optimization methods, the maximum and minimum boundaries for the variables are the same for both optimizations. By using a reference machine (designed in Chapter 2 which was used to compare WRSM with SM-PMSM) with the external volume of $1.0888 \times 10^6\ mm^3$ as a starting point, two optimization methods for the relaxed problem ($\boldsymbol{\mathcal{P}_{R1}}$) provide different results. Considering *fmincon* solver, only the interior-point algorithm converges and makes it possible to obtain solutions for our design problem. The optimal results are achieved and verified with a fine mesh size for both methods. These results are shown in Table 3.3.

Table 3. 3: Optimal (local) solutions of ($\boldsymbol{\mathcal{P}_{R1}}$) problem

Performance	Symbol	*fmincon*	NOMAD	Unit
Average torque	T_{em}	5.00	5.00	Nm
Torque ripple	ΔT	1.58%	0.57%	
Efficiency	η	94.17%	69.04%	
Peak phase voltage	V_{peak}	357.05	316.79	V
Rotor current density	J_{cu_r}	3.56	21.30	A/mm^2
Stator current density	J_{cu_s}	3.85	72.49	A/mm^2
External volume	$\boldsymbol{V_{ext}^{c}}$	**9.9793**	**2.0412**	$\boldsymbol{10^5\ mm^3}$

By using *fmincon* method, the minimal exterior volume is smaller about 8.44% compared to the initial value of the starting point. Using NOMAD method, the minimal exterior volume is smaller about 81.28% than the initial value. Therefore, NOMAD provides a better local optimal solution than *fmincon* for this relaxed problem using the same starting point. However, $21.30A/mm^2$ for the current density in the rotor winding and $72.49A/mm^2$ for the current density in the stator winding are very high when the exterior volume is so reduced, leading to a low machine efficiency with a high temperature. Considering that, we optimize the machine with different values of current densities J_{cu_r} ($^{A}/_{mm^2}$), and J_{cu_s} ($^{A}/_{mm^2}$) in order to evaluate the effect of current densities on the machine performances. The optimal results obtained by using NOMAD are shown in Table 3.4.

Table 3. 4: Optimal solution of ($\boldsymbol{\mathcal{P}_{R1}}$) problem with fixed current densities

(J_{cu_r}, J_{cu_s})	**Symbol**	**(2,3)**	**(4,6)**	**(8,12)**	**(16,24)**
Average torque (Nm)	T_{em}	5	5	5	5
Torque ripple	ΔT	3.80%	2.18%	4.16%	1.84%
Efficiency	η	94.19%	93.52%	92.10%	87.09%
Copper losses/Output power	$P_{\text{copper}}/P_{out}$	1.51%	3.51%	7.19%	13.70%
Exterior volume ($10^5 mm$)	V_{ext}^c	11.82	5.27	3.17	1.92

It can be seen that with lower current densities, the ratio between the total copper losses and the output power are reduced so that the machine efficiency increases. Moreover, the limitations of the current densities which are $4A/mm^2$ in the rotor winding and $6.5A/mm^2$ in the stator winding were presented in [8] for salient pole WRSM without cooling system to prevent overheating.

Thanks to that, considering that the copper losses can be calculated analytically (see Equation (2.33) in Chapter 2) and that the machine temperature depends on the loss density, a constraint on the copper loss can be used in order to replace the efficiency and temperature constraints by limiting its value to 3% compared to the output power (P_{out}). This makes it possible to obtain a relaxed problem more realistic which takes into account indirectly the efficiency and the temperature of the machine. An improved relaxed optimization problem ($\boldsymbol{\mathcal{P}_{R2}}$) is thus established as follows:

$$(\boldsymbol{\mathcal{P}_{R2}}) = \begin{cases} \min \quad V_{ext}^c \\ x \in \mathcal{B}^{14} \\ Under\ Constraints: \\ T_{em}^{4p} = 5Nm \\ \Delta T^{4p} \leq 5\% \\ P_{copper}/P_{out} \leq 3\% \\ \rho_m r_r^2 \Omega^2 < s \times \sigma \\ geometrical\ constraint \end{cases} \tag{3.17}$$

With the same starting point as above (from the machine provided at Chapter 2), the optimal solution for two different methods is represented in Tables 3.5 and 3.6.

Table 3. 5: Optimal (local) solution of ($\boldsymbol{\mathcal{P}_{R2}}$) problem

Performance	**Symbol**	***fmincon***	**NOMAD**	**Unit**
Average torque	T_{em}	5.00	5.00	Nm
Torque ripple	ΔT	4.28%	4.43%	
Efficiency	η	93.81%	94.12%	
Peak phase voltage	V_{peak}	148.21	338.43	V
Copper losses/Output power	P_{copper}/P_{out}	2.50%	2.99%	
External volume	V_{ext}^c	8.1510	6.2554	$10^5 mm^3$

Table 3. 6: Optimized variables of ($\mathcal{P}_{R2}$) problem

Name	*fmincon*	NOMAD	Unit
Machine length	41.33	34.78	mm
Stator yoke height	10.08	9.87	mm
Tooth height	16.69	15.06	mm
Tooth width	27.07	24.54	mm
Rotor yoke height	8.24	7.60	mm
Pole shoe height	7.74	7.92	mm
Pole shoe width	35.49	38.22	mm
Pole body height	12.61	12.11	mm
Pole body width	25.16	20.08	mm
Pole arc offset	11.42	13.72	mm
Armature current density	3.94	4.63	A/mm^2
Field current density	4.50	4.08	A/mm^2
Stator conductor number	358	366	
Rotor conductor number	144	124	

The external volume of the machine obtained by NOMAD is still better than 23% compared to the one obtained by *fmincon*. With NOMAD, the ratio of the copper losses per the output power reached the limited value (3%) in the constraint so that the external volume can be reduced as much as possible. In addition, the peak value of phase voltage is higher than the solution obtained with *fmincon*; however, this value is still lower than the limited value (800V). The CPU time to obtain those two optimal solutions (about one day) is similar in both cases. In Figures 3.6 and 3.7, the 2D and 3D dimensions of the machines obtained by using *fmincon* and NOMAD are shown.

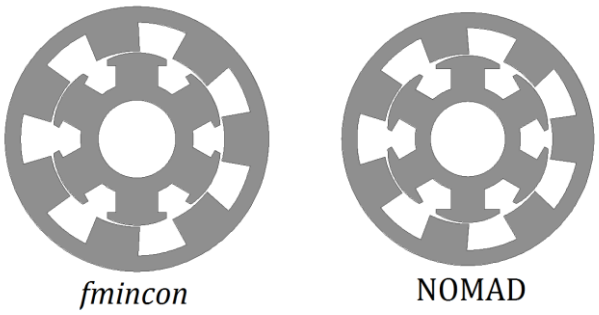

Figure 3. 6: 2D machines with NOMAD and *fmincon* codes

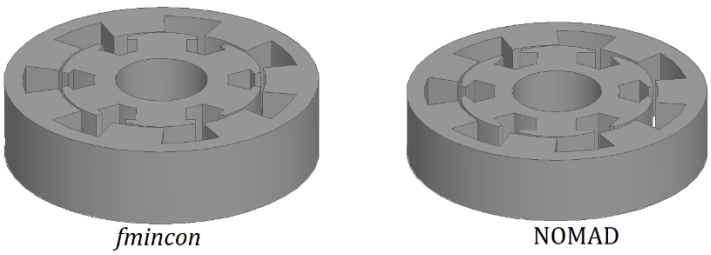

Figure 3. 7: 3D machines with NOMAD and *fmincon* codes

Note that the diameters of both machines are similar; however, the length of the machine obtained by *fmincon* code is higher about 16% compared to the one obtained by NOMAD.

From multiple runs of the optimization methods, it can be concluded that NOMAD is more efficient than *fmincon* to find the best local optimal solutions as possible for those kinds of optimization design problems where some constraints have to be computed via numerical simulations (black-box constraints).

3.3 Optimization of a WRSM Design

Design optimization of electrical machines has been widely investigated during recent decades [89]-[92]. The selected NOMAD solver based on MADS method is used in order to minimize the external volume of heptagonal WRSM subject to all of the constraints which are computed by 2D FE simulations.

Wide intervals are selected for the variables in order to explore a large domain where the optimal design for a given performance is searched. The upper bound of the machine length is limited by 60mm due to the mechanical condition for manufacturing a prototype machine based on a POKI-POKI^{TM} structure. The lower bounds of the stator and rotor yoke heights, the pole body width are selected for avoiding the saturation of the magnetic induction. For the salient pole synchronous machine without a cooling system, the limits of current densities was presented in [70] and are $2 \leq J_{cu_r} \leq 4$; $4 \leq J_{cu_s} \leq 6$ (A/mm^2). The variables with their bounds are shown in Table 3.7.

Table 3. 7: The bounds of optimization variables

Variable	Unit	Bounds B
Machine length	mm	B_1=[20 ; 60]
Stator yoke height	mm	B_2=[05; 20]
Tooth height	mm	B_3=[08; 30]
Tooth width	mm	B_4=[20 ; 50]
Rotor yoke height	mm	B_5=[05 ; 20]
Pole shoe height	mm	B_6=[03 ; 20]
Pole shoe width	mm	B_7=[20 ; 60]
Pole body height	mm	B_8=[10 ; 35]
Pole body width	mm	B_9=[10 ; 30]
Shaft Diameter	mm	B_{10}=[20 ; 90]
Pole arc offset	mm	B_{11}=[0 ; 30]
Armature current density	A/mm^2	B_{12}=[0 ; 6]
Field current density	A/mm^2	B_{13}=[0 ; 4]
Stator conductor number		B_{14}=[0 ; 400]
Rotor conductor number		B_{15}=[0 ; 400]

Effect of parameters on the machine performances

Based on the reference machine designed (see in Chapter 2), all parameters are fixed, the value of each parameter is increased to 20% in order to study its effect on the machine performances as well as on the searching criteria. In Table 3.8, the effects of each parameter on the machine performances including the average value of the torque, the torque ripple, the phase voltage and the efficiency are presented.

Table 3. 8: Effect of the parameters on the machine performances

Parameter	Symbol	ΔT_{em} (%)	$\Delta(\Delta T)$(%)	ΔV_{peak}(%)	$\Delta\eta$(%)
Machine length	L	20	0	19.93	0.17
Stator yoke height	H_{ys}	0.15	1.8	0.19	0.11
Tooth height	H_t	23.58	19.82	10.62	0.12
Tooth width	B_t	-9.61	10.42	-0.54	0
Rotor yoke height	H_{yr}	10.47	12.73	3.59	0.15
Pole shoe height	H_s	4.69	-6.3	2.66	0.03
Pole shoe width	W_s	2.43	79.63	-0.42	0.05
Pole body height	H_b	26.54	121.43	6.12	0.41
Pole body width	W_b	-1.07	2.77	5.87	0.159
Pole arc offset	$Offset$	-2.68	-14.05	-1.87	-0.06
Shaft diameter	D_{sh}	6.46	92.27	19.57	0.24
Air-gap length	e	-8.3	-12.12	-6.69	-0.21
Armature current density	J_{cu_s}	18.28	17.03	7.98	-0.17
Field current density	J_{cu_r}	12.37	31.75	2.11	0.11
Stator conductor number	N_s	0	0	20.46	0
Rotor conductor number	N_r	0	0	0.09	0

Based on the sensibilities of the variable parameters on the machine performances, it can be observed that the conductor number of the windings only have an impact on the value of the phase voltage when other parameters including the current densities are fixed. Therefore, two variables of conductor numbers and the voltage constraint can be eliminated in the optimization program in order to reduce the complexity of the optimization problem and therefore, this can reduce the computational time.

After achieving the solution, the peak value of the phase voltage needs to be verified and if necessary, it can be adjusted by the number of conductors. In this case, 11 other geometrical variables are used to represent the geometrical magnitudes and 2 more variables for the current densities for the windings.

Besides, this machine has a complicate structure (no symmetry, salient pole, 7 phases, etc.) so that the construction of lumped parameter circuit which is used to calculate the machine temperature is very complicate. On the other hand, CFD simulation enables analyzing the temperature distribution of the machine but the associated computational time is really huge and thus, we cannot implement CFD simulations inside our optimization process. Hence, it is necessary to find another constraint which can replace the coil temperature constraint in our optimization. With the experience on thermal analysis, we

assume that with a surface temperature of the machine $\leq 85°C$, we would able to obtain the desired temperature of the coils $\leq 105°C$.

In this case, the temperature can be calculated with a simple equation which can be used for the optimization codes although the results cannot be very precise. At the end of the optimization process, the machine temperature will be verified by CFD analysis in the next chapter.

By considering that the computational time and the complex structure of the WRSM, the surface temperature of the frame is calculated from the following equation:

$$T_s = T_{amb} + \Delta T° = T_{amb} + P_{total} \times R_\theta \tag{3.18}$$

Where: T_s is the surface temperature of the frame, T_{amb} is the ambiance temperature, P_{total} is the total losses and R_θ is the thermal resistance for the convection which is defined as:

$$R_\theta = 1/hS \tag{3.19}$$

Where: h is the convection heat transfer coefficient, S is the surface area of the frame.

The value of the convection heat transfer coefficient for natural convection was presented in [108]. This value is normally in the interval of [10;30] $W/(m^2K)$. In this study, the convection heat transfer coefficient is selected as 20 $W/(m^2K)$.

Considering the limit of manufacturing technique for the prototype machine, several parameters are determined and fixed as follows:

- The smallest length of air-gap is fixed to 0.7 mm,
- The copper slot fill factors are 0.5 for the stator winding and 0.4 for rotor winding.

Therefore, the optimization problem becomes:

$$(\boldsymbol{\mathcal{P}_{R3}}) = \begin{cases} min & V_{ext\_ew}^h \\ x \in B^{13} & \\ Under\ Constraints: & \\ T_{em}^{120p} & = 5Nm \\ \Delta T^{120\mathrm{p}} & \leq 5\% \\ \eta & \geq 94\% \\ T_s & \leq 85°C \\ \rho_m r_r^2 \Omega^2 & < s \times \sigma \\ geometrical\ constraints & \end{cases} \tag{3.20}$$

Using NOMAD function in the Matlab Optimization Toolbox [93], the optimization code calls the FE simulation in ANSYS Maxwell to construct the machine, apply the materials, the currents and then compute the electromagnetic torque and the losses with a selected mesh size. In Tables 3.9 and 3.10, the machine performances and the obtained value of optimized variables are shown.

Table 3. 9: Optimal solution of ($\boldsymbol{\mathcal{P}_{R3}}$) problem

Performance	Value	Unit
Average torque	4.9977	Nm
Torque ripple	3.51%	
Total losses	162.46	W
Efficiency	95.56%	
Surface temperature	85	°C
External volume	$\mathbf{2.0542}$	$10^6\ mm^3$

Table 3. 10: Optimized variables of ($\boldsymbol{\mathcal{P}_{R3}}$) problem

Variable	Value	Unit
Machine length	31.62	mm
Stator yoke height	13.95	mm
Tooth height	18.38	mm
Tooth width	45.46	mm
Rotor yoke height	12.88	mm
Pole shoe height	9.80	mm
Pole shoe width	41.90	mm
Pole body height	22.14	mm
Pole body width	14.50	mm
Shaft diameter	47.53	mm
Pole arc offset	23.18	mm
Armature current density	2.69	$\mathrm{A/mm^2}$
Field current density	3.87	$\mathrm{A/mm^2}$

It should be emphasized that the optimal WRSM presented in Tables 3.9 and 3.10 is the best local optimum that we found so far by using NOMAD during intensive 2D-numerical efforts with several different starting points. Note that these starting points are solutions of the problem ($\boldsymbol{\mathcal{P}_{R2}}$). The CPU time is about 5 days for achieving one local optimum. The minimal value of the external volume is $2.0542 \times 10^6\ mm^3$. This value takes into account the space of the end-winding. Due to the effect of the temperature constraint, the optimal machine shown in Figure 3.8 must be large enough to reduce the surface temperature of the frame.

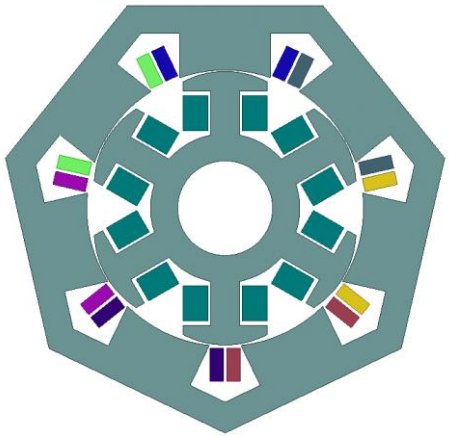

Figure 3. 8: Structure in 2D of the optimal WRSM

3.4 2D Numerical Validation

A transient FE analysis with fine mesh size is more accurate to re-compute the optimal results. In this case, the conductor number of the rotor winding is re-calculated to obtain the desired voltage of the field winding. It should be mentioned that the number of conductors only affects on the voltage (not on the other constraints) thanks to the sensibility study of the parameters on machine performances presented in Section 3.3. Hence, the machine has 133 spires for the rotor winding and 70 spires for the stator winding. The optimal machine is analyzed with fine meshes and in Figure 3.9, the magnetic induction of the stator and the rotor is presented.

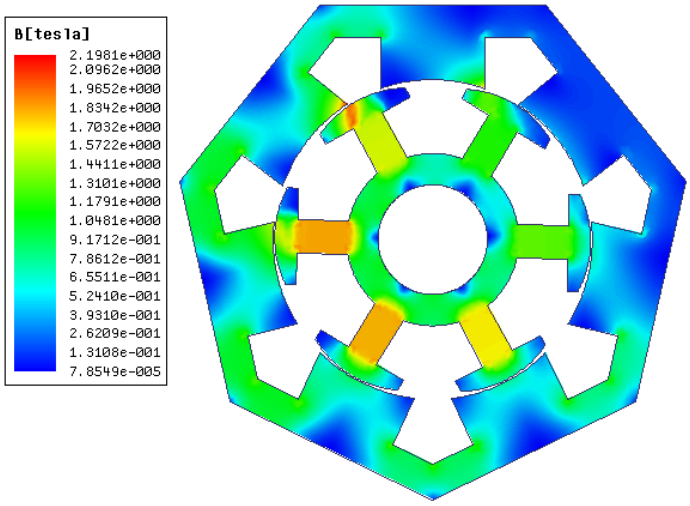

Figure 3. 9: Magnetic induction of the optimal WRSM

It should be noticed that there is a little saturation in the pole shoe and in the tooth tip. The sinusoidal currents shown in Figure 3.10 are used to supply for seven phases of the machine.

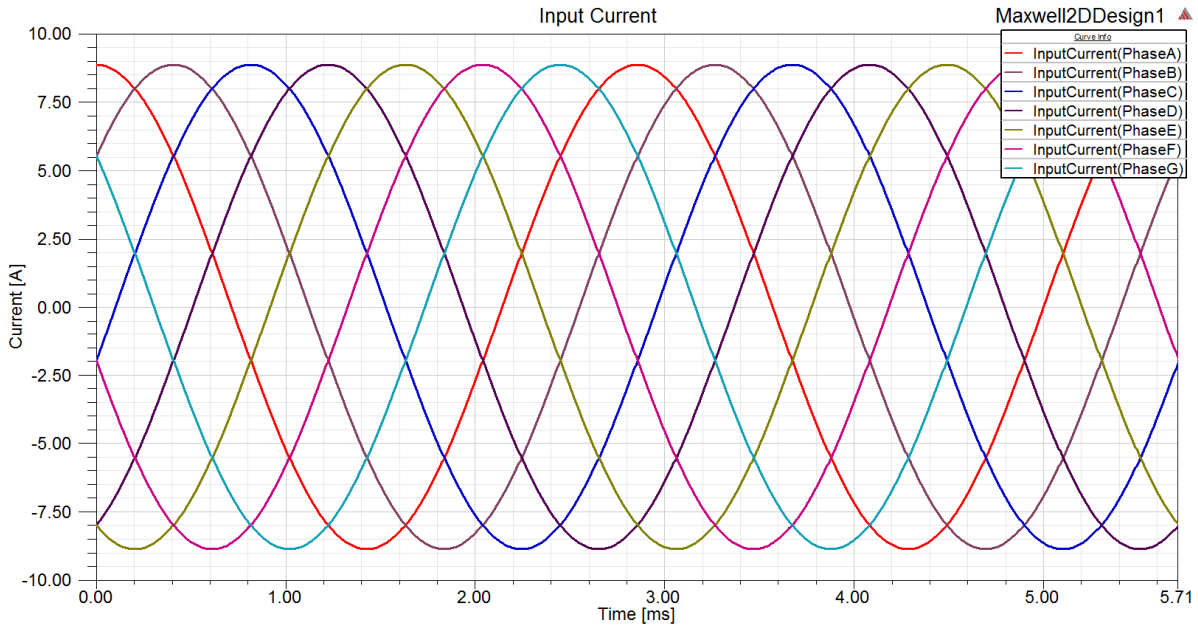

Figure 3. 10: Input currents for different phases of the optimal WRSM

The induced voltages of seven phases shown in Figure 3.11 are not sinusoidal maybe due to MMF harmonic components of the FSCW.

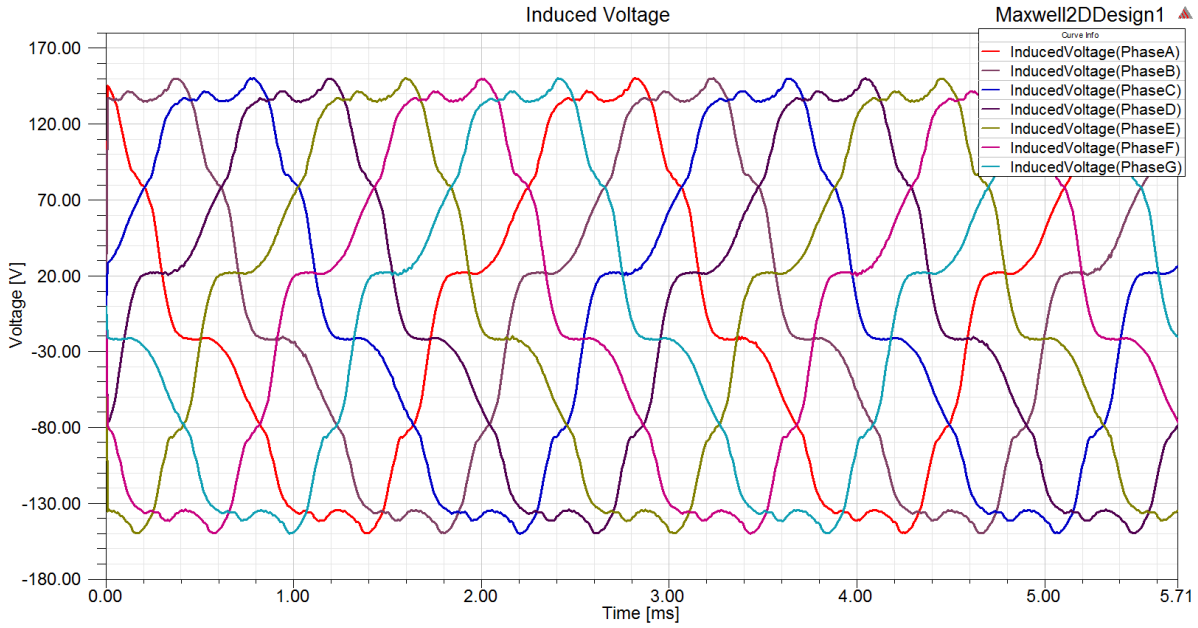

Figure 3. 11: Induced voltages for different phases of the optimal WRSM

In Figure 3.12, the electromagnetic torque of the machine is shown. It can be seen that the average torque is not different when compared to the optimal solution.

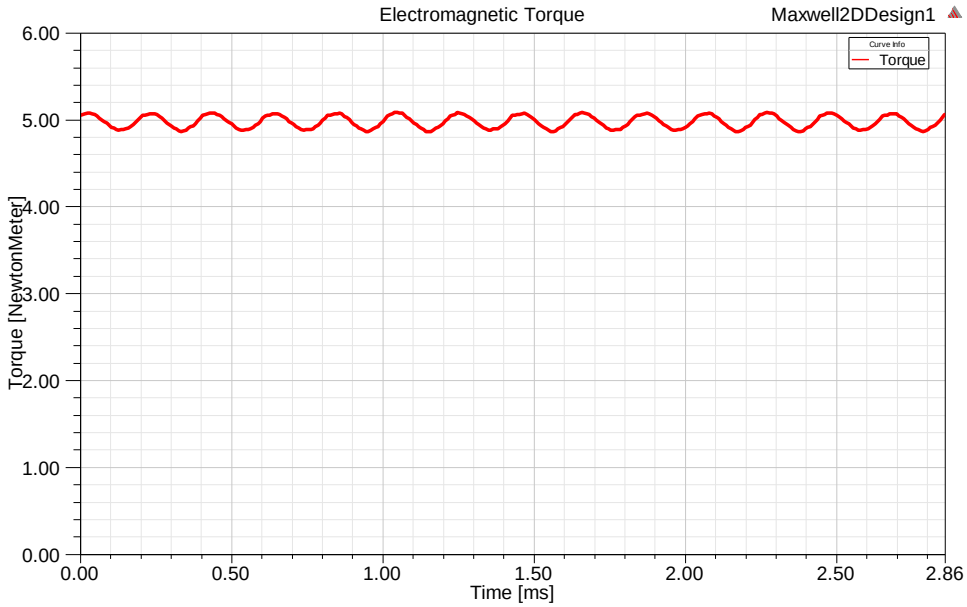

Figure 3. 12: Electromagnetic torque of the optimal WRSM

The machine performances are summarized in Table 3.11. The results show that the torque ripple is higher than the one obtained by the optimization process; however, it is still lower than the limited value.

Moreover, the iron losses are also higher than 162.46W of the optimal machine and therefore, the surface temperature is little bit higher than the desired value (86.5°C in place of 85°C).

Table 3. 11: 2D performances of the optimal WRSM

Performance	Value	Unit
Average torque	4.9978	Nm
Torque ripple	4.09%	
Stator copper loss	35.40	W
Rotor copper loss	50.74	W
Iron losses	80.13	W
Total losses	166.27	W
Efficiency	95.56%	
Peak phase voltage	133.32	V
Temperature	86.5	°C

3.5 "Pancake" Shape Validation of the Optimal Machine

It can be seen that the optimal machine has a form as a "pancake" with a short length and a large diameter. It is thus necessary to do some tests to evaluate the optimal results in order to confirm the pancake shape of the optimal solution. Firstly, different lengths: 50, 100, 150 and 200mm are fixed. Then a new relaxed problem with the copper losses over the mechanical power which has to be lower than 2.5% is considered. This is used in order to reduce the computational time.

The optimization is made with different starting points in order to ensure finding the best possible local optima:

$$(\boldsymbol{\mathcal{P}_{R2r}}) = \begin{cases} \min & V_{ext\_ew}^{h} \\ x \in \mathcal{B}_l^{13} & \\ Under\ Constraints: & \\ & T_{em}^{4p} = 5Nm \\ & \Delta T^{4p} \leq 5\% \\ & P_{copper}/\mathrm{P_{out}} \leq 2.5\% \\ & \rho_m r_r^2 \Omega^2 < s \times \sigma \\ & geometrical\ constraint \end{cases} \tag{3.21}$$

With the fixed values of the machine length, the optimal results are shown in Table 3.12 and Figure 3.13. As can be seen in Figure 3.13, the minimal value of the external volume is reduced when the machine length is reduced for the optimization problem $(\boldsymbol{\mathcal{P}_{R2r}})$ with the constraint of the copper losses over the mechanical power lower than 2.5%.

Table 3. 12: Optimal (local) results of $(\mathcal{P}_{R2r})$ problem

Machine length (mm)	T_{em}^{c} (Nm)	P_{copper}/P_{out} (%)	$V_{ext\_ew}^{h} \times 10^{6} mm^{3}$
200	~ 5	2.44	2.5350
150	~ 5	2.50	2.0013
100	~ 5	2.48	1.4294
50	~ 5	2.52	1.2220
31.62	~ 5	2.49	1.0755

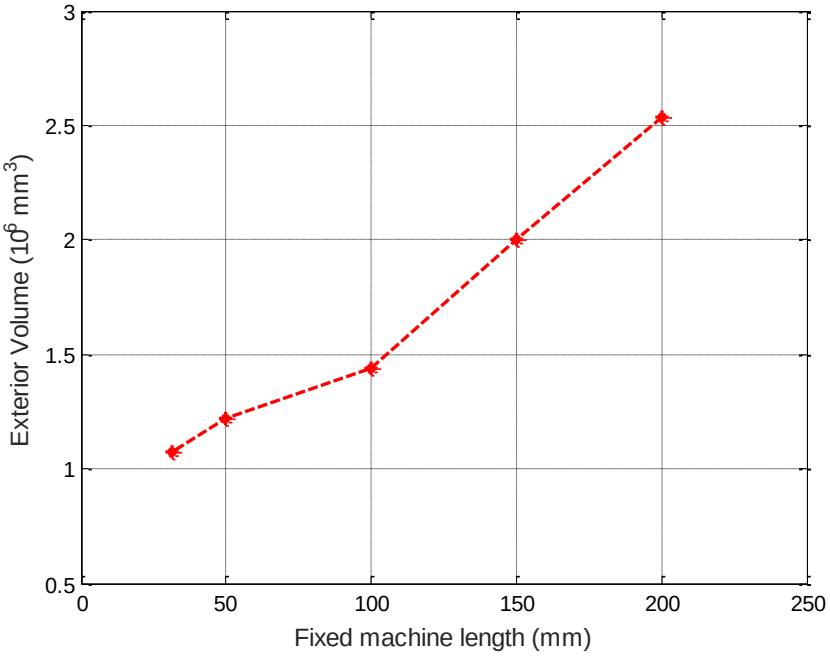

Figure 3. 13: Optimal external volume with fixed machine length

Furthermore, we optimize the machine with the fixed machine length (100mm) using our optimization problem $(\mathcal{P}_{R3})$ defined in Equation (3.20). The starting point is the local optimal result of the optimization problem $(\mathcal{P}_{R2r})$ and thanks to that, the results are obtained and shown in Table 3.13.

Table 3. 13: Optimal solution of $(\mathcal{P}_{R3})$ problem with 100 fixed machine length

Performance	Value	Unit
Average torque	5	Nm
Torque ripple	4.28%	
Copper losses	83.53	W
Iron losses	75.85	W
Efficiency	95.62%	
Peak phase voltage	269.08	V
Temperature	**91.13**	**°C**
External Volume	2.2552	$10^{6}\ mm^{3}$

It should be noted that all of the constraints are satisfied, except the surface temperature. The surface temperature is about 91.13°C which is higher than the desired value. The optimal external volume with the end-winding zone is $2.2552 \times 10^6\ mm^3$, higher 9.78% than the optimal value ($2.0542 \times 10^6\ mm^3$) obtained when the machine length is considered as an optimization variable in the section 3.3. Figure 3.14 shows all of the average values of the torque in the optimization.

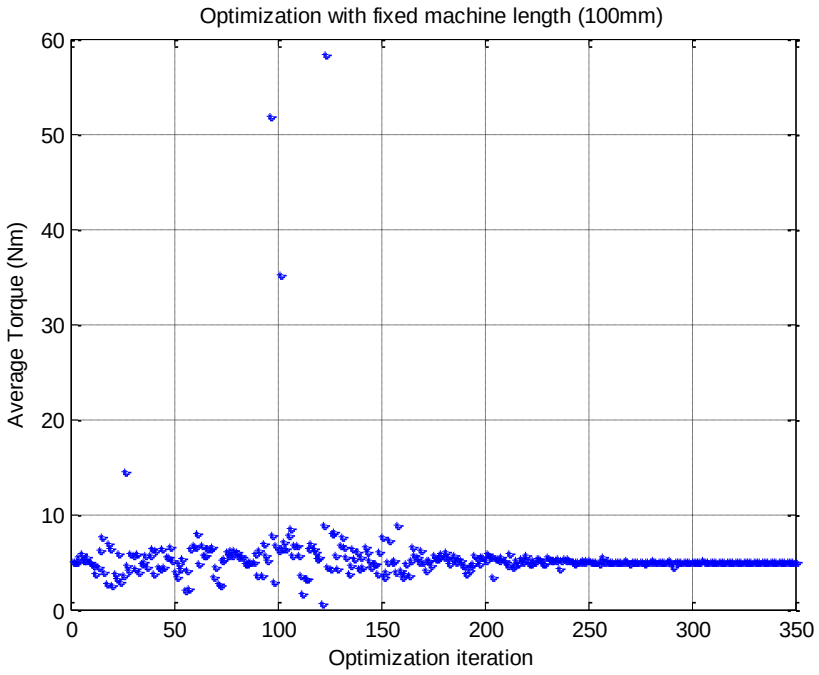

Figure 3. 14: Average torque in Optimization with L = 100mm

The starting point used has the average torque about 5Nm which satisfies the constraint of the average torque in our optimization method; however, the surface temperature and the torque ripple of this starting point are higher than the desired values. The optimization mostly searches the variables which have the average torque between 0Nm to 10Nm. Figure 3.15 shows all of the values of torque ripple obtained by the optimization process.

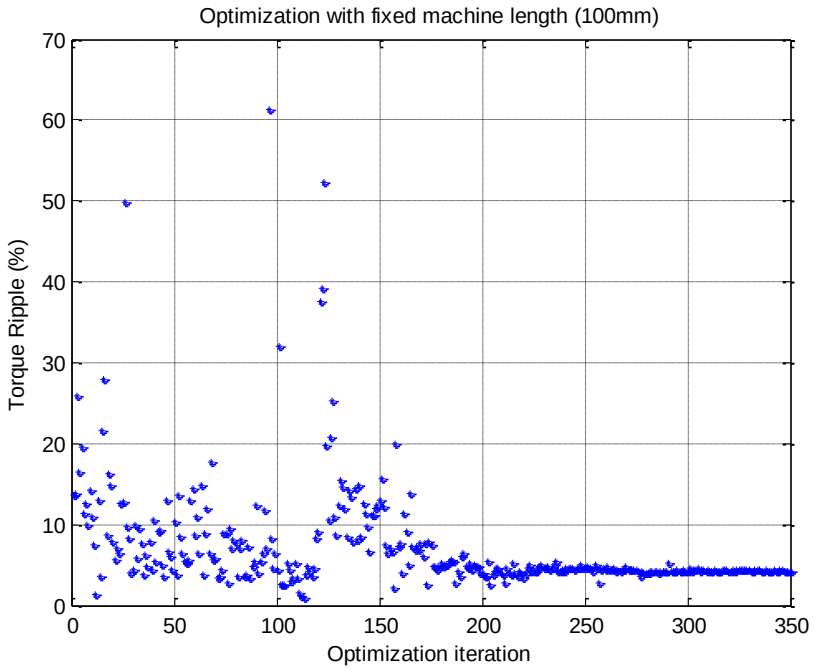

Figure 3. 15: Torque ripple in Optimization with L = 100mm

In the first iterations, the torque ripple of the machine is higher than 5%, even 60% and after 200 iterations, the torque ripple is reduced to nearly 5% after 250 iterations. The values of the surface temperature and the values of objective function obtained by the optimization process are shown in Figures 3.16 and 3.17.

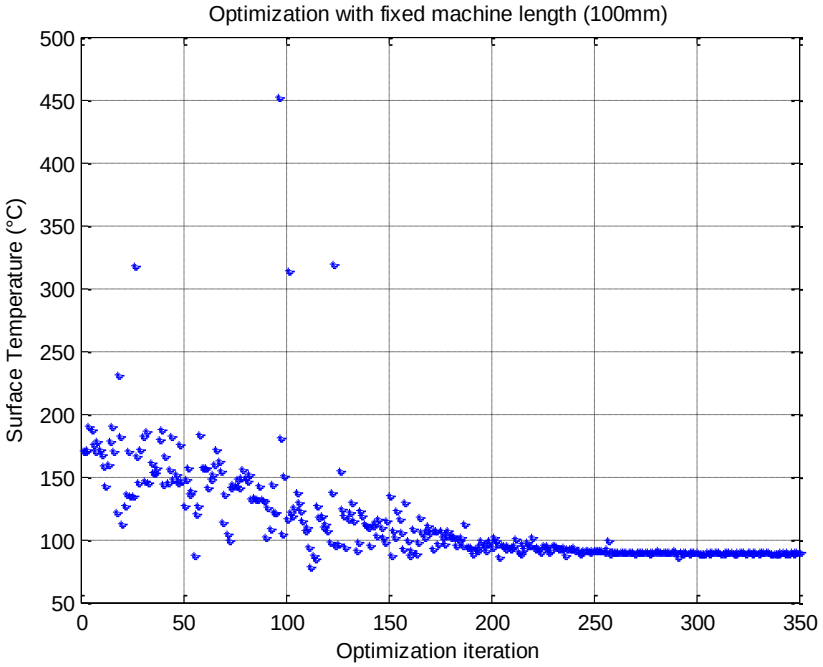

Figure 3. 16: Surface temperature in Optimization with L = 100mm

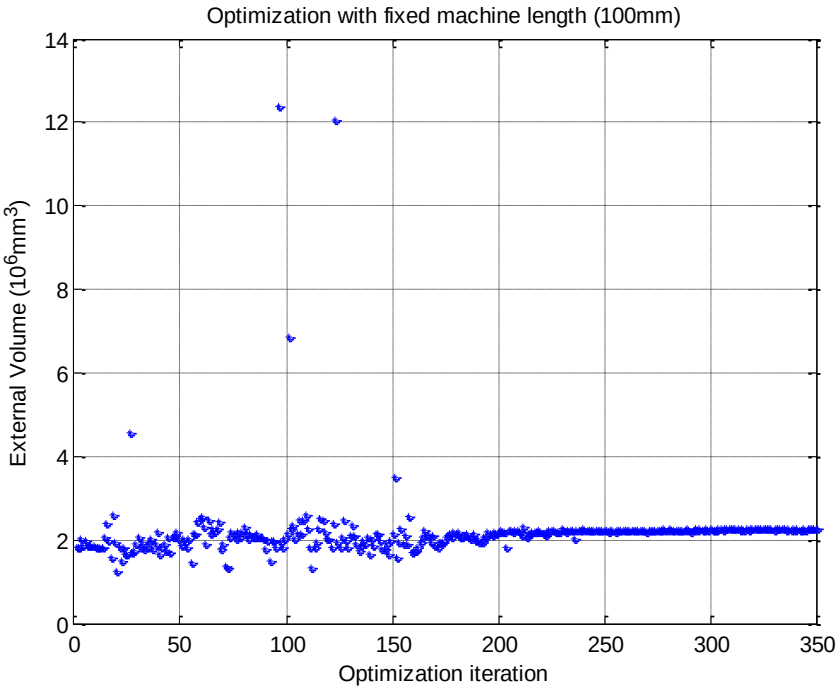

Figure 3. 17: External volume in Optimization with L = 100mm

As can be seen from Figure 3.16, the surface temperature at the starting point is about 170°C, two times higher compared to the desired value: 85°C. The optimization has a tendency to reduce the surface temperature and after 300 iterations, the surface temperature does not vary a lot. After 250 iterations, the optimization converges to a solution which satisfies all of the constraints except the temperature which is a little bit higher than 85°C. As shown in Figure 3.17, the optimal value is higher than the value of the starting point however the torque ripple and the surface temperature are strongly reduced.

All the above figures represent the iterative searches of NOMAD with the machine length of 100mm. Note that the surface temperature is not well satisfied: 91°C in place of 85°C; however, the optimal result so-obtained is better to the starting point.

In order to identify that with smaller machine length, the optimal external volume is smaller or not, we can optimize the machine to solve the same optimization problem with different fixed values of the machine length around 100mm: as 98mm and 102mm. To be more precise, we perform a numerical analysis of the sensitivity of the optimal solution obtained with a length equal to 100mm. In this case, the surface temperature of the machine is limited by 91°C (corresponding to the optimal solution obtained when the length is fixed to 100mm). Especially, the upper and lower bounds of the variables should be arround $\pm$ 20% compared to the optimized variables obtained solving the above optimization problem with the length equals to 100mm. Moreover, in each case the starting point is the optimized solution of the above optimization problem with 100mm fixed machine length. This makes the optimization searches more efficient and makes sure as possible that the optimal solution is the best one in these regions. The optimization problem ($\boldsymbol{\mathcal{P}_{R2r}}$) is defined as:

$$(\boldsymbol{\mathcal{P}_{R3r}}) = \begin{cases} min & V_{ext\_ew}^{h} \\ x \in \mathcal{B}_n^{10} & \\ Under\ Constraints: & \\ T_{em}^{120p} & = 5Nm \\ \Delta T^{120\mathrm{p}} & \leq 5\% \\ \eta & \geq 94\% \\ T_s & \leq 91°C \\ \rho_m v^2 & < s \times \sigma \\ geometrical\ constraints & \end{cases} \tag{3.22}$$

The optimal results and variables with the different fixed values of the machine length are shown in Tables 3.14 and 3.15.

Table 3. 14: Optimal solutions for $(\boldsymbol{\mathcal{P}_{R3r}})$ problem with different fixed machine lengths

Performance	L=100mm	L=98mm	L=102mm	Unit
Average torque	5	5	5	Nm
Torque ripple	4.58%	3.75%	3.48%	
Efficiency	95.60%	95.64%	95.58%	
Temperature	91	91	91	°C
Volume	**2.2032**	**2.1877**	**2.2256**	$\times 10^6 mm^3$

Table 3. 15: Optimized variables for $(\boldsymbol{\mathcal{P}_{R3r}})$ problem with different fixed machine lengths

Name	Value	Value	Value	Unit
Machine length	100	98	102	mm
Stator yoke height	10.15	10.26	10.15	mm
Tooth height	7.23	7.49	7.23	mm
Tooth width	33.03	33.05	33.01	mm
Rotor yoke height	8.26	8.29	8.23	mm
Pole shoe height	7.39	6.79	7.21	mm
Pole shoe width	43.48	44.04	43.42	mm
Pole body height	26.20	26.44	25.99	mm
Pole body width	10.82	10.87	10.95	mm
Pole arc offset	6.77	6.80	8.45	mm
Shaft diameter	20.51	20.70	21.15	mm
Armature current density	2.92	2.92	2.92	A/mm^2
Field current density	3.96	3.96	3.96	A/mm^2

The CPU time to obtain good optimal results is really important: about 7 days. For these three cases, the average torque is 5Nm, the torque ripple is lower than 5% and the temperature is equal to the limited value (91°C). It should be noticed that the solutions satisfy all of the constraints. The minimal value of the external volume is obtained when the machine length is fixed to **98mm (less than** the optimal solution obtaine with 100mm machine length). On the contrary, the minimal value of the external volume with 102mm machine length is higher compared to the one with 100mm machine length. This sensitivity study around a length fixed to 100mm shows clearly that it is possible to reduce the external

volume by decreasing the length of the machine (the contraray is not possible). This involves that if the length becomes a free optimization variable, NOMAD will converge naturally to solution with smaller lengths. In conclusion (considering our way to determine the best as possible local solution), the optimal machine has a "pancake" shape.

3.6 Chapter conclusion

The CPU time for solving our optimization problem is extremely high so that several relaxations coupled with FE analysis are proposed and used in order to compare the efficiency and the reliability of *fmincon* solver (a Quasi-Newton based algorithm) and NOMAD solver (a MADS based algorithm). The results show that NOMAD is more efficient than *fmincon* for our numerical optimization design problem. Due to the difficulty for calculating the coil temperature, the surface temperature based on the total losses are used to replace the constraint of the coil temperature. Starting from the previous local solutions, a new more precise design problem is solved using NOMAD and therefore, the best local solution we obtained so far is selected as our final design solution. This solution is then verified by using 2D FE simulations with fine meshes. Finally, the optimal machine is validated in order to confirm that the optimal machine shape is a "pancake" one. In Chapter 4, this optimal solution will be validated by 3D electromagnetic and thermal simulations. Moreover, a prototype is built and experimental tests are provided.

Chapter 4

3D Validation, Manufacturing and Experimental Tests

This chapter describes 3D electromagnetic/thermal numerical simulations and experimental tests on our prototype machine for validating the optimized heptagonal WRSM provided in Chapter 3. In the optimization process, for reducing the computational time, a 2D finite element tool was used to compute the electromagnetic performances of the machine and an analytical equation involving the total losses was used in order to calculate the surface temperature of the machine. Therefore, the optimal results need be validated by more precise numerical methods by using a 3D FE method and also a Computational Dynamics Fluid (CFD) method. Finally, a prototype machine is built and some experimental tests are conducted. The results of these tests are devoted to the comparison of measured and predicted numerical results.

4.1 3D Electromagnetic Validation of the Optimal Solution

The 3D model using FE method allows us to analyze the flux in the end-zone of electrical machines. The current in the end-winding can generate leakage flux which is not included in the flux calculated from the design in 2D, making the solution more accurate. However, these simulations are more expensive in terms of time and memory, because it needs a large number of mesh elements due to the complicated 3D structure of the WRSM. At least 60 hours is necessary in order to obtain precise results. The optimal variables in Chapter 3 are implemented in the 3D model and then the 3D structure of the machine is constructed and shown in Figure 4.1.

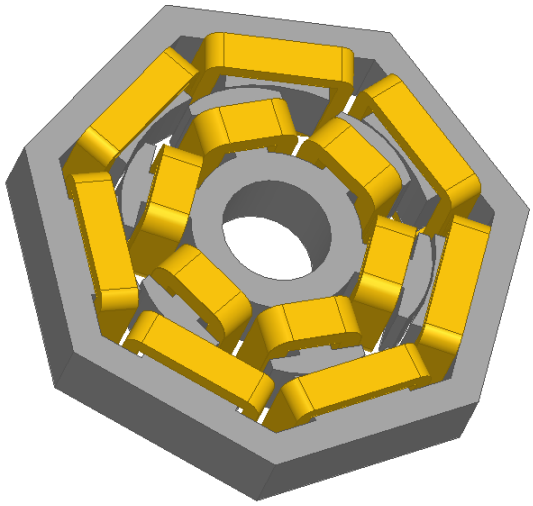

Figure 4. 1: 3D structure of the optimal heptagonal based WRSM

In Table 4.1, the machine performances in 3D with small mesh size using ANSYS Maxwell 16.0 are shown. The average value of the torque is 4.8434Nm and the torque ripple is about 4.28%. Note that the average torque in 3D is lower than the one in 2D. This can be due to the version of ANSYS Maxwell software used. In addition, the iron losses in 3D are higher than the value in 2D because of the leakage flux induced by the current in the end-winding. Therefore, the electromagnetic efficiency is reduced to 94.79% and the surface temperature of the machine is increased to 95.75°C.

Table 4. 1: 3D performances of the optimal WRSM

Performance	Value	Unit
Average torque	4.8434	Nm
Torque ripple	4.28%	
Phase voltage (rms)	91.74	V
Stator copper loss	35.40	W
Rotor copper loss	50.74	W
Iron losses	105.14	W
Total losses	191.28	W
Efficiency	94.79%	
Temperature	95.75	°C

It can be seen that the average torque is smaller than 5Nm. The average torque needs to be increased in order to obtain the desired performance. The machine length is selected to increase the average torque without affecting too much the surface temperature based on the sensibility analysis of the parameters. Thanks to an analytical approximation, the new value of the machine length calculated is 32.65mm in order to obtain 5Nm for the average torque. In order to verify the results, a new 3D simulation based on FE method is run. The new electromagnetic torque is shown in Figure 4.2 and the performances of the new machine are shown in Table 4.2.

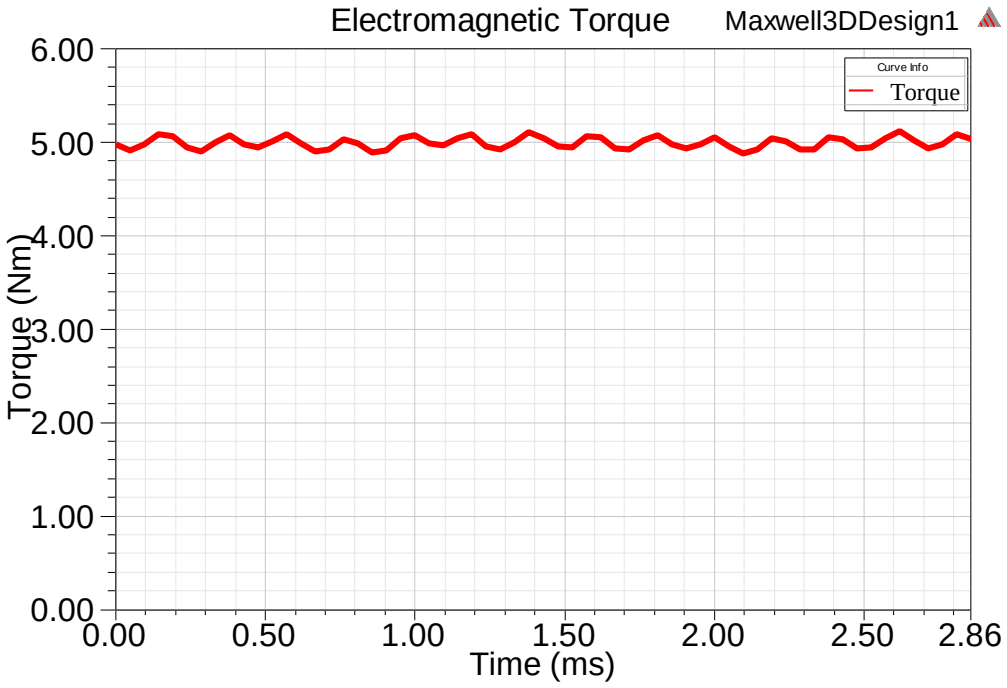

Figure 4. 2: 3D electromagnetic torque of the rectified WRSM

Table 4. 2: 3D machine performances of the corrected WRSM

Performance	Value	Unit
Average torque	5	Nm
Torque ripple	4.05%	
Phase voltage (rms)	94.27	V
Stator copper loss	35.80	W
Rotor copper loss	51.51	W
Iron losses	105.94	W
Total losses	193.25	W
Efficiency	94.89%	
Temperature	96.07	°C

The iron losses in 3D are higher than the ones in 2D, leading to a lower efficiency. The surface temperature obtained is thus higher about 11°C than the desired value (85°C).

Test with ANSYS Maxwell's another version (15.1)

It should be noticed that the average values of the torque analyzed by 2D and 3D FE simulations are different about 3%. This difference can be explained by ANSYS Maxwell version which is run by a Matlab script. To demonstrate that, other version of ANSYS Maxwell (Maxwell 15.1) is used with the same parameters and same Matlab script for analyzing the machine performance.

With the optimal results, the average torque is obtained in 2D FE simulation by ANSYS Maxwell 16.0 (not version 15.1) is about 5Nm. However, with ANSYS Maxwell 15.1, the average torque shown in Figure 4.3 is about 4.8192 Nm.

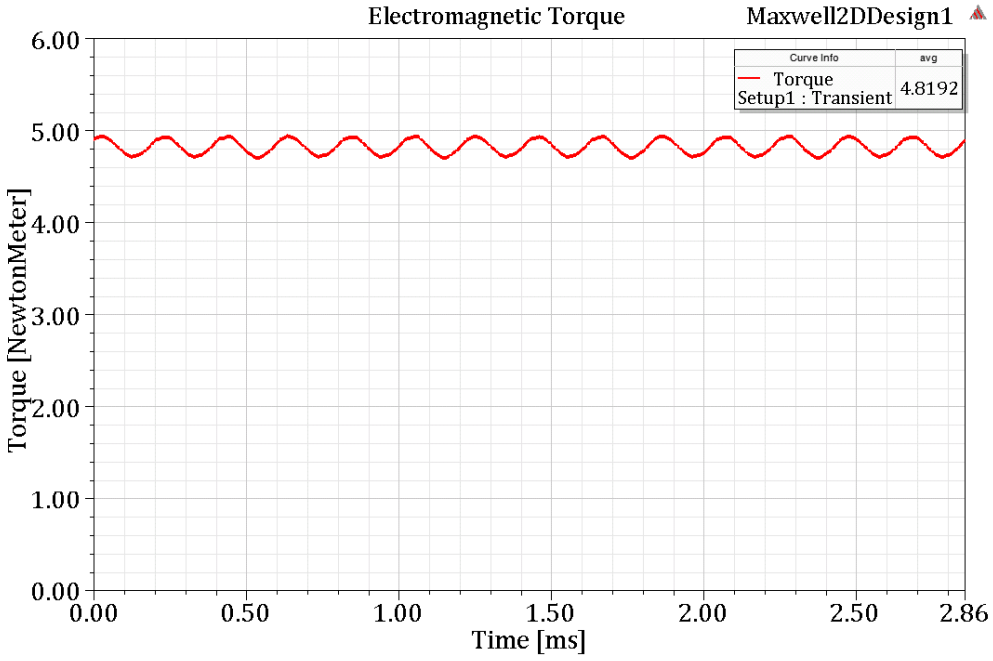

Figure 4. 3: Electromagnetic torque obtained by 2D ANSYS Maxwell 15.1

With the new value of the rectified machine length (32.65mm), the average torque analyzed by 2D ANSYS Maxwell 15.1 is shown in Figure 4.4. In this case, the average torque is about 4.9738Nm (nearly 5Nm).

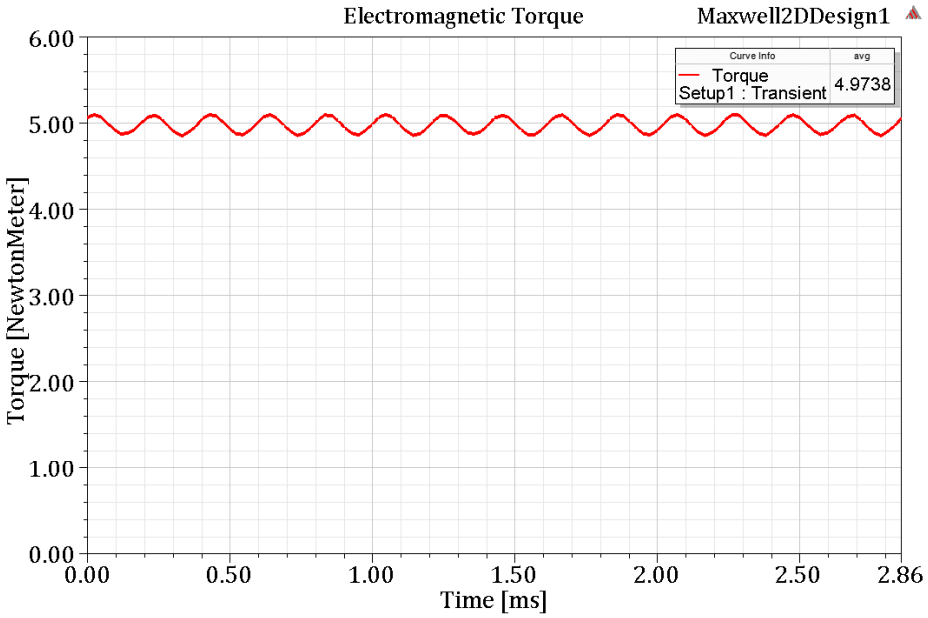

Figure 4. 4: Electromagnetic torque obtained by 2D ANSYS Maxwell 15.1

For 3D FE simulation, with optimal solution, the average torque shown in Figure 4.5 is about 4.8435Nm and with the rectified machine length (32.65mm), the average torque shown in Figure 4.6 is about 4.9915 Nm. It should be noticed that the average torques obtained by 2D and 3D simulations by ANSYS Maxwell 15.1 are similar.

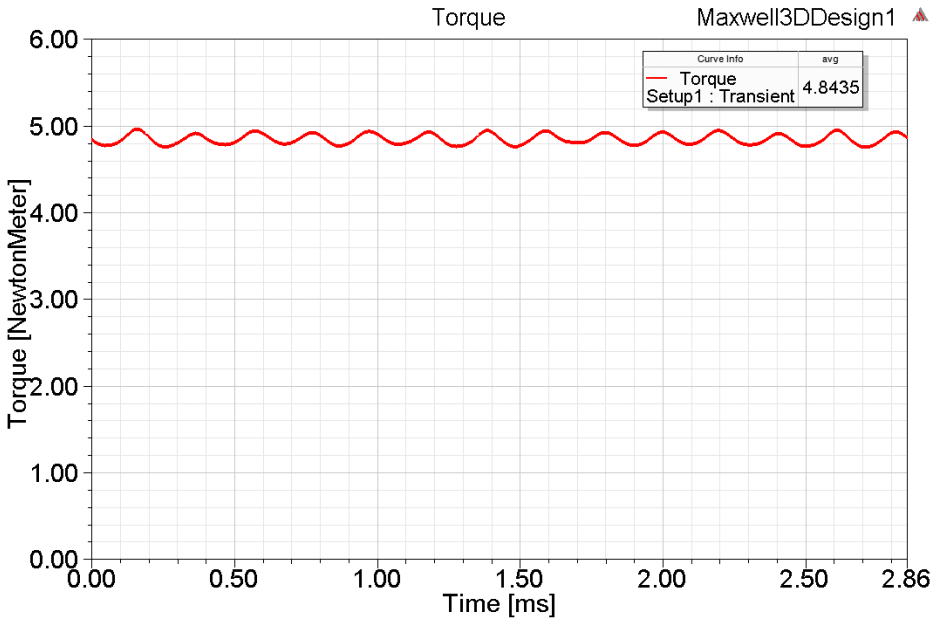

Figure 4. 5: Electromagnetic torque analyzed by 3D ANSYS Maxwell 15.1

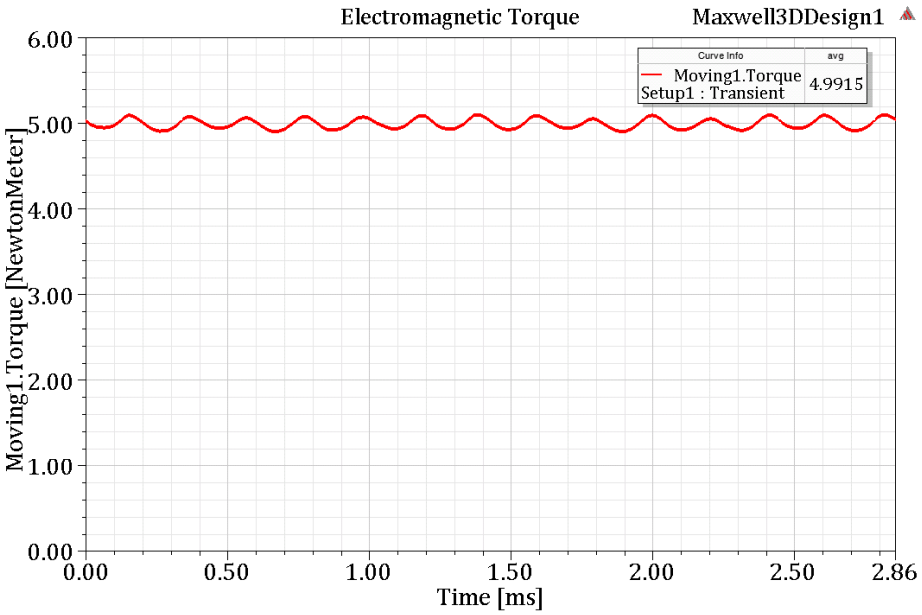

Figure 4. 6: Electromagnetic torque analyzed by 3D ANSYS Maxwell 15.1

In conclusion, it exists some differences between the 2D average values of the torque computed using different ANSYS Maxwell versions. This can be explained by the enhancements in the mesh generation process, which result in slightly different mesh in different versions or the different values of nonlinear residual as well as the different treatment of $B(H)$ curve (with or without interpolation). Generally, the average torque in 2D and 3D model is not different so much although 3D model takes into account the end-zone winding. Note that the 3D average values of the torque obtained with both ANSYS Maxwell licenses are similar (about 5Nm with 32.65mm machine length).

4.2 3D Thermal Validation of the Optimal Solution

The integration of power converters into the machine housing can raise the temperature of the machine. High temperature may cause problems such as the failure of insulation materials and this may decrease the lifetime of the converters and of the machine. Hence, it is necessary to determine the temperature distribution on the machine at the design state. Thermal models are analyzed according to two approaches: lumped parameter thermal models or numerical methods.

The lumped parameter thermal models are used to estimate key temperatures inside electrical machines much more rapidly than numerical methods. However, the calculation of lumped parameters mainly based on dimensional data of the machine can be challenging for complex parts including the active part of the winding and the end-winding body [94].

On the contrary, using numerical simulations can precisely predict the temperature of complex structures but the computational effort for modelling is important. The simulations can be carried out by FE or CFD methods. FE thermal simulation enables the accurate computation of the temperature inside solid bodies. In order to take into account the effect of fluid on solid, convection heat transfer coefficients

need to be applied at the boundaries between the solid zone and the moving fluid. These coefficients can be provided using analytical approaches or experimental tests. Using CFD simulations, solid and fluid regions can be modeled and they can precisely predict the temperature of complex structures including fluid and solid bodies. In fact, the exact evaluation of the temperature at different locations inside the machine is a very demanding task because of the complicity of the fluid velocity and of the surface properties of the machine [94], [95].

4.2.1 Heat Transfer

The heat is removed by convection, conduction and radiation [95], [96]. Convection occurs between a surface and a fluid when there is a temperature gradient. Conduction occurs when heat is transferred from one element to another due to different temperatures between the two elements. Radiation is the heat dissipation to the environment through electromagnetic waves. The proportion of heat transfer by radiation is usually moderate, not important in electrical machine with cooling system. In a machine without cooling system, the effect of the radiation can be only considered on the outer surfaces.

Conduction heat transfer

There is an energy transfer from the high-temperature region to the low-temperature region which occurs normally in solids due to the energy transfer between free electrons and molecular vibrations of the molecules in matter. The energy is transferred by conduction and the heat transfer rate per unit area is proportional to the normal temperature gradient as:

$$q = \lambda A \frac{dT}{dx} \tag{4.1}$$

Where: A is the exchange area, λ is the conduction coefficient, and T is the temperature.

Convection heat transfer

The convection terms refer to the transport of quantities of the interest (mass, momentum and energy) due to the physical motion of the fluid. Thus, convection heat transfer depends on the viscosity of the fluid and on the thermal properties of the fluid (thermal conductivity, specific heat density). The temperature gradient is dependent on the rate at which the fluid carries the heat away. In fact, a high velocity produces a large temperature gradient, and so on. The overall effect of the convection is defined as:

$$q = hA(T_s - T_a) \tag{4.2}$$

Where: A is the surface area, h is the convective heat transfer coefficient.

There are two mechanisms of convection:

- Natural convection is caused by density difference due to temperature differences between different regions of the fluid.

- Forced convection occurs when the fluid is forced to flow over the surface by external forces such as fans and cooling systems.

Radiation heat transfer

Electromagnetic radiation that is propagated as a result of a temperature difference; this is called thermal radiation. A simple radiation problem is encountered when we have a heat transfer surface at temperature T_s completely enclosed by a much larger surface maintained at T_a. The rate of the radiation heat exchange in this case can be calculated [112] as:

$$q = \epsilon\sigma A(T_s^4 - T_a^4) \tag{4.3}$$

Where: ϵ is the emission coefficient, σ is the Boltzmann constant ($5.67 \times 10^{-8}\, Wm^{-2}K^{-4}$), A is the surface area.

4.2.2 Computational Fluid Dynamics

In this study, CFD is used to analyze the temperature distribution of the WRSM due to its complex unsymmetrical salient pole structure.

Concept of CFD

The thermal analysis is necessary to identify the temperature distribution of the different machine parts. Navier-Stokes equations are used to describe the physical properties of the fluid and it is the governing equation of CFD. The CFD method is widely used in the thermal analysis of electrical machines because of its capability of accurate calculation of thermal field. Basically, CFD is a numerical approach for solving nonlinear differential equations by describing fluid dynamic problems and therefore, it is the most extensive modelling approach for the thermal analysis of electrical machines. The techniques such as finite element method, finite volume method, polynomial fitting, finite difference method, spectral method, boundary element method. can be used in CFD.

Navier-Stokes equations

The governing equations of fluid dynamics which are called the Navier-Stokes equations are the conservation laws of mass, momentum and energy [97], [98]:

- Mass is conserved for the fluid.
- The rate of change of momentum equals the sum of forces acting on the fluid.
- The rate of change of energy equals the sum of rate of heat addition to the rate of work done on the fluid.

Continuity equation

Considering the model of a moving fluid element, the mass of this element δm is fixed, and is calculated as:

$$\delta m = \rho\delta\mathcal{V} \tag{4.4}$$

Where: $\delta\mathcal{V}$ is the volume of this element, ρ is the fluid density.

Since the mass is conserved, it can be seen that the time rate of change of the mass of the fluid element is zero as the element moves along with the flow:

$$\frac{\partial(\delta m)}{\partial t} = 0 \tag{4.5}$$

From equations (4.4) and (4.5), we obtain:

$$\frac{\partial \rho}{\partial t} + \rho \nabla . \vec{U} = 0 \tag{4.6}$$

Where: $\vec{U}$ is the fluid velocity vector.

Momentum equation

Based on Newton's second law, the net force on the fluid element equals its mass times the acceleration of the element as:

$$\vec{F} = m\vec{a} \tag{4.7}$$

There are two sources of this force:

- Body forces: which act directly on the volumetric mass of the fluid element such as gravitational, electric and magnetic forces.
- Surface forces: which act directly on the surface of the fluid element due to:
  - The pressure distribution acting on the surface of the fluid,
  - The shear and normal stress distributions acting on the surface, also imposed by the outside fluid "tugging' or 'pushing' on the surface by means of friction. The shear and normal stresses in a fluid are related to the time rate of change of the deformation of the fluid element.

In different forms, the momentum equation can be represented as:

$$\frac{\partial(\rho u)}{\partial t} + \nabla . \left(\rho u \vec{U}\right) = -\frac{\partial P}{\partial x} + \frac{\partial \tau_{xx}}{\partial x} + \frac{\partial \tau_{yx}}{\partial y} + \frac{\partial \tau_{zx}}{\partial z} + \rho f_x \tag{4.8}$$

$$\frac{\partial(\rho v)}{\partial t} + \nabla . \left(\rho v \vec{U}\right) = -\frac{\partial P}{\partial y} + \frac{\partial \tau_{xy}}{\partial x} + \frac{\partial \tau_{yy}}{\partial y} + \frac{\partial \tau_{zy}}{\partial z} + \rho f_y \tag{4.9}$$

$$\frac{\partial(\rho w)}{\partial t} + \nabla . \left(\rho w \vec{U}\right) = -\frac{\partial P}{\partial z} + \frac{\partial \tau_{xz}}{\partial x} + \frac{\partial \tau_{yz}}{\partial y} + \frac{\partial \tau_{zz}}{\partial z} + \rho f_z \tag{4.10}$$

Where: ρ is the fluid density, u, v and w are the x , y and z components of the fluid velocity vector $\vec{V}$, P is the static pressure; f_x, f_y, f_z are the body force per unit mass on the fluid element acting in the x, y, z direction, τ_{ij} is the shear stress, τ_{ii} is the normal stress.

Energy equation

The energy equation describes the energy conservation. The total rate of changes of the energy inside the fluid element is equal to the net flux of heat into the element plus the rate of working done on the element due to body and surface forces as:

$$\frac{\partial(\rho T)}{\partial t} + \nabla.\left(\rho T \vec{U}\right) = \nabla.\left(\frac{\lambda}{c}\nabla T\right) + S_T \tag{4.11}$$

Where: T is the temperature, c is the specific heat capacity, λ is the thermal conductivity, S_T is the volume heat source.

It is difficult to solve the partial differential equations directly. Thus, it is thus necessary to transfer them into discretized forms. In ANSYS Fluent which is the software used in our study, the discretization method is based on finite volume method.

Finite volume method

Finite Volume Method (FVM) is based on the integral form of the governing equations. The method starts by dividing the flow domain into a finite number of contiguous control volumes. The conservation equations are applied to each control volume. The variables are stored at the centroid of each control volume. Extra boundary nodes are added and the transport equations are then integrated over each control volume. If the Navier-Stokes equations are satisfied in each control volume, they will be satisfied for the whole domain [108], [112].

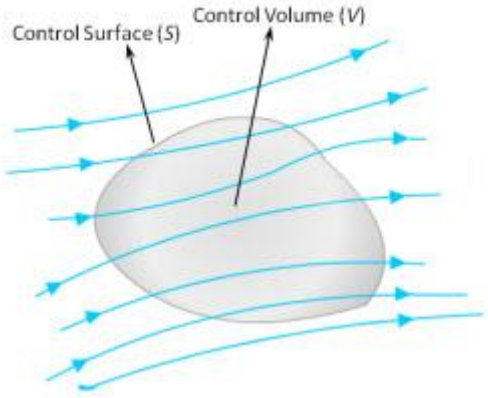

Figure 4. 7: A closed volume within a finite region of flow [113]

A general flow field is shown in Figure 4.7 with a closed volume drawn within a finite region of the flow. This volume defines a control volume and a control surface is defined as the closed surface which bounds the volume. The fundamental physical principles are applied to the fluid inside the control volume, and to the fluid crossing the control surface in an integral approach. These integral forms of the governing equations can be manipulated to obtain partial differential equations.

When the flow passes through it, the rate of the increase of the quantity which can be either mass or momentum component inside the volume is calculated with:

$$\frac{\partial}{\partial t}\int_V UdV = -\oint_S \vec{F}d\vec{S} + \int_V Q_f dV \quad (4.12)$$

Rate of Increase of Quantity inside Control Volume

Flux of Quantity in – Flux of Quantity out

Source

Where: V is the control volume, S is the control surface, U is the quantity, F is the flux, and Q_f is the source.

Control volume is split into small cells by ANSYS Meshing shown in Figure 4.8. In CFD, numerical integrations of these equations are solved on small cell volumes of arbitrary shapes.

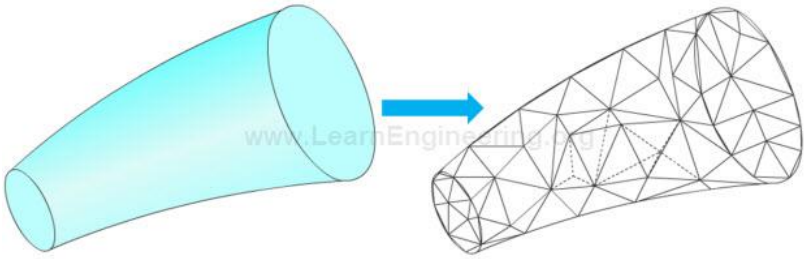

Figure 4. 8: Conversion of control volume in to small non-overlapping cells: Meshing [15]

There are three types of grids: structured grids, unstructured grids and block structured grids. The simplest one is the structured grid as shown in Figure 4.9. Using this type of grids, all nodes have the same number of elements around it. It is easily to describe and store them and it is only used for simple structures.

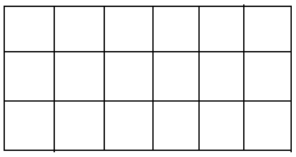

Figure 4. 9: Structured grid

For a complex structure, unstructured grid shown in Figure 4.10 is usually used. It is often used in CFD but the data structure is irregular, it is more difficult to describe and store them.

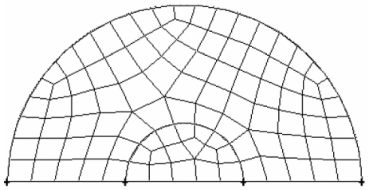

Figure 4. 10: Unstructured grid [15]

Block structure grid includes structured and unstructured grid. The domain is divided into several blocks, and then we use different structured grids in different blocks.

Turbulence flow

The Reynolds number is defined as

$$Re = \frac{UL}{\nu} = \frac{Inertial\ forces}{Viscous\ forces} \tag{4.13}$$

Where: U is the characteristic velocity, L is the characteristic length, and ν is the kinematic viscosity.

Fluids with the same Reynolds number behave the same way. Based on the Reynolds number, it is possible to distinguish the different types of fluid such as laminar ($Re \leq 2000$), transitional ($2000 \leq Re \leq 4000$), and turbulent ($Re \geq 4000$).

Turbulent flows occur at high Reynolds number because inertia forces are sufficiently large to cause eddies in the flow. There are three common ways to model turbulent phenomena of fluid [109] as:

- Direct Numerical Simulation (DNS)
  - Solving the full unsteady Navier-Stokes equations,
  - Modelling smallest eddies living for a short period of time,
  - Extremely fine and fully 3D mesh so the cost is too prohibitive,
  - Not practical for industrial flows.

- Large Eddies Simulation (LES)
  - Resolving only largest eddies in the flow,
  - Solving the filtered Navier-Stokes equations,
  - Less computational cost than DNS, but the computational resources needed are still too large for most practical applications.

- Reynolds-Average Navier-Stokes (RANS) models
  - Solving time-average Navier-Stokes equations,
  - The least computationally expensive method,
  - A popular method for industrial flows.

The family of RANS models is widely used in the field of turbulence for a large number of industrial applications. In particular, RANS is the most widely method for thermal analysis of electrical machines. Based on turbulent kinetic energy and dissipation rate or length scale transport equations, RANS models are commonly used for developing turbulence arising from buoyancy, shear, or shocks [103].

In fact, the Navier-Stokes equation contains five equations (1 continuity, 3 momentums, 1 energy) in terms of six unknown flow field variables ρ, u, v, w, e, P. All of these variables are decomposed into time-average and fluctuating components. The instantaneous fluctuating components are rejected to obtain the RANS equation. For incompressible fluid, the density does not change with pressure. The RANS equations can be described for fluid flow of an incompressible fluid [99] as:

$$\rho\frac{\partial U}{\partial t} + \rho(U.\nabla)U = -\nabla P + \mu\nabla^2 U + f \quad (4.14)$$

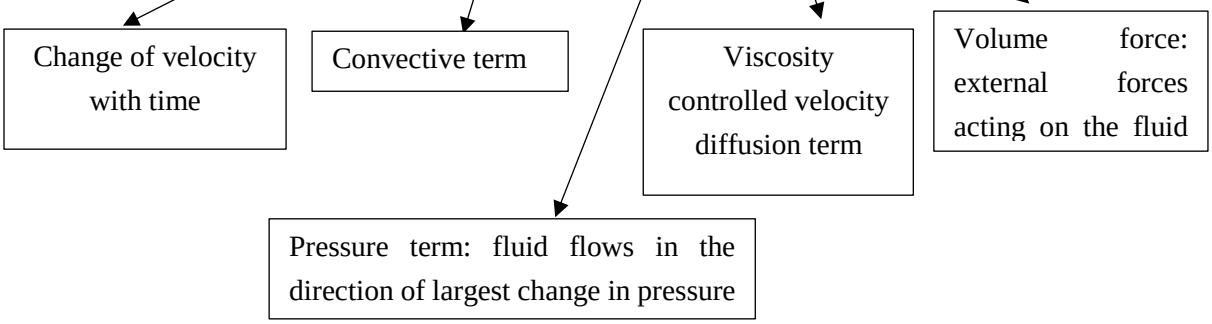

$$\nabla U = 0 \quad (4.15)$$

Where: ρ is the density, U is average velocity field, P is the pressure, μ is the dynamic viscosity, f is the volumetric force.

4.2.3 Thermal Analysis

One of most widely used CFD solvers is ANSYS Fluent which is integrated into the simulation environment ANSYS Workbench. Workbench offers several features as facilitating simulation setup and it minimizes the number of cases required to run. The principle steps in a CFD simulation for investigating the temperature distribution are shown in Figure 4.11.

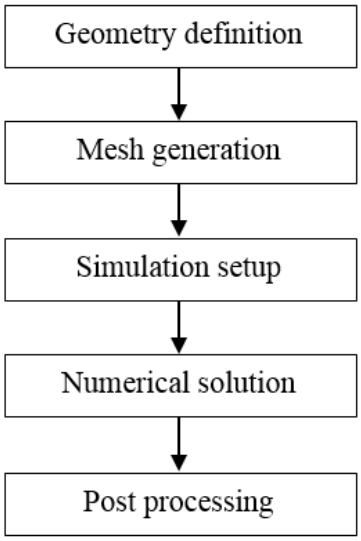

Figure 4. 11: Principal steps of CFD modelling

Geometry definition is often easily accomplished with CAD/ANSYS Maxwell. In our study, mesh is generated by using ANSYS Meshing with many mesh shapes such as hexahedral, tetrahedral, prism and polyhedral elements. After meshing, the pre-processor is used to setup the simulation domain, the

boundary conditions and the solver controls. The solver runs until the convergence conditions are met or if the number of iterations exceeds a specified maximum value. The results are then processed in a post-processing program. Indeed, the accuracy of the results is dependent on the turbulence models, on the boundary conditions, on the mesh operations (near wall treatments), on the discretization schemes and on the convergence criteria.

Geometry

A simplified model of all the components in the machine is created in 3D by ANSYS Maxwell. The 360° model is required because of the lack of symmetry in the geometry of the machine. The thermal modelling of some parts such as the winding, the bearing is a challenging task so that the bearing is not modelled in this study. In order to simplify the CFD model, several assumptions are made, see [97] for details on the assumptions as follows:

- The ambient temperature is constant,
- There is no influence of the temperature rise on the thermal property of the materials,
- The lamination is modeled as orthotropic composite material which has different thermal conductivities in different directions,
- Air is blown in and out perpendicular to the inlet and outlet faces,
- Heat sources are uniformly distributed in the corresponding parts of the machine.

In fact, the insulation is used to isolate the winding electrically; however, it reduces the evacuation of the copper losses in the winding because it has a very low thermal conductivity when compared to the thermal conductivity of the copper. Therefore, the temperature of the winding without insulation is smaller than the one taking into account the insulation. In order to obtain precise results, it is necessary to model the insulation in the thermal analysis.

The winding can be simplified as homogeneous winding thanks to the calculation of equivalent conductivity. The winding has several different insulations such as wire insulation, slot insulation, wedges and they are modelled as an equivalent insulation system [104]. In our study, the winding insulation is simplified and it consists only of the wire insulation as it is shown in Figure 4.12.

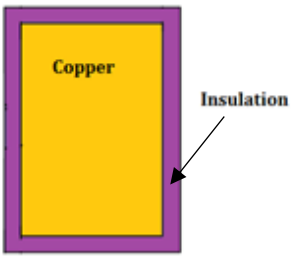

Figure 4. 12: Winding components

The stator and the rotor are split up into many laminations to reduce eddy current losses. The laminations are separated by insulations with low thermal conductivities. Thus, the thermal conductivity of the stator and the rotor in axial direction is calculated as equivalent conductivity of the lamination and the

insulation [101]. Typically, thermal properties of different materials used for our thermal analysis are shown in Table 4.3.

Table 4. 3: Thermal properties of different materials at 20°C

Type	**Material**	**Conductivity (W/m/K)**	**Capacity (J/kg/K)**	**Mass density (kg/m3)**
Lamination	M330-35A	Radial (28) Axial (2)	420	7650
Conductor	Copper	387	380	8960
Wire Insulation	Polyimide	0.26	1000	1440
Shaft	Stainless steel	16.27	502.48	8030
Frame	Aluminum	202.4	871	2719

In order to make the simulation in ANSYS Fluent easier to converge, the machine is simplified as it shown in Figures 4.13 and 4.14.

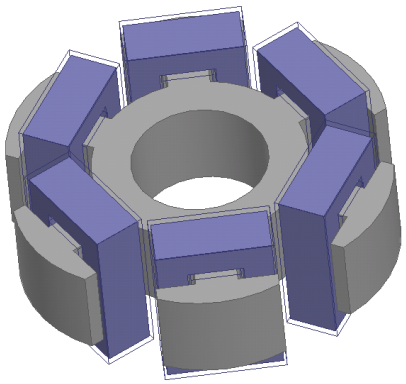

Figure 4. 13: Rotor modelling

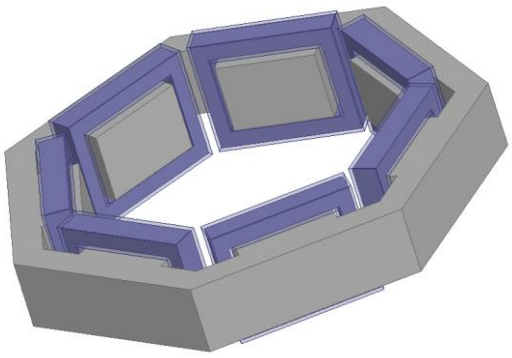

Figure 4. 14: Stator modelling

Heat generation

Electromagnetic losses within different parts of the machine act as the main heat sources, leading to the heating of the machine. In this study, the losses which are considered in our thermal analysis include the core losses of the laminations, the copper losses of the armature and field windings. Each kind of losses need to be determined accurately in order to get an accurate temperature prediction.

Mesh generation

Spatial discretization is the process of dividing the domain into small elements connected at nodes. The collection of the elements is often called "grid". The equations are then solved for each individual element. In the FVM, individual elements in the grid are referred as cells. In our study, ANSYS Meshing is used to generate the array of meshes for the machine. The grids may generally be either structured (consisting of hexahedral cells) or unstructured (consisting of tetrahedral cells). Hexahedral cells are used in regions of constant cross section, or where a controllable cell distribution was required to resolve the geometry and the flow [108].

A poor quality grid can cause the divergence and the inaccuracy of the solution. The quality of grid is measured based on several criteria as follows:

Orthogonal quality for a cell shown in Figure 4.15 is the minimum of $\frac{A_i f_i}{|\overrightarrow{A_i}||\overrightarrow{f_i}|}$ $\frac{A_i c_i}{|\overrightarrow{A_i}||\overrightarrow{c_i}|}$ computed for each face i.

Skewness of cell shown in Figure 4.16 is calculated as:

$$Skewness = \frac{optimal\ cell\ size - cell\ size}{optimal\ cell\ size}$$

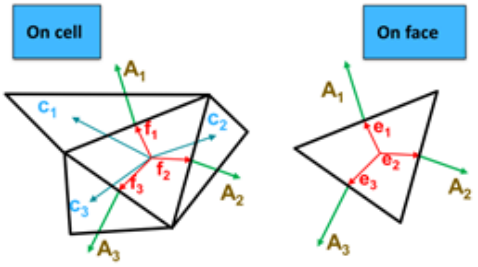

Figure 4. 15: Orthogonal quality [108]

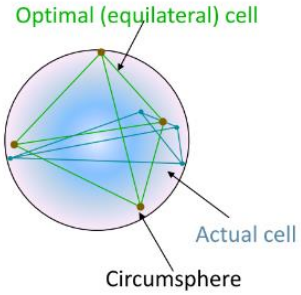

Figure 4. 16: Skewness [108]

Boundary conditions

Actually, the Navier-Stokes equation is a boundary value problem. In CFD analysis, the boundary conditions, and sometimes the initial conditions need to be assigned to determine how the system operates [102], [103]. The typical boundary conditions in CFD are no-slip boundary condition, axisymmetric boundary condition, inlet, outlet boundary condition and periodic boundary condition.

Generally, boundary conditions are necessary for the success of CFD simulation. Regarding inlet and outlet regions, they are faces through which the air gets in and out from the simulation domain as shown in Figure 4.17. Pressure inlet and pressure outlet are used to define flow boundary conditions at the inlet and outlet respectively with zero Pa as relative pressure [104]. For a conjugate heat transfer problem, wall zone is a two-sided wall including wall and its shadow. A subset of these thermal conditions is available, and two sides of the wall can be coupled.

- Inlet: Pressure-inlet (P = 0 Pa), T = 20°C,
- Outlet: Pressure-outlet (P = 0 Pa), T = 20°C,
- Wall of moving fluid: Moving wall,
- The contact interfaces are considered as coupling surfaces.

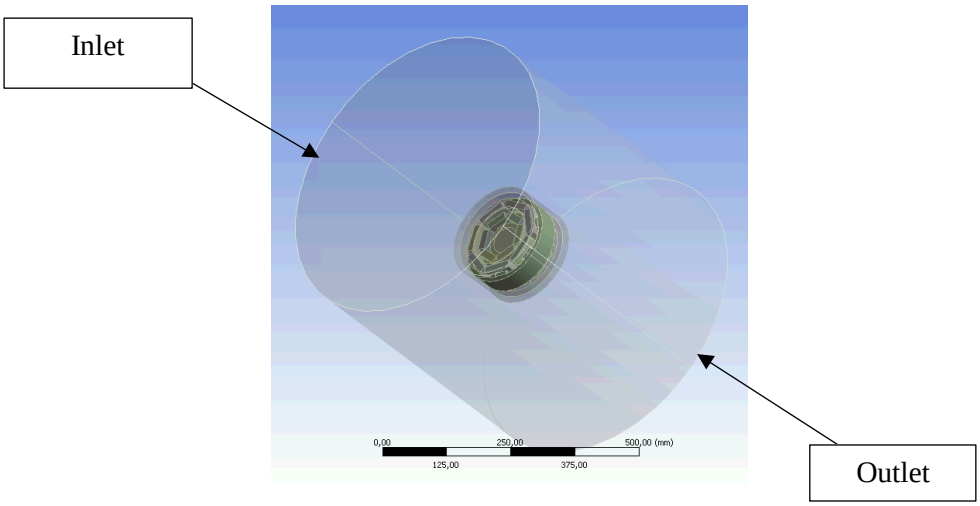

Figure 4. 17: Inlet and outlet regions in our thermal simulation

Modelling technique

The rotation of electrical machines effects on fluid flow and pressure distribution. It is necessary to simulate the rotation of the machine in the modelling. There are two main approaches that can be used: Moving Reference Frame (MRF) and Sliding Mesh (SM). For a steady state analysis, the MRF technique is used and for a transient analysis, the SM technique is used [105].

In our study, the MRF technique is employed to simulate the relative motion of the rotor and of the stator. The fluid region is split into two concentric cylinders by an interior surface shown in Figure 4.18. The inner fluid region is set to rotate at the synchronous speed. The outer fluid region is set to be stationary [111]. The region where MRF is applied does not move physically; however, the rotation of all walls in the MRF region is taken into account to generate a constant grid flux. The grid flux is calculated based on the properties of the reference frame and therefore, the forces due to the rotation are introduced to the MRF region. This approach is suitable for a steady state analysis and it can solve most flow behaviors like mass flow rate and pressure rise across rotating components [106].

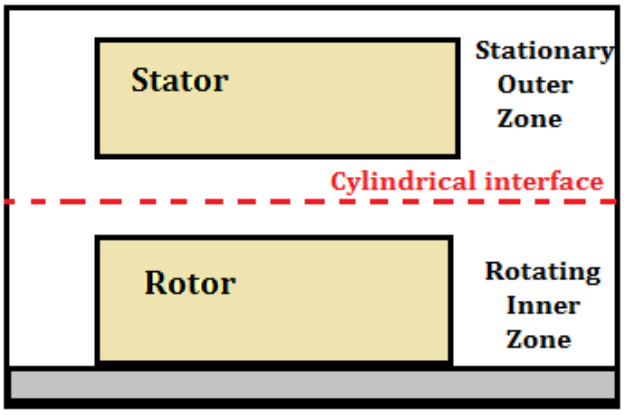

Figure 4. 18: MRF interface of the simplified model

CFD Solver

Two equation turbulence models are usually used for turbulence modelling in the industry: k-ε and k-ω models. These two models include the transport equations for the turbulent kinetic energy k and the dissipation rate of the turbulent energy ε for k-ε models or the specific turbulence dissipation rate ω for k-ω models. The k-ε model is reliable and robust. The standard k-ε turbulence model gives an isotropic turbulence, which is a turbulence constant in all directions. Besides, the realizable k-ε model provides the performances for flows involving rotation, boundary layers under strong adverse pressure gradients, recirculation. The k-ε model provides an isotropic turbulence and easily convergence compared to k-ω. It is commonly used for radial flux machines and has been validated for them by a number of studies [107], [110] and [111]. In this study, the realizable k-ε model with enhanced wall treatment is used because of its robustness. Moreover, the solution methods are adjusted as second order.

ANSYS Fluent steady state rotational, turbulence and conjugate heat transfer modelling options are used to solve the machine model. Cell zone conditions govern the material, heat generation and rotational properties of the solid and fluid zones. Volumetric heat generation rates represent the iron and copper losses. In natural convection, fluid motions are generated due to density differences (buoyancy) in the fluid caused by temperature differences. Therefore, air is considered as incompressible ideal gas with specified operating conditions [108].

4.2.4 CFD Analysis Results

The optimal heptagonal WRSM is modelled which the losses (W) shown in Tables 4.4. From that, the loss densities of different parts are calculated with the unit W/m^3 in Table 4.5.

Table 4. 4: Losses of different machine parts

Stator lamination	Rotor lamination	Stator winding	Rotor winding
48.07	57.87	35.80	51.51

Table 4. 5: Loss densities of different machine parts

Stator lamination	Rotor lamination	Stator winding	Rotor winding
97184	270989	171500	356350

In order to obtain these following results, 13 hours was needed using a PC-server with 16 processors (2.6GHz and 128GB). The machine temperature is analyzed and shown in Figures 4.19 and 4.20.

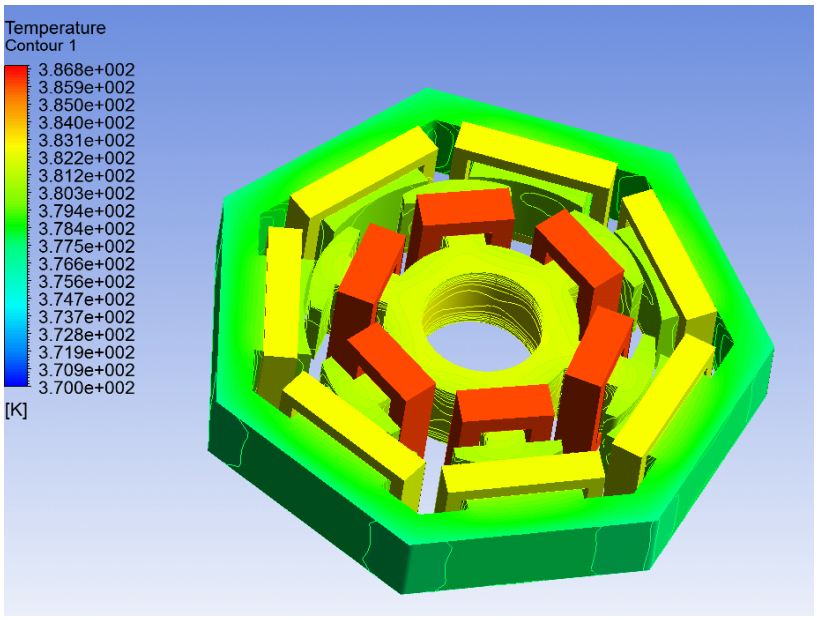

Figure 4. 19: Temperature distribution of the WRSM

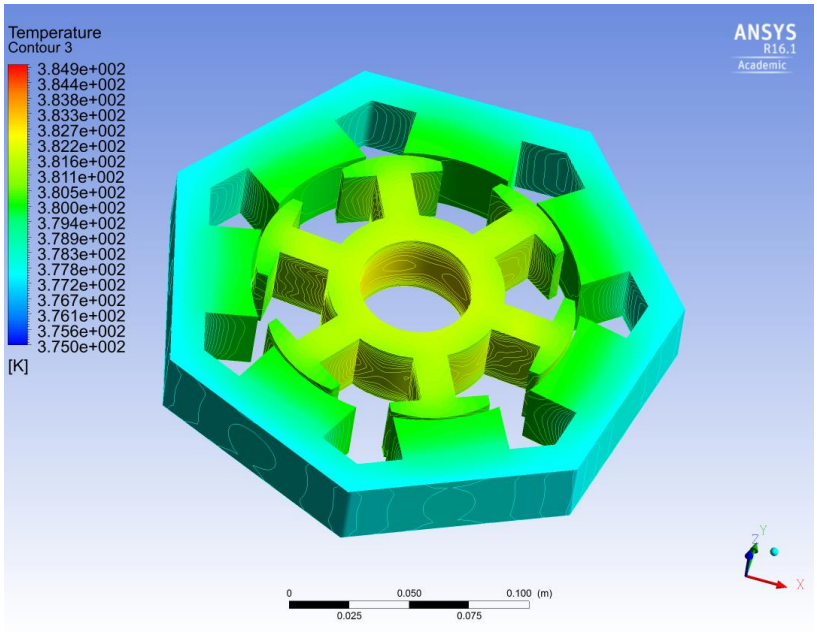

Figure 4. 20: ‘zoom’ on the temperatures of the laminations

The highest temperature in the machine is the temperature of the field winding (113.80°C). The surface temperature of the frame where the power converters are integrated is about 104.48°C. The error of the surface temperature of the frame between the CFD simulation and the analytical equation is about 8.05% with the same value of the losses analyzed by 3D electromagnetic simulation. However, it should be emphasized that only natural convection is investigated in this study. The radiation should be taken into account at the surface of the machine frame for electrical machines without cooling systems.

4.3 Prototype and Experimental Tests

In the following subsections, the prototype machine is described and the static performance measurements are conducted for comparing the results with the 3D numerical results.

4.3.1 Prototype Manufacturing

The prototype machine is a MB-WRSM with 3.67 kW, 7 phases, 7 slots and 6 poles. The laminated rotor and stator is manufactured in the company SEF (Toulouse, France) and in the LAPLACE laboratory (mainly by Dominique Harribey). The properties of the electrical steel laminations are shown in Table 4.6.

Table 4. 6: Properties of the laminations

Thickness	0.35 mm
Width	1000 mm
Length	700 mm
Net Weight	200
Chemical analysis	C, Si, Mn, S
Loss density at 50 Hz, 1 T	0.91 W/kg
Loss density at 50 Hz, 1.5 T	2.23 W/kg

Each segment of the stator core is shown in Figure 4.21. The armature winding is pre-wounded for each segment of the stator core (Figure 4.22). All of the segments are jointed together, so we obtain the stator and the rotor as shown in Figure 4.23. The rotating transformer is fixed on additional extended arrangement for the rotor shaft.

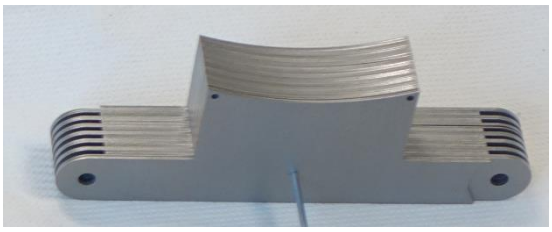

Figure 4. 21: One segment of the stator core

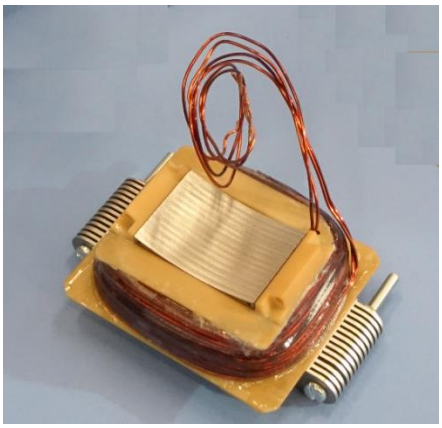

Figure 4. 22: “Pre-wound” stator winding

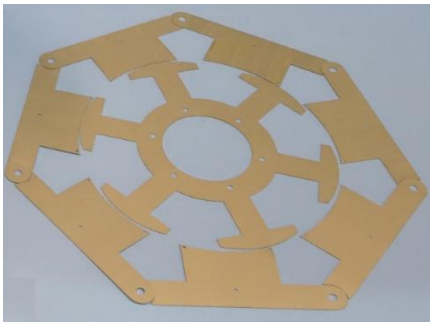

Figure 4. 23: Segmented stator core and rotor core

The prototype machine is shown in Figures 4.24 - 4.26. The outside entire frame has a cylindrical form and the outside holes of the frame contain the power converters whereby each single module supplies the current for each machine phase.

Figure 4. 24: WRSM prototype

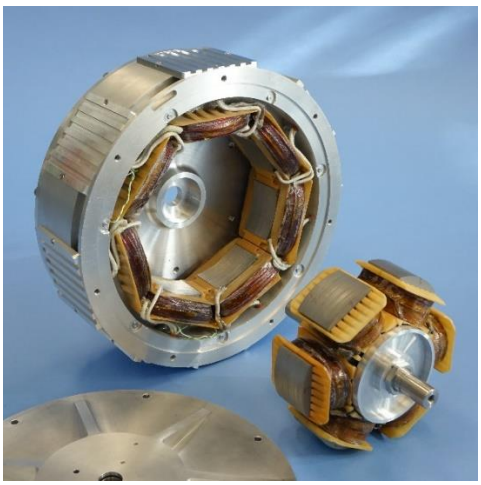

Figure 4. 25: Rotor and stator

Figure 4. 26: Winding and insulation

It is important to emphasize that for the prototype machine, the slot filling factors of both windings are lower than the desired values. These values are calculated as follows:

From the prototype data, the rotor winding has 133 spires with 2 wires (the wire diameter D_{wr}=*0.8mm*) per conductor and the stator winding has 70 spires per phase with 2 wires (the wire diameter D_{ws}=*1mm*) per conductor. Therefore, the copper areas of rotor and stator windings are:

$$A_{cu_r} = 2 \times N_r \times S_{w_r} = 2 \times 133 \times 2 \times {}^{\pi D_{wr}^2}/_4 = 267.41\ mm^2$$

$$A_{cu_s} = 2 \times N_s \times S_{w_s} = 2 \times 70 \times 2 \times {}^{\pi D_{ws}^2}/_4 = 219.91\ mm^2$$

The stator slot area and the area between two rotor poles are computed and verified by using ANSYS Maxwell:

$$A_{slot} = 653.60\ mm^2\ and\ A_{bpole} = 877.175\ mm^2$$

Therefore, the copper slot fill factors of rotor and stator windings are $k_{r_r} = 0.3049\ and\ k_{r_s} = 0.3365$, respectlly. With different values of copper slot fill factors, we keep the same values of both currents like in the design to obtain the same value of the torque. Thus, the current densities are increased from 3.87A/mm^2 to 5.0782A/mm^2 for the rotor winding and from 2.69A/mm^2 to 3.9905A/mm^2 for the stator winding. The performances of the prototype are simulated in 3D and shown in Table 4.7.

Table 4. 7: 3D performances of the prototype machine

Performance	Value	Unit
Average torque	4.99	Nm
Torque ripple	4.02%	
Iron losses	111.06	W
Copper losses	121.10	W
Efficiency	93.95%	
Phase voltage (rms)	94.79	V
Surface temperature	110.25	°C

The average torque shown in Figure 4.27 is about 5Nm and the torque ripple is still lower than 5%. The induced voltage of phase A is shown in Figure 4.28 and thanks to that, we can see that the peak value of the phase voltage calculated is lower than the limited value (800V). Nevertheless, the copper losses are increased so much due to the reduction of the copper slot fill factors (same currents); this leads to increase the surface temperature until to 110.25°C (instead of 96.07°C in 3D). It should be mentioned that for our structure with the segmented stator, the copper slot fill factor is higher than the classical cylindrical structure. Nevertheless, this is the first time we fabricate this structure so that we cannot make sure all of requirements well satisfied. Therefore, a second prototype machine is expected in order to improve the slot fill factors using smaller wires and of winding more efficiently.

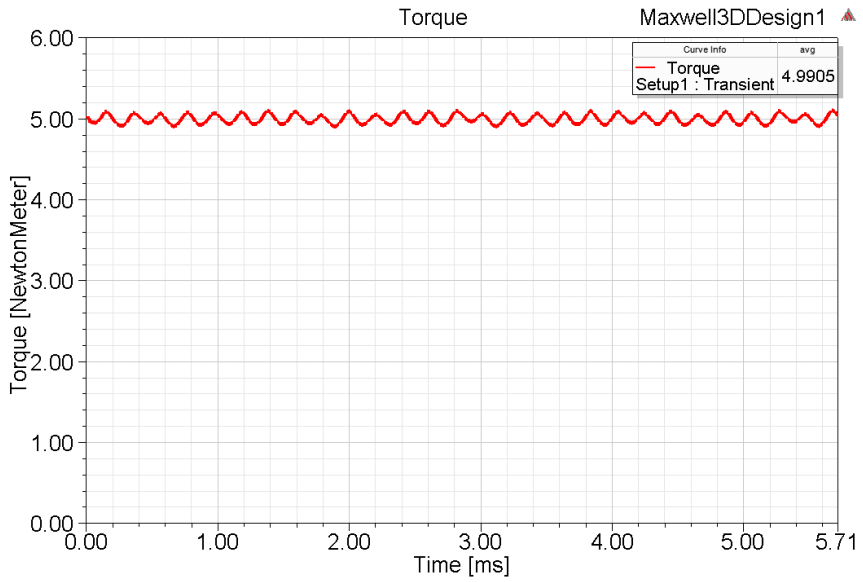

Figure 4. 27: 3D electromagnetic torque of the prototype

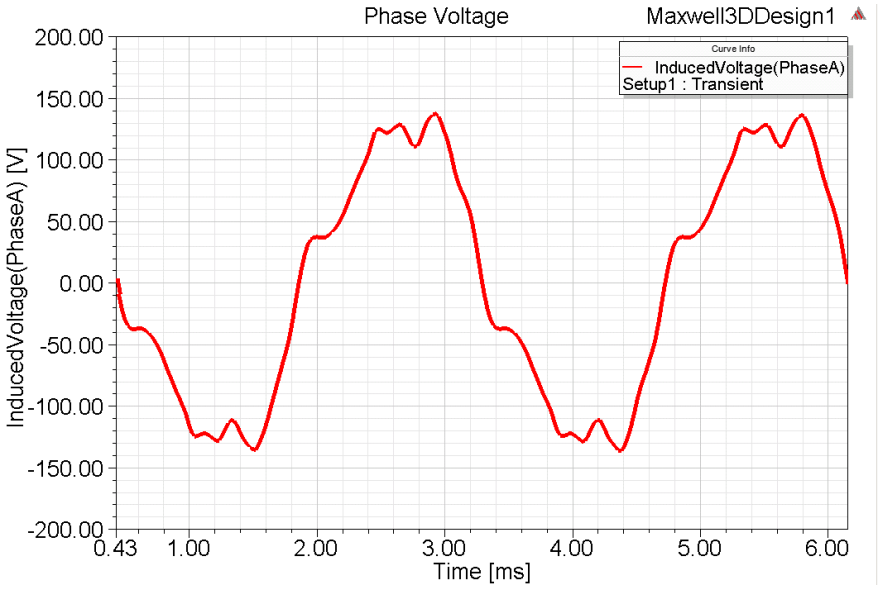

Figure 4. 28: 3D induced voltage of phase A of the prototype

4.3.2 Experimental Tests of the Prototype

The experimental tests of the prototype are carried out in LAPLACE laboratory. With some limitations on the power supply, no load characteristics of WRSM are determined and then, the experimental results are compared to the numerical ones.

EMF waveform at no load

The object of this initial test is to check the machine construction and the system setup; where the prototype is at no load operation, set by only the rotor field winding excited by an external DC power supply. The rotation of the rotor is clockwise and the rotational speed is almost constant at 700rpm. The

value of the excitation current is about 5A. The waveform of EMF is measured and the plot on the oscilloscope for EMF waveform is displayed in Figure 4.29.

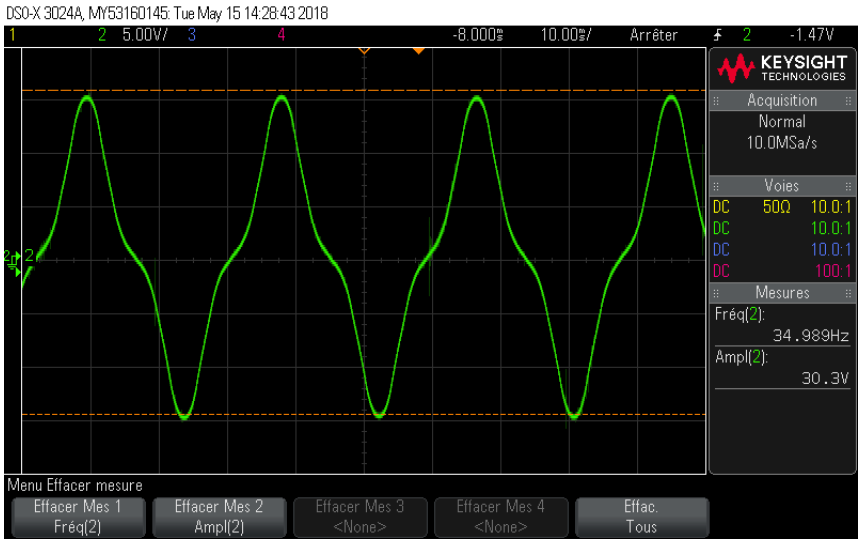

Figure 4. 29: EMF waveform in Oscilloscope

The 3D FE simulation by ANSYS Maxwell is carried out at the same speed and at the same value of the excitation current. Figure 4.30 shows the waveform of the EMF in Maxwell 3D.

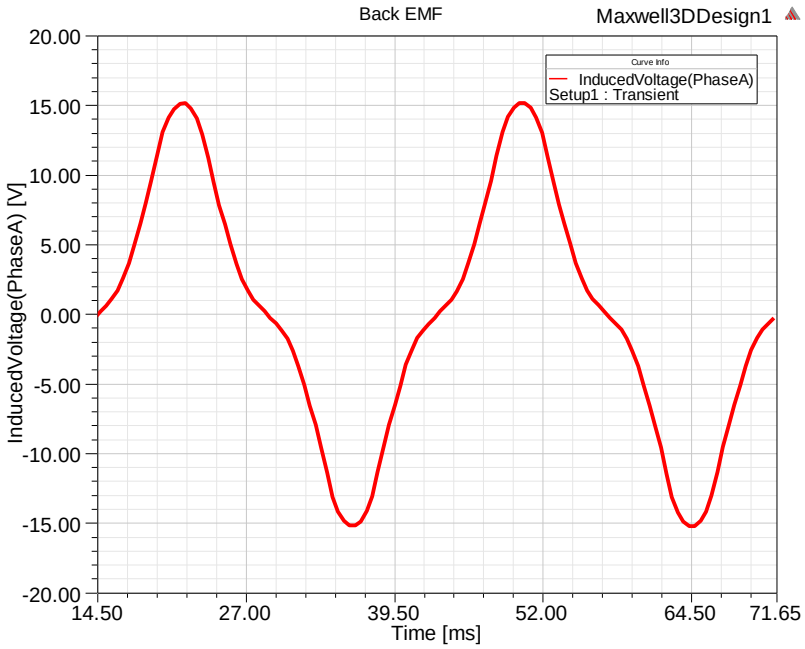

Figure 4. 30: EMF waveform by 3D FE analysis

The EMF comparison at no load between the 3D FE simulation and the experimental test is shown in Figure 4.31. It can be seen that the experimental EMF waveform is similar to the simulated EMF waveform. The waveform of EMF is not perfectly sinusoidal due to the saturation of the induction.

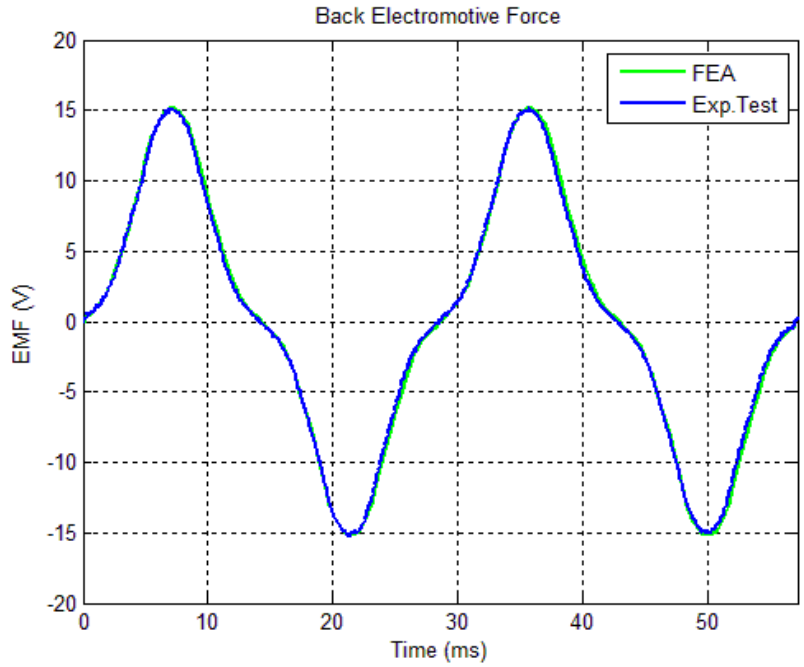

Figure 4. 31: EMF comparison between experimental test and 3D FE analysis

Static torque vs. mechanical rotor angle

The static modelling is constructed in the laboratory and used in order to measure the static torque. In Figure 4.32, the prototype machine coupled with the power supplies is illustrated.

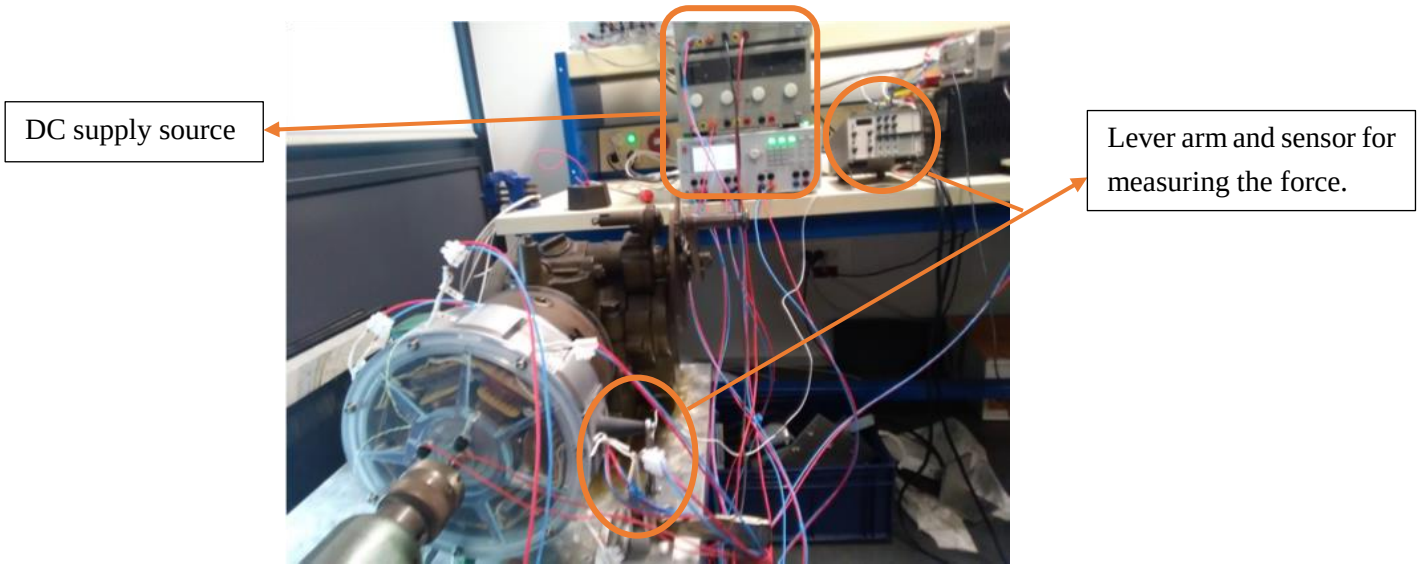

Figure 4. 32: Experimental set-up for testing static torque without converters

The rotor current is excited with 5.10A and the armature current of each phase is fed by a DC current supply source as shown in Table 4.8. The static torque of the prototype machine is measured and shown in Figure 4.33.

Table 4. 8: DC values of armature currents in experimental test

Current	I_A (A)	I_E(A)	I_B(A)	I_F(A)	I_C(A)	I_G(A)	I_D(A)
Value	8.79	-7.99	5.53	-1.97	-1.97	5.53	-7.99

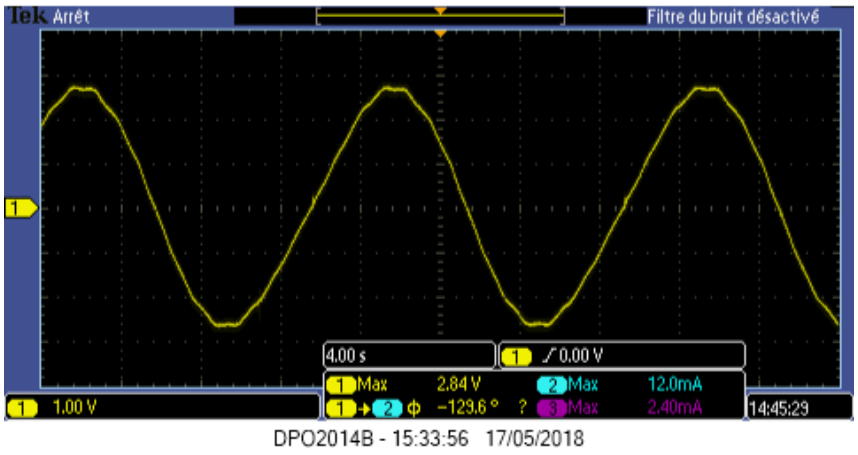

Figure 4. 33: Measured static torque of the prototype

Note that 100N for the force corresponds to 10V of voltage and we use a 175mm lever arm. The so-computed maximum torque is 4.97Nm. For 3D FE simulation, the armature windings are fed with DC currents shown in Table 4.9 and the static torque analyzed in 3D simulation is shown in Figure 4.34.

Table 4. 9: DC values of armature currents in 3D FE analysis

Current	I_A (A)	I_E(A)	I_B(A)	I_F(A)	I_C(A)	I_G(A)	I_D(A)
Value	8.8658	-7.9878	5.5277	-1.9728	-1.9728	5.5277	-7.9878

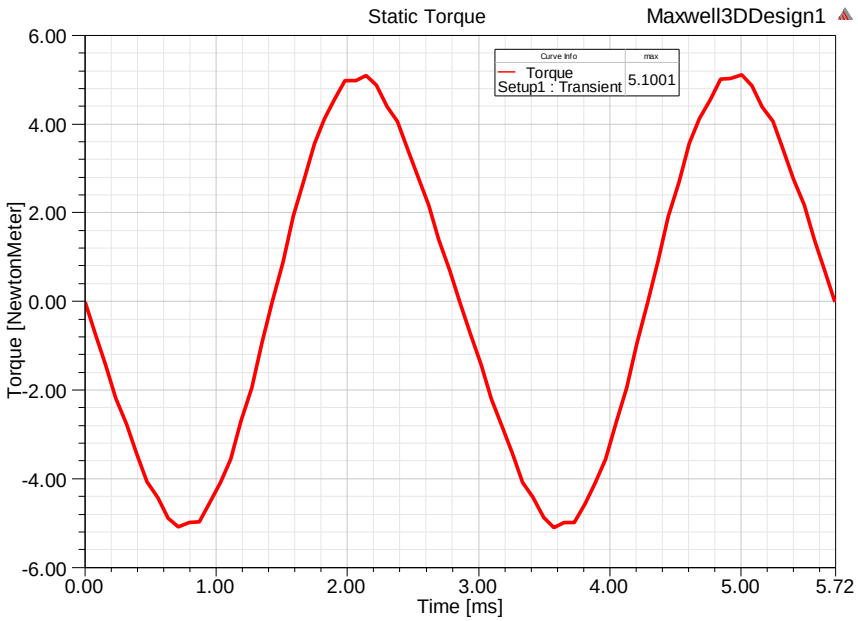

Figure 4. 34: Static torque in 3D FE analysis

The maximum static torque obtained by 3D FE analysis is about 5.10Nm. The comparison of static torque between the measurement and the numerical simulations is shown in Figure 4.35. The result shows that the maximum static torque between the 3D prediction and the real measurement are not so different with a relative error of 2.62%. It should be noted that the small differences between the measured and simulated values can be caused by different values of the currents and the variation in the construction and the measuring process.

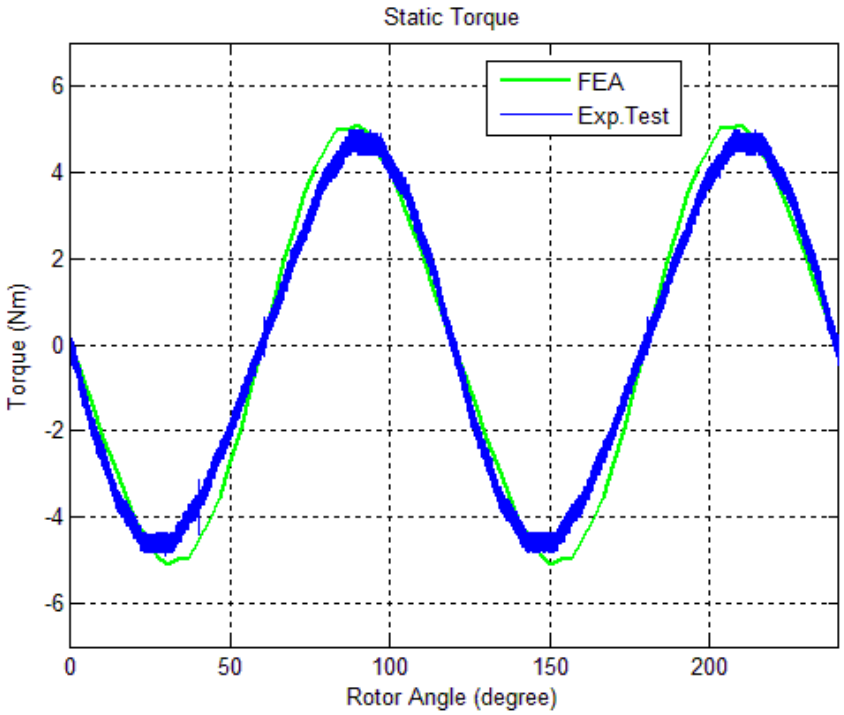

Figure 4. 35: Static torque vs. rotor angle between experimental test and 3D FE analysis

In order to make sure that the maximum static torque is about 5Nm with different values of the time, we measured the static torque for 11 discretization of the power supply between the maximum current of phase A to the maximum current of phase B by changing the time t in the equation of the armature current as:

$$I_{phase_i} = I_s cos\left(wt + \ (i-1)\frac{2\pi}{7}\right) \tag{4.16}$$

Where: I_{phase_i} is the current of phase i, I_s is the peak value of armature current, w is the angular frequency.

In Table 4.10, the maximum static torques for the 11 experimental tests and 2D FE simulations are shown.

Table 4. 10: Maximum static torques with different values of armature currents

Time *t*	**Experimental test (approximations)**	**2D FE analysis (version 15.1)**
0 (I_A:max)	4.96	5.07
$\pi/35$	5.13	5.06
$2\pi/35$	5.04	5.08
$3\pi/35$	5.16	5.08
$4\pi/35$	4.95	5.03
$5\pi/35$	5.06	5.03
$6\pi/35$	5.20	5.06
$7\pi/35$	5.11	5.08
$8\pi/35$	5.06	5.08
$9\pi/35$	5.10	5.03
$10\pi/35$ (I_B:max)	5.13	5.02

For these measurements, the static torques have noise maybe due to the imbalance of the system set-up. Therefore, the maximum static torque is approximated by using basic fitting with spline interpolant method as it is shown in Figure 4.36.

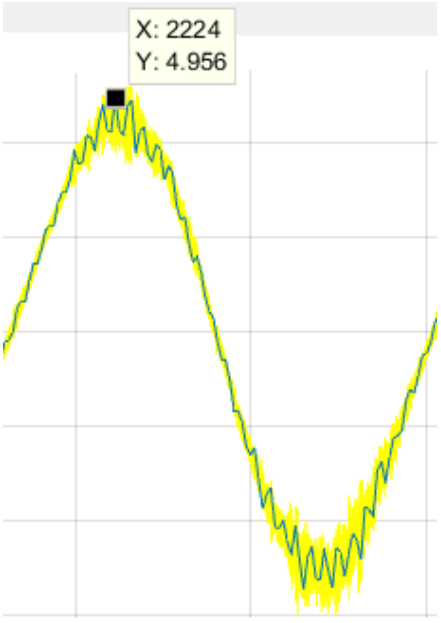

Figure 4. 36: Maximum static torque approximation

From these experimental tests, we obtain that all of the measured static torques correspond to the simulated ones. Thus, we can conclude that the dynamic torque of the prototype will corresponds to the numerical predictions.

4.4 Chapter conclusion

The design optimization based on FE analysis of the MB-WRSM with 7 phases, 7 stator slots and 6 poles were investigated and an optimal solution which the best as possible local solution we found so far is achieved. This optimal solution needs to be verified and validated by using 3D electromagnetic and thermal analyses. The results obtained by using 3D FE simulation via ANSYS Maxwell 16.0 show that the average torque is inferior to 5Nm. Hence, to obtain the desired value of the torque, the length of the optimal machine is rectified and therefore, a new corrected WSRM is so-obtained. We observed that the difference of the average torque is due to the version of ANSYS Maxwell used. Besides, it should be noticed that the iron losses obtained using 3D FE analysis are higher than in 2D. This is due to the high leakage flux in the end-winding of the FSCW. With the values of losses analyzed by 3D FE simulation, the surface temperature of the new corrected machine analyzed by CFD simulation is different compared to the one obtained by the analytical equation. It is important to note that the limit on the coil temperature was fixed to 105°C in order to guarantee a perfect functioning of the WSRM. Thus, in order to obtain that temperature value at the end of this entire design process, a limit of 85°C for the surface temperature had to be fixed into the optimization problem. At the end, the coil temperature of the new corrected WSRM analyzed by CFD method is 113.48°C which is 8.48°C higher than the desired value. This should not be an issue, since we expect to have some dissipation by the shaft and the bearings of the machine. Finally, the prototype machine is built and several experimental tests are carried out. The results show that the back-EMF at no load (700rpm) obtained by the experimental test has a similar waveform compared to that predicted by 3D FE simulation. In addition, the differences of the maximum static torque between the experimental tests and the 3D FE simulations with different discretization of the stator supply are small.

The link you can see the video for the prototype manufacturing and experimental tests is: https://youtu.be/8eoO_WeAPgg with the help of M. Dominique.

General conclusion

The design optimization using numerical models was carried out in order to investigate electromagnetic and thermal characteristics of MB-WRSMs.

The first chapter of the thesis briefly introduced several types of electrical machines which can be used in HVAC application. PMSMs are currently the most popular choice because of its high torque density and high efficiency. However, magnet price is more and more expensive. Therefore, alternative machines without magnets are considered to replace PMSMs in HVAC application. The reasons for choosing MB-WRSM based on a POKI-POKI^{TM} structure were discussed in the first chapter as well. The high fault tolerance capability, a significant improvement of safety, a wide constant power region makes it to become a viable candidate in the next generation of HVAC application.

Chapter 2 focused on the selection of phase/slot/pole combinations and the electromagnetic modelling for different machines in order to select the most appropriate machine which has a high torque density, a high efficiency and a torque ripple lower than 5%. Thanks to this study, the WRSM with 7 phases, 7 slots and 6 poles was selected and then compared to a reference design SM-PMSM with 3 phases, 9 slots and 8 poles in order to evaluate the interest of the selected WRSM. The simulation results were discussed and they demonstrate that the MB-WRSM presents interesting performance features, with overall performances closely matching that of an equivalent SM-PMSM.

Chapter 3 was dedicated to the optimization of a WRSM design. The Quasi-Newton and MADS based algorithms are implemented for two test numerical problems coupled with FE analysis in order to compare their efficiency and their reliability. Consequently, NOMAD solver based on MADS algorithm provides the better solutions for designing WRSMs. Our optimization problem is difficult to solve because the constraint on the coil temperature is complicated to calculate. Therefore, the surface temperature and the efficiency constraints were considered in order to replace the coil temperature constraint. Some tests with this new optimization problem were carried out to find good optimized solutions and then, the optimal result was verified by 2D simulation with fine mesh. Moreover, the validation of the optimal shape was done and we observed the optimal machine has the form like a pancake with a short machine length.

In a fourth and last chapter, the 3D electromagnetic/thermal analyses and experimental tests in order to validate the optimal results obtained in Chapter 3 are presented. Those numerical and experimental results show that in 3D electromagnetic simulation, the iron losses of the machine are higher than the one in 2D simulation due to the leakage flux in the end-winding, leading to the higher temperature of the machine. With the values of the losses analyzed by 3D FE method, the surface temperature of the machine calculated by the equation is not so much different compared to that analyzed by CFD and the

coil temperature is higher about 8.48°C than the desired value (105°C). Finally, the prototype was built and some measurements were performed on the machine. This also proved the correctness of the design and our analysis methodology. Measured back-EMF at no load and static torque characteristics of the machine are similar with the one obtained by 3D numerical design.

Future works

Having the design, manufacturing and several static tests were performed and the results show that the prototype corresponds to our attempts. Complete experimental studies will be done with the drive electronics in a few months later. Here the recommendations will cover the further improvement of the designed machine and also the application related topics.

Firstly, the use of the lumped parameter model which can compute rapidly the machine temperature is necessary in the optimization. Our optimization problem with the constraint on the coil temperature can be thus solved directly and therefore, the optimal results can be better.

Secondly, in order to improve the efficiency of the existing prototype as well as to reduce the machine temperature, the copper slot fill factors should be increased up to 50% for the stator winding and up to 40% for the rotor winding in the prototype machine by using conductors with smaller diameters.

Thirdly, the dynamic torque and the machine temperature should be measured after having the power converters.

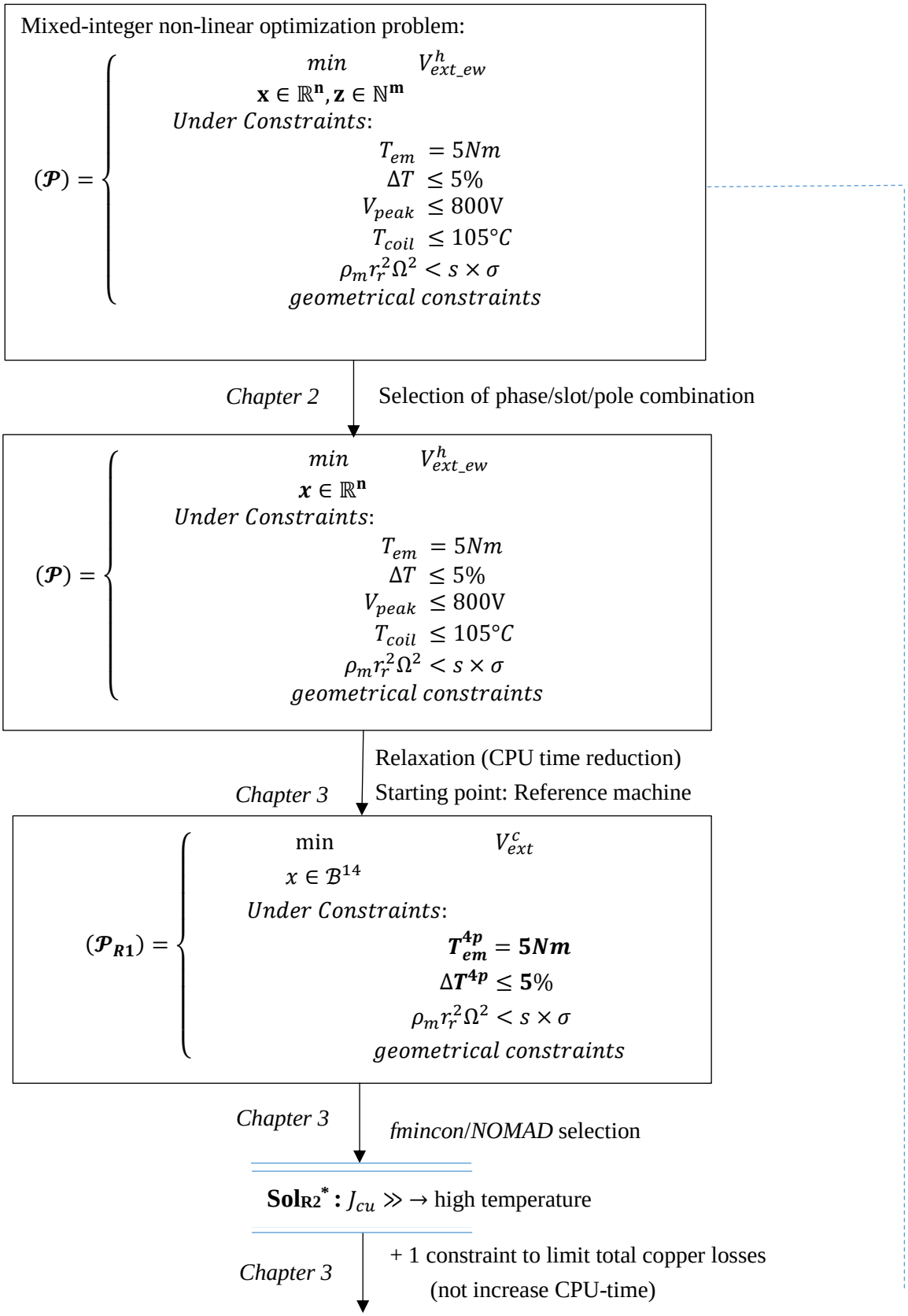
Mixed-integer non-linear optimization problem:
$(\mathcal{P}) = \begin{cases} min \quad V_{ext\_ew}^{h} \\ \mathbf{x} \in \mathbb{R}^{\mathbf{n}}, \mathbf{z} \in \mathbb{N}^{\mathbf{m}} \\ Under\ Constraints: \\ T_{em} = 5Nm \\ \Delta T \leq 5\% \\ V_{peak} \leq 800\text{V} \\ T_{coil} \leq 105°C \\ \rho_m r_r^2 \Omega^2 < s \times \sigma \\ geometrical\ constraints \end{cases}$
Chapter 2
Selection of phase/slot/pole combination
$(\mathcal{P}) = \begin{cases} min \quad V_{ext\_ew}^{h} \\ \boldsymbol{x} \in \mathbb{R}^{\mathbf{n}} \\ Under\ Constraints: \\ T_{em} = 5Nm \\ \Delta T \leq 5\% \\ V_{peak} \leq 800\text{V} \\ T_{coil} \leq 105°C \\ \rho_m r_r^2 \Omega^2 < s \times \sigma \\ geometrical\ constraints \end{cases}$
Relaxation (CPU time reduction)
Chapter 3
Starting point: Reference machine
$(\mathcal{P}_{R1}) = \begin{cases} \min \quad V_{ext}^{c} \\ x \in \mathcal{B}^{14} \\ Under\ Constraints: \\ \boldsymbol{T_{em}^{4p} = 5Nm} \\ \boldsymbol{\Delta T^{4p} \leq 5\%} \\ \rho_m r_r^2 \Omega^2 < s \times \sigma \\ geometrical\ constraints \end{cases}$
Chapter 3
fmincon/*NOMAD* selection
Sol$_{R2}^{*}$: $J_{cu} \gg$ → high temperature
Chapter 3
+ 1 constraint to limit total copper losses
(not increase CPU-time)

$$(\boldsymbol{\mathcal{P}_{R2}}) = \begin{cases} \min & V_{ext}^{c} \\ x \in \mathcal{B}^{14} & \\ Under\ Constraints: & \\ T_{em}^{4p} = 5Nm & \\ \Delta T^{4p} \leq 5\% & \\ \boldsymbol{P_{copper}/P_{out}} \leq \mathbf{3}\% & \\ \rho_m r_r^2 \Omega^2 < s \times \sigma & \\ geometrical\ constraint & \end{cases}$$

Chapter 3

NOMAD and $\mathbf{Sol_{R2}}^{*}$

Chapter 3 + 2 constraints (efficiency and surface temperature)

$$(\boldsymbol{\mathcal{P}_{R3}}) = \begin{cases} min & V_{ext\_ew}^{h} \\ x \in B^{13} & \\ Under\ Constraints: & \\ T_{em}^{120p} = 5Nm & \\ \Delta T^{120\mathrm{p}} \leq 5\% & \\ \boldsymbol{\eta} \geq \mathbf{94}\% & \\ \boldsymbol{T_s} \leq \mathbf{85°C} & \\ \rho_m r_r^2 \Omega^2 < s \times \sigma & \\ geometrical\ constraints & \end{cases}$$

Chapter 3

$\mathbf{Sol_{R3}}^{*}$

Chapter 3

2D FE validation

Chapter 4 End-winding zone modelled

3D electromagnetic validation

Chapter 4 Increase machine length for 5Nm torque

$\mathbf{Sol_{R3}}^{*}$ rectified

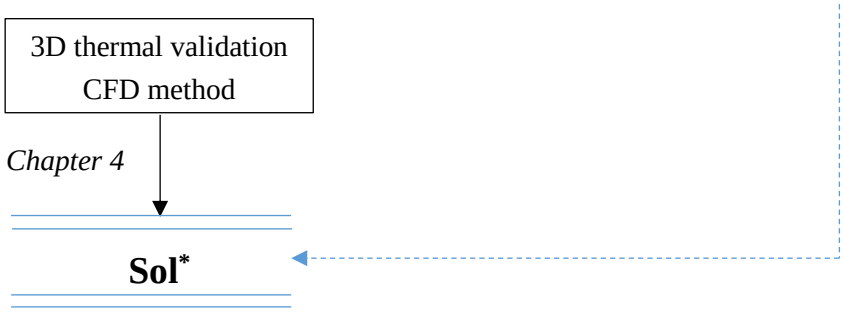
3D thermal validation
CFD method
Chapter 4
Sol*

Reference

[1] Hao Ding, Yingjie Li, Seun Guy Min, and Bulent Sarlioglu, *Electromagnetic and Thermodynamic Design of a Novel Integrated Flux-Switching Motor-Compressor with Airfoil-shaped Rotor*, Wisconsin Electrical machines and Power Electronics Consortium (WEMPEC), IEEE 2017.

[2] Ming-Tsung Chui, Jui-An Chiang, Zwe-Lee Gaing, Yao-Yang Hsieh, *Interior Permanent Magnet Motor with a Novel Tangentially Magnetized Rotor for Refrigerant Compressors*, Electrical Machines and Systems (ICEMS), 20th International Conference, 2017.

[3] James D.Widme, Richard Martin and Mohammed Kimiabeigi, *Electric vehicle traction motors without rare earth magnets*, Sustainable Materials and Technologies, Volume 3, April 2015, Pages 7-13.

[4] Ion Boldea, Lucian N. Tutelea, Leila Parsa, and David Dorrell, A*utomotive Electric Propulsion Systems with Reduced or No Permanent Magnets: An Overview*, IEEE Transactions on Industrial Electronics, Vol. 61, No. 10, October 2014.

[5] Francesco Parasiliti, Marco Villani, Stefano Lucidi, and Francesco Rinaldi, *Finite-Element-Based Multiobjective Design Optimization Procedure of Interior Permanent Magnet Synchronous Motors for Wide Constant-Power Region Operation*, IEEE Transactions on Industrial Electronics, Vol. 59, No. 6, June 2012.

[6] Florin Nicolae Jurca, Mircea Ruba, Claudia Martis, *Analysis of Permanent Magnet Synchronous Machine for Integrated Starter-Alternator-Booster Applications*, International Conference on Electrical Drives and Power Electronics, 2015.

[7] Alexander Stening, *Design and optimization of a surface-mounted permanent magnet synchronous motor for a high cycle industrial cutter*, Master Thesis.

[8] R. Bharanikumar, K.T.Mahaswari and A. Nirmal Kumar, *Comparative Analysis of Permanent Magnet Materials for Wind Turbine Driven Permanent Magnet Generator*, Journal of electrical engineering.

[9] Xiao Chen and Jiabin Wang, *Magneto-motive force Harmonic Reduction Techniques for Fractional-Slot Non-Overlapping Concentrated Winding Configurations in Permanent-Magnet Synchronous Machines*, Chinese Journal of Electrical Engineering, Vol. 3, No. 2, September 2017.

[10] James D.Widmer, Richard Martin, Mohammed Kimiabeigi, *Electric vehicle traction motors without rare earth magnets*, Elsevier B.V, 2015.

[11] Sinisa Jurkovic, Khwaja M. Rahman, John C. Morgante, and Peter J. Savagian, *Induction Machine Design and Analysis for General Motors e-Assist Electrification Technology,* IEEE Transactions on Industrial Applications, Vol. 51, No. 1, January/February 2015.

[12] Akira Chiba, Yuichi Takano, Motoki Takeno, Takashi Imakawa, Nobukazu Hoshi, Masatsugu Takemoto, and Satoshi Ogasawara, *Torque Density and Efficiency Improvements of a Switched Reluctance Motor Without Rare-Earth Material for Hybrid Vehicles*, IEEE Transactions on Industrial Applications, Vol. 47, No. 3, May/June 2011.

[13] Kyohei Kiyota, and Akira Chiba, *Design of Switched Reluctance Motor Competitive to 60 kW IPMSM in Third Generation Hybrid Electric Vehicle*, Energy Conversion Congress and Exposition (ECCE), IEEE, 2011.

[14] Claudio Rossi, Domenico Casadei, Alessio Pilati, Matteo Marano, *Wound Rotor Salient Pole Synchronous Machine Drive for Electric Traction*, Industry Applications Conference, 2006. 41st IAS Annual Meeting. Conference Record of the IEEE, 2006.

[15] Geun-Ho Lee, Heon-Hyeong Lee, and Qi Wang, *Development of Wound Rotor Synchronous Motor for Belt-Driven e-Assist System*, Journal of Magnetics, Volume 18, Issue 4, pp.487-493 2013.

[16] David G. Dorrell, *Are wound rotor synchronous motors suitable for use in high efficiency torque dense automotive drives*?, IECON - 38th Annual Conference on IEEE Industrial Electronics Society, 2012.

[17] Constantin Stancu, Terence Ward, Khwaja Rahman, Robert Dawsey, Peter Savagian, *Separately Excited Synchronous Motor with Rotary Transformer for Hybrid Vehicle Application*, Global Powertrain, General Motors Pontiac, Michigan, Energy Conversion Congress and Exposition (ECCE), 2014.

[18] J. Jürgens, A. Brune, B. Ponick, *Electromagnetic Design and Analysis of a Salient Pole Synchronous Machine with Tooth-Coil Windings for Use as a Wheel Hub Motor in an Electric Vehicle*, Electrical Machines (ICEM) conference, 2014.

[19] Huijuan, Longya Xu, Mingzhu Shangguan, *Finite element Method Simulation of a High Speed Wound Rotor Synchronous Machine*, Electrical Machines and Systems (ICEMS) conference, 2011.

[20] Tayfun Gündogdu, Güven Kömügöz, *Implementation of Fractional Slot Concentrated Winding Technique in Large Salient-Pole Synchronous Generators*, Power Electronics and Machines in Wind Applications (PEMWA), 2012.

[21] I. Topaloglu, C. Ocak, I. Tarimer, *a case study of Getting Performance Characteristics of a Salient Pole Synchronous Hydro Generators*, Electronics and Electrical Engineering No. 1, ISSN 1392-1215, 2010.

[22] D. Lin, P. Zhou, B. He, and N. Lambert, *Steady state and transient parameter computation for wound field synchronous machines*, Electrical Machines (ICEM) conference, 2012.

[23] Barrie C. Mecrow, Alan G. Jack, David J. Atkinson, Simon R. Green, Glynn J. Atkinson, Andrew King, and Brian Green, *Design and Testing of a Four-Phase Fault-Tolerant Permanent-Magnet Machine for an Engine Fuel Pump*, IEEE Transaction on Energy Conversion, Vol. 19, No. 4, December 2004.

[24] Mehdi T. Abolhassani, Hamid A. Toliyat, *Fault Tolerant Permanent Magnet Motor Drives for Electric Vehicles*, Electrical machines and Drives Conference (IEMDC) conference, 2009.

[25] C.J. Ifedi, B.C. Mecrow, S.T.M. Brockway, G.S. Boast, G.J. Atkinson and D. Kostic-Perovic, *Fault-Tolerant In-Wheel Motor Topologies for High Performance Electric Vehicles*, Electrical machines & Drives Conference (IEMDC) conference, 2011.

[26] J.J. Wolmarans, M.B. Gerber, H. Polinder, S.W.H de Haan, J.A. Ferreira, D. Clarenbach, *A 50kW Integrated Fault Tolerant Permanent Magnet Machine and Motor Drive*, Power Electronics Specialists Conference, 2008.

[27] N.R. Brown, T.M. Jahns, R.D. Lorenz, *Power Converter Design for an Integrated Modular Motor Drive,* Conference Record - IAS Annual Meeting (IEEE Industry Applications Society), October 2007.

[28] Jiyao Wang, Ye Li and Yehui Han, *Integrated Modular Motor Drive Design with GaN Power FETs*, IEEE Transaction on Industry Applications, Vol. 51, No. 4, July/August 2015.

[29] Udai Shinpurkar, Henk Polinder, Jan A. Ferreira, *Modularity in Wind Turbine Generator Systems – Opportunities and Challenges*, Power Electronics and Applications (EPE'16 ECCE Europe), 2016.

[30] Georgios Alpogiannis, *Modeling and Topology investigation of Modular Machines for Wind Generator Systems,* Thesis for the degree of Master in Electrical Engineering, 2016.

[31] Guang-Jin Li, Zi-Qiang Zhu, Martin P. Foster, Dave A. Stone, and Han-Lin Zhan, *Modular Permanent Magnet Machines with Alternate Teeth having Tooth Tips,* IEEE Transaction on Industry Electronics, Vol. 62, No. 10, October 2015.

[32] *Motor Technologies for Industry and Daily Life Edition*, Mitsubishi Electric Advance, Vol. 103, Sep. 2003.

[33] M. Zeraoulia, M. Benbouzid and D. Diallo, *Electric motor drive selection issues for HEV propulsion systems: A comparative*, IEEE Transaction on Vehicle Technology, Vol. 55, No. 6, pp. 1756-1764, Nov. 2006.

[34] Mattia Tosi, *Rotary Transformer Design for Brushless Electrically Excited Synchronous Machines*, Phd Thesis of Università degli Studi di Padova.

[35] Enzo llliano, *Design of a Brushless Separately Excited Synchronous Motor,* Swiss Federal Institute of Technology Zurich.

[36] Frédéric Messine and Bertrand Nogarede, *Optimal Design of Multi-Airgap Electrical Machines: An Unknown Size Mixed-Constrained Global Optimization Formulation*, IEEE Transactions on Magnetics, Vol. 42, No. 12, March 2006.

[37] Julien Fontchastagner, Frédéric Messine, and Yvan Lefèvre, *Design of Electrical Rotating Machines by Associating Deterministic Global Optimization Algorithm with Combinatorial Analytical and Numerical Models*, IEEE Transactions on Magnetics, Vol. 43, No. 8, August 2007.

[38] Satafa Sanogo, Frédéric Messine, Carole Hénaux, and Raphaël Vilamot, T*opology Optimization for Magnetic Circuits Dedicated to Electric Propulsion*, IEEE Transactions on Magnetics, Vol. 50, No. 12, Decembre 2014.

[39] Frédéric Gillon and Pascal Brochet, *Screening and Response Surface Method Applied to the Numerical Optimization of Electromagnetic Devices*, IEEE Transactions on Magnetics, Vol. 36, No. 4, July 2000.

[40] Pierre-Hadrien Arnoux, Pierre Caillard, and Fréderic Gillon, *Modeling Finite-Element Constraint to Run an Electrical Machine Design Optimization Using Machine Learning*, IEEE Transactions on Magnetics, Vol. 51, No. 3, March 2015.

[41] Jean-Frédéric Charpentier and Guy Lemarquand, *Optimal Design of Cylindrical Air-Gap Synchronous Permanent Magnet Couplings*, IEEE Transactions on Magnetics, Vol. 35, No. 2, July 1999.

[42] Frédéric Messine, Bertrand Nogarede, and Jean-Louis Lagouanelle, *Optimal Design of Electromechanical Actuators: A New Method Based on Global Optimization*, IEEE Transactions on Magnetic, Vol. 34, No. 1, January 1998.

[43] I. Mazhoud, K. Hadj-Hamou, J. Bigeon, and G. Remy, *the Electromagnetic Actuator Design Problem: An Adapted Interval Global Optimization Algorithm*, IEEE Transactions on Magnetic, Vol. 48, No. 2, February 2012.

[44] M Lukaniszyn, M. JagieLa,R. Wrobel, *Optimization of permanent magnet shape for minimum cogging torque using a genetic algorithm*, IEEE Transactions on Magnetics, Vol. 40, Iss. 2, March 2004, pp. 1228-1231. Astrid Rokke.

[45] Dong-Joon Sim, Dong-Hyeok Cho, Jang-Sung Chun and Hyun-Kyo Jung, *Efficiency optimization of Interior Permanent Magnet Synchronous using Genetic Algorithms*, IEEE Transactions on Magnetics, Vol. 33, No. 2, March 1997.

[46] Pedram Elhaminia, Masoud Yazdanian, Mohammad Reza Zolghadri, and Mehdi Fardmanesh, *Optimal Electromagnetic Design of a Nonsalient Magnetic-Cored Superconducting Synchronous Machine Using Genetic Algorithm*, IEEE Transactions on Applied Superconductivity, Vol. 25, No. 1, February 2015.

[47] Stephen J. Wright, *Numerical Optimization*, Jorge Nocedal, ISBN 0-387-98793-2 Springer-Verlag New York Berlin Heidelberg SPIN 10764949.

[48] Byrd, R.H., Mary E. Hribar, and Jorge Nocedal, *An Interior Point Algorithm for Large-Scale Nonlinear Programming*, SIAM Journal on Optimization, Vol 9, No. 4, pp. 877–900, 1999.

[49] Coleman, T.F. and Y. Li, *On the Convergence of Reflective Newton Methods for Large-Scale Nonlinear Minimization Subject to Bounds*, Mathematical Programming, Vol. 67, Number 2, pp. 189–224, 1994.

[50] C. Audet, A. Ihaddadene, S. Le Digabel, and C. Tribes, *Robust optimization of noisy blackbox problems using the Mesh Adaptive Direct Search algorithm*, Technical Report G-2016-55, Les cahiers du GERAD, 2016.

[51] Sébastien Le Digabel, *Algorithm xxx: NOMAD: Nonlinear Optimization with the MADS algorithm*, August 27, 2010.

[52] Sébastien Le Digabel, *Blackbox optimization with the NOMAD software*, GERAD and ´Ecole Polytechnique de Montréal (MAGI), Canmet Energie, 2015.

[53] C. Audet, A.L. Custódio, and J.E. Dennis, Jr. Erratum, *Mesh adaptive direct search algorithms for constrained optimization*, SIAM Journal on Optimization, 18(4):1501–1503, 2008.

[54] Dongsu Lee, Jong-Wook Kim, Cheol-Gyun Lee, and Sang-Yong Jung, *Variable Mesh Adaptive Direct Search Algorithm Applied for Optimal Design of Electrical Machines Based on FEA*, IEEE Transaction on Magnetics, Vol. 47, No. 10, October 2011.

[55] Jin Hwan Lee, Jong-Wook Kim, Jun-Young Song, Yong-Jae Kim, and Sang-Yong Jun, *A Novel Memetic Algorithm Using Modified Particle Swarm Optimization and Mesh Adaptive Direct Search for PMSM Design*, IEEE Transaction on Magnetics, Vol. 52, No. 3, March 2016.

[56] Myung-Ki Seo, Tae-Yong Lee, Jong-Wook Kim, Yong-Jae Kim, and Sang-Yong Jung, *Principal Component Optimization with Mesh Adaptive Direct Search for Optimal Design of IPMSM*, IEEE Transaction on Magnetics, Vol. 53, No. 6, June 2017.

[57] Alberto Rossi, *Développement d'outils d'optimisation dédies aux circuits magnétiques des propulseurs á effet Hall*, PhD thesis of INP Toulouse.

[58] A.J. Mitcham, G. Antonopoulos and J.J.A. Cullen, *Favourable slot and pole number combinations for fault-tolerant PM machines*, IEE Proceedings - Electric Power Applications, Vol. 151, 2004.

[59] Ayman M. EL-Refaie, *Fractional Slot Concentrated Windings synchronous permanent magnet Machines: Opportunities and Challenges*, IEEE Transactions on Industrial Electronics, Vol. 57, No. 1, 2010.

[60] Johannes J. Germishuizen and Maarten J. Kamper, *IPM Traction Machine with Single Layer Non*-Overlapping Concentrated Windings, IEEE Transaction on Industry Applications, Vol. 45, No. 4, July/August 2009.

[61] Giulio De Donato, Fabio Giulii Capponi, Giovanni Antonio Rivellini, and Federico Caricchi, *Integral-Slot Versus Fractional-Slot Concentrated-Winding Axial Flux Permanent Magnet Machines: Comparative Design, FEA and Experimental Tests*, EEE transactions on industry applications, Vol. 48, No. 5, 2012.

[62] Jinghua Ji, Haiyou Chen, and Wenxiang Zhao, *Reduction of Eddy Current Loss of Permanent-Magnet Machines with Fractional Slot Concentrated Windings*, Progress in Electromagnetics Research Letters, Vol. 56, 39-46, 2015.

[63] Nicola Bianchi, Silverio Bolognani, Michele Dai Pré, and Giorgio Grezzani, *Design Considerations for Fractional-Slot Winding Configurations of Synchronous Machines* IEEE Transactions on Industry Applications, Vol. 42, No. 4, July/August 2006.

[64] A.M. El-Refaie, M.R. Shah, J.P. Alexander, S. Galioto, Kum-Kang Huh, W.D. Gerstler, *Rotor end losses in multi-phases fractional-slot concentrated-winding permanent magnet synchronous machines*, Energy Conversion Congress and Exposition (ECCE), Sept. 2010.

[65] Jéröme Cros and Philippe Viarouge, *Synthesis of high performance PM Motors with concentrated windings*, IEEE Transactions on energy conversion, vol. 17, No. 2, June 2002.

[66] Ayman M. EL-Refaie, Manoj R. Shah, Ronghai Qu, and John M. Kern, *Effect of Number of phases on losses in Conduction Sleeves of Surface PM Machine Rotors Equipped with Fractional-Slot Concentrated Windings*, IEEE Transactions on Industry Applications, Vol. 44, No. 5, 2008.

[67] Florence Meier, *Permanent-Magnet Synchronous Machines with Non-Overlapping Concentrated Windings for Low-Speed Direct-Drive Applications*, PhD Thesis, Royal Institute of Technology School of Electrical Engineering Electrical Machines and Power Electronics, Stockholm 2008.

[68] Pia Salminen, *Fractional Slot Permanent Magnet Synchronous Motors for Slow Speed Applications*, PhD Thesis, Lappeenranta University of Technology, Finland 2004.

[69] N. Bianchi and M. Dai Pré, *Using of the star of slots in designing fractional slot single-layer synchronous motors*, IEE Proceedings - Electric Power Applications, Vol 153, 2006.

[70] Juha Pyrhönen, Tapani Jokinen and Valéria Hrabovcova, *Design of Rotating Electrical Machines*, 2008 John Wiley & Sons, Ltd. ISBN: 978-0-470-69516-6.

[71] Qasim Ali, Thomas A. Lipo and Byung-il Kwon, *Design and Analysis of Novel Brushless Wound Rotor Synchronous Machine*, IEEE Transaction on magnetics, 2015.

[72] Huijuan Liu, Longya Xu, Mingzhu Shangguan, and W. N. Fu, *Finite Element Analysis of 1 MW high speed wound rotor synchronous machine*, IEEE Transactions on Magnetics, Vol. 48, No. 11, November 2012.

[73] L. Vandenbossche, S. Jacobs, D. Van Hoecke, B. Weber, E. Leunis, E. Attrazic, *Improved iron loss modeling approach for advanced electrical steels operating at high frequencies and high inductions in automotive machine*, Electric Drives Production Conference (EDPC), 2012.

[74] Andreas Krings, *Iron losses in electrical machines - influence of material properties, manufacturing processes, and inverter operation*, Sweden 2014.

[75] Choong-Sung Lee, Ji-Hyun Kim, Jung-Pyo Hong, *Core loss effects on electrical steel sheet of Wound Rotor Synchronous Motor for integrated starter generator*, Journal of Magnetics Vol.20 No.2, 2015.6, 148-154.

[76] Ion Boldea, *The Electric Generators Handbook – Synchronous Generators*, Polytechnical Institute Timisoara, Romania.

[77] M. Liwschitz, L. Maret, *Calcul des machines électriques 1,2*, Bibliothèque de l'ingénieur.

[78] ANSYS Maxwell 2D/3D user's guide.

[79] Philip A. Hargreaves, Barrie C. Mecrow, and Ross Hall, *Calculation of Iron Loss in Electrical Generators Using Finite-Element Analysis*, IEEE Transactions on industry applications, Vol. 48, No. 5, 2012.

[80] K. Lakshmi Varaha Iyer, Bruce Minaker, Kaushik Mukherjee and Jimi Tjong, Narayan C. Kar, *On-board Direct-Drive Surface Permanent Magnet Synchronous Machine with Fractional-Slot Concentrated Windings for Electric Vehicles*, IEEE Canadian Conference on Electrical and Computer Engineering (CCECE), 2016.

[81] Li Junlong, Xu Yongxiang, Zou Jibin, Wang Baochao, Wang Qian, and Liang Weiyan, *Analysis and Design of SPM Machines with Fractional Slot Concentrated Windings for a Given Constant Power Region*, IEEE Transactions on Magnetics, Vol. 51, No. 11, 2015.

[82] Jiabin Wang, Xibo Yuan, and Kais Atalla, *Design Optimization of a Surface-Mounted Permanent-Magnet Motor with Concentrated Windings for Electric Vehicle Applications*, IEEE Transactions on Vehicular Technology, Vol. 62, No. 3, 2013.

[83] Jan Rens, Sigrid Jacobs, Lode Vandenbossche, Emmanuel Attrazic, *Effect of stator segmentation and manufacturing degradation on the performance of IPM machines, using iCARe® electrical steels*, World Electric Vehicle Journal, Vol. 8, ISSN 2032-6653, Canada, June 2016.

[84] Ilya Petrov, *Cost reduction of permanent magnet synchronous machines*, Thesis for the degree of Doctor of Science in the Auditorium 1382 at Lappeenranta University of Technology, Finland, June 2015.

[85] Zhu, Z.Q., Azar, Z., and Ombach, G., *Influence of Additional Air Gaps between Stator Segments on Cogging Torque of Permanent-Magnet Machines Having Modular Stators*, IEEE Transactions on Magnetics, vol.48, no.6, pp. 2049– 2055, 2012.

[86] Nikita Uzhegov, Janne Nerg and Juha Pyrhönen, *Design of 6-slot 2-pole High-Speed Permanent Magnet Synchronous Machines with Tooth-Coil Windings*, International Conference on Electrical Machines (ICEM), 2014.

[87] Phase Motion Control Ningbo LTD, *Stator coil winding*, [online] http://www.phasemotorparts.com/showing_149_149/stator-coilwinding.html, 2012.

[88] Daniel Marcsa, *Induction Motors Simulation by Finite Element Method and Different Potential Formulations with Motion Voltage T*erm, A Thesis submitted to the Széchenyi Istvan University for the degree of Bachelor of Science in Electrical Engineering, 2008.

[89] Dan M. Ionel, and Mircea Popescu, *Finite-Element Surrogate Model for Electrical Machines with Revolving Field—Application to IPM Motors*, IEEE Transactions on Industry Applications, Vol. 46, No. 6, November/December 2010.

[90] M. H. Mohammadi, T. Rahman, R. Silva, M. Li, and D. A. Lowther, *A Computationally Efficient Algorithm for Rotor Design Optimization of Synchronous Reluctance Machines*, IEEE Transactions on Magnetics, Vol. 52, No. 3, March 2016.

[91] Peng Zhang, Gennadi Y. Sizov, Muyang Li, Dan M. Ionel, Nabeel A. O. Demerdash, Steven J. Stretz, and Alan W. Yeadon, *Multi-Objective Tradeoffs in the Design Optimization of a Brushless Permanent-Magnet Machine with Fractional-Slot Concentrated Windings, IEEE Transactions on Industry Applications*, Vol. 50, No. 5, October 2014.

[92] Xikai Sun, Ming Cheng, Wei Hua, and Longya Xu, *Optimal Design of Double-Layer Permanent Magnet Dual Mechanical Port Machine for Wind Power Application*, IEEE Transaction on Magnetics, Vol. 45, No. 10, October 2009.

[93] https://fr.mathworks.com/products/optimization.html.

[94] Han-Kyeol Yeo, Hyeon-Jeong Park, Jung-Moo Seo, Sang-Yong Jung, Jong-Suk Ro, and Hyun-Kyo Jung, *Electromagnetic and Thermal Analysis of a Surface-Mounted Permanent-Magnet Motor with Overhang Structur*e, IEEE Transactions on Magnetics, Vol. 53, No. 6, June 2017.

[95] Roman Pechanek, Vladimir Kindl, Bohumil Skala, *Transient thermal analysis of small squirrel cage motor through coupled FEA*, Science Journal, 2015.

[96] Aldo Boglietti, Andrea Cavagnino, David Staton, Martin Shanel, Markus Mueller, and Carlos Mejuto, *Evolution and Modern Approaches for Thermal Analysis of Electrical Machines*, IEEE Transactions of Industrial Electronics, Vol. 56, No. 3, March 2009.

[97] Xinggang Fan, Ronghai Qu, Jian Li, Dawei Li, Bin Zhang and Cong Wang, *Ventilation and Thermal Improvement of Radial Forced Air-Cooled FSCW Permanent Magnet Synchronous Wind Generators*, IEEE Transactions on Industry Applications 2017.

[98] A. B. Nachouane, A. Abdelli, G. Friedrich, and S. Vivier, *Estimation of Windage Losses Inside Very Narrow Air Gaps of High Speed Electrical Machines without an Internal Ventilation using CFD Methods*, Electrical Machines (ICEM) - XII International Conference 2016.

[99] R. Pechanek, L. Bouzek, *Analyzing of Two Types Water Cooling Electric Motors using Computational Fluid Dynamics*, 15th International Power Electronics and Motion Control Conference, EPE-PEMC 2012 ECCE Europe, Novi Sad, Serbia.

[100] Aldo Boglietti, Enrico Carpaneto, Marco Cossale, Silvio Vaschetto, Mircea Popescu, and David Alan Staton, *Stator Winding Thermal Conductivity Evaluation: An Industrial Production Assessment*, IEEE Transactions on Industry Applications, vol. 52, No. 5, 2016.

[101] Mariia Polikarpova, *Liquid Cooling Solutions for rotating Permanent Magnet Synchronous Machines*, Thesis for the degree of Doctor of Science (Technology) at Lappeenranta University of Technology, Lappeenranta, Finland on the 21st of November, 2014.

[102] James Kuria, Pyung Hwang, *Optimizing Heat Sink Geometry for Electric Vehicle BLDC Motor using CFD*, Sustainable Research and Innovation Proceedings 3, 122-146, 2011.

[103] Yiping Lu, Li Liu, and Dongxue Zhan, *Simulation and Analysis of Thermal Fields of Rotor Multislots for Nonsalient-Pole Motor*, IEEE Transactions of Industrial Electronics, Vol. 62, No. 12, December 2015.

[104] Shuye Ding, Hailing Li, *Investigation of Characteristics of Fluid Flow Pattern for Air-cooled Motor*, Industrial Electronics and Applications (ICIEA), 11th Conference IEEE 2016.

[105] Peter H. Conner, Steve J. Pickering, Chris Gerada, Carol N. Eastwick, Chris Micallef, Chris Tighe, *Computational fluid dynamics modelling of an entire synchronous generator for improved thermal management*, IET Electric Power Applications, 2012.

[106] P.H. Connor, S.J. Pickering, C. Gerada, C.N. Eastwick, C. Micallef, *CFD modelling of an entire synchronous generator for improved thermal management*, Power Electronics, Machines and Drives (PEMD), 6th IET International Conference, 2012.

[107] Unai SanAndres, Gaizka Almandoz, Javier Poza and Gaizka Ugalde, *Design of Cooling Systems using Computational Fluid Dynamics and Analytical Thermal Models*, IEEE Transactions of Industrial Electronics, Vol. 61, No. 8, August 2014.

[108] ANSYS Fluent user's guide.

[109] Chong Yew Chuan, *Thermal analysis and air flow modelling of electrical machines*, PhD thesis, 2015.

[110] C.H. Lim, G. Airoldi, J.R. Bumby, R.G. Dominy, G.I. Ingram, K. Mahkamov, N.L. Brown, A. Mebarki, M. Shanel, *Experimental and CFD investigation of a lumped parameter thermal model of a single-sided, slotted axial flux generator*, International Journal of Thermal Sciences 49, 2010.

[111] P. H. Connor, C. N. Eastwick, S. J. Pickering, C. Gerada, R. Rolston, *Stator and Rotor Vent Modelling in a MVA rated Synchronous Machine*, Electrical Machines (ICEM) - XII International Conference 2016.

[112] Airoldi, Giovanni, *Numerical Investigations of Air Flux and Heat Transfer in Axial Flux Permanent Magnet Electrical Machines*, Durham theses, Durham Unveristy, 2010.

[113] SONG Jianyu, *Chapter 2 Aerodynamics: Some Fundamental Principles and Equations*, February 2009.

Annexes

Annex 1: 2D FE analysis of SM-PMSM and WRSM

The performances of 3-phases/9-slots/ 8-poles SM-PMSM

Figure 1 shows the sinusoidal input currents supplied for the armature windings of the SM-PMSM.

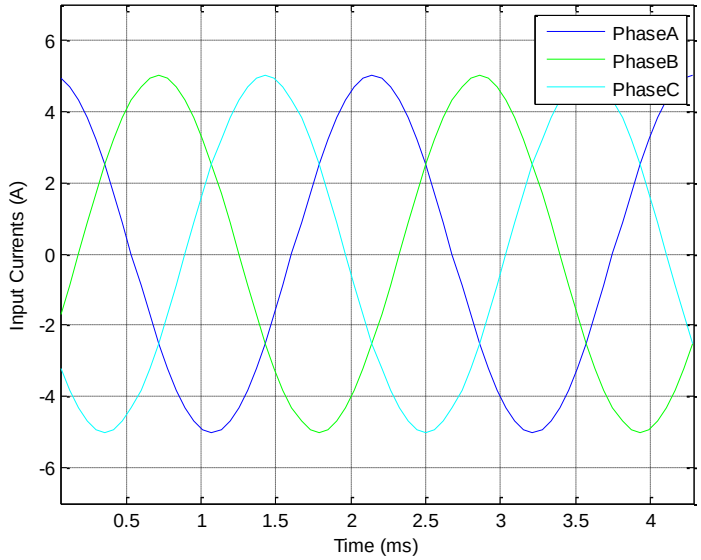

Figure 1: 3-phase sinusoidal input currents for SM-PMSM

In Figure 2, the magnetic flux of each phase is presented. Note that the waveform of the magnetic flux of the SM-PMSM is nearly sinusoidal.

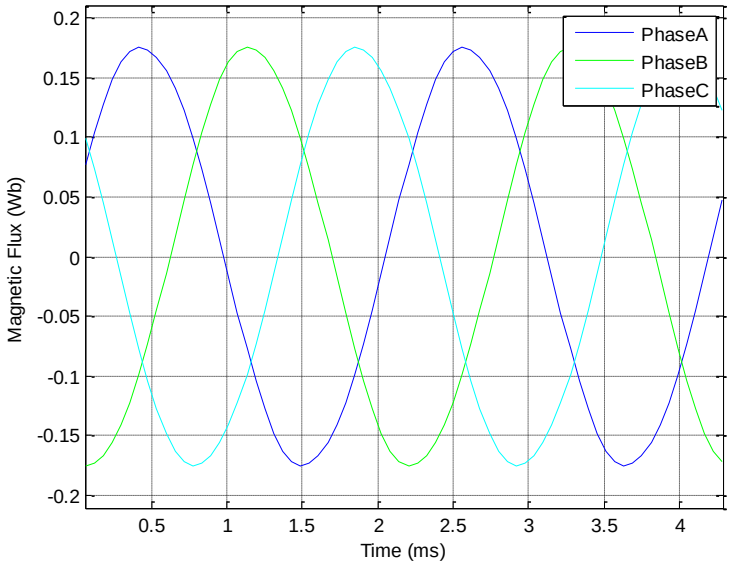

Figure 2: Magnetic flux of the SM-PMSM

The voltages of three phases are indicated in Figure 3.

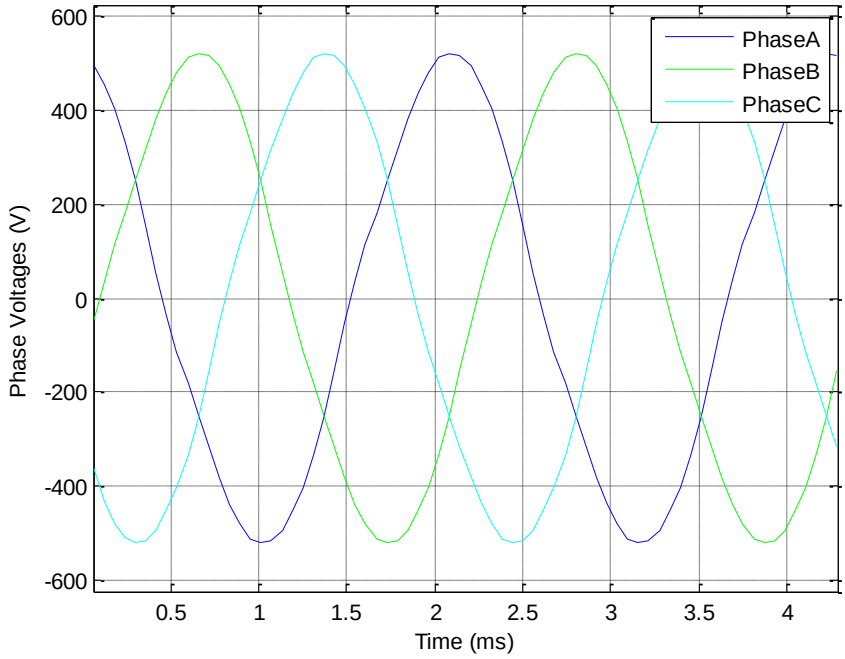

Figure 3: Induced voltage of three phases of SM-PMSM

The electromagnetic torque of the SM-PMSM is shown in Figure 4.

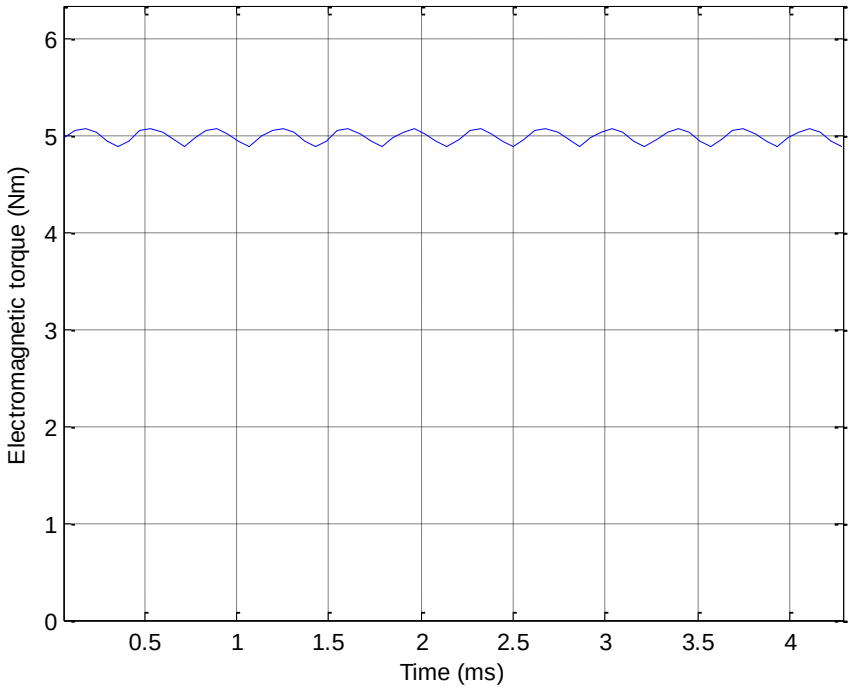

Figure 4: Electromagnetic torque of the SM-PMSM

The core losses of the SM-PMSM are shown in Figure 5.

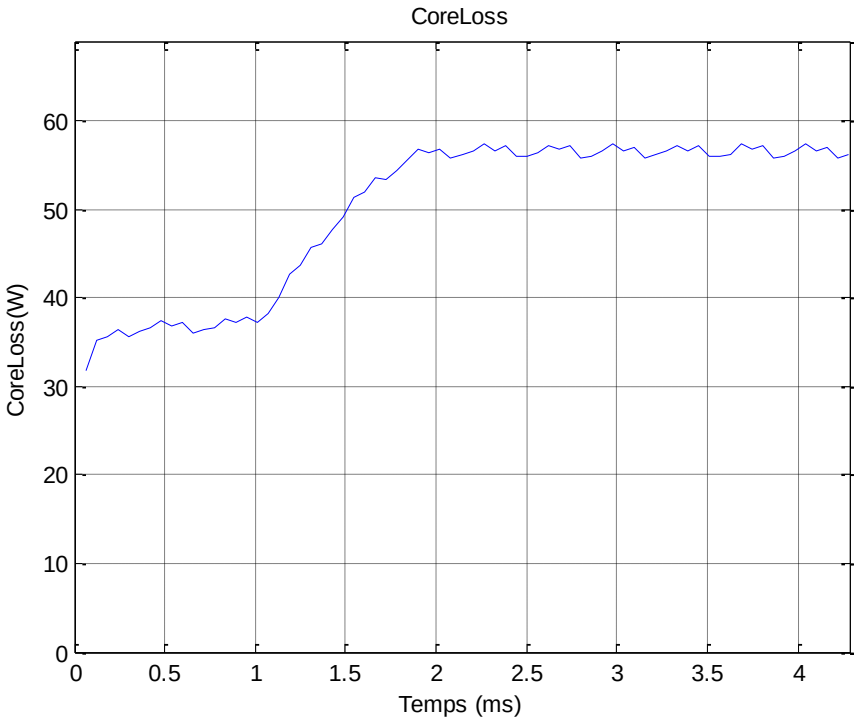

Figure 5: Core losses of the SM-PMSM

The eddy current losses of the SM-PMSM are presented in Figure 6.

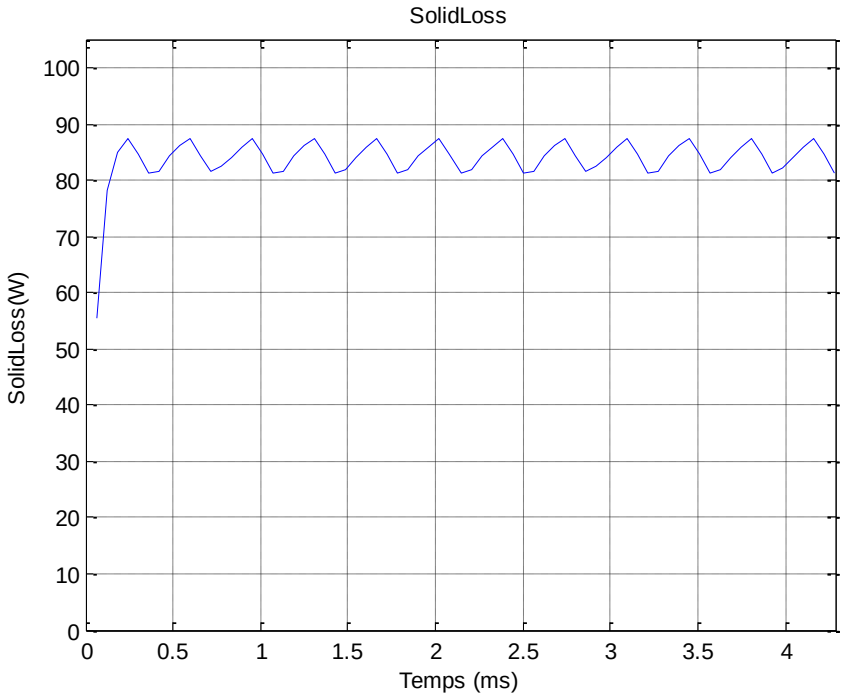

Figure 6: Eddy current losses in permanent magnets

The performances of 7-phases/7-slots/ 6-poles WRSM

The seven-phase windings are supplied with sinusoidal currents shown in Figure 7.

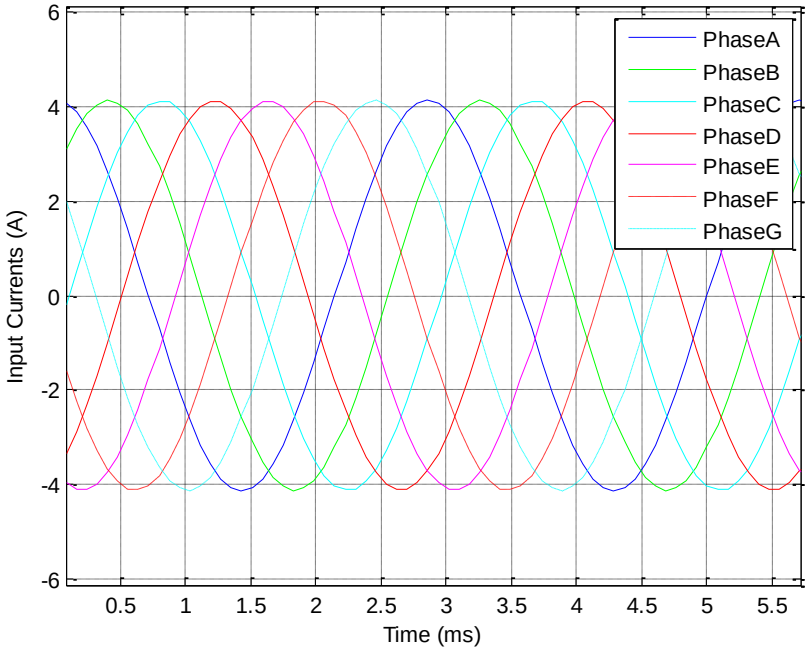

Figure 7: Input currents for 7-phase WRSM

The magnetic fluxes of different phases of WRSM are shown in Figure 8.

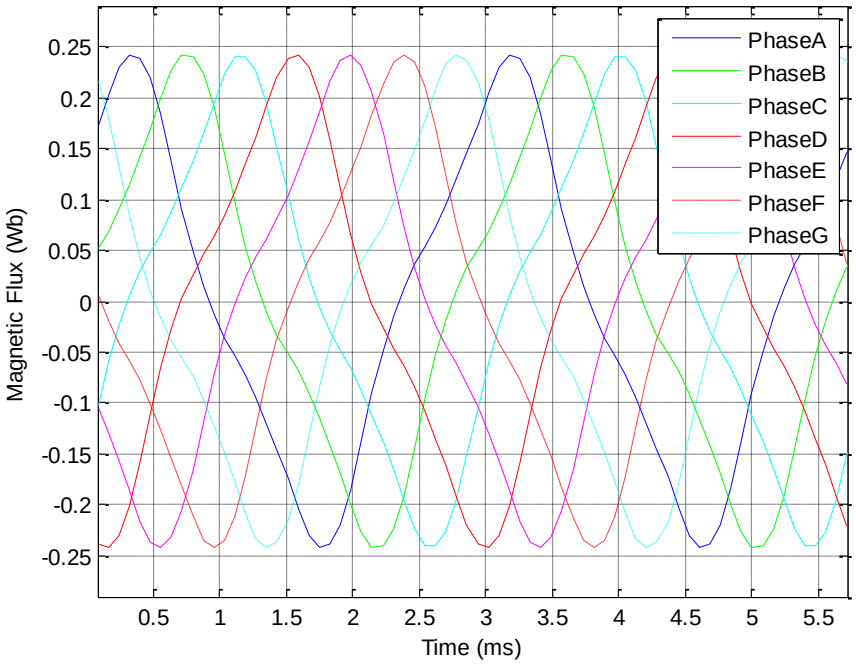

Figure 8: Magnetic flux of the designed WRSM

The induced voltages of seven-phase WRSM are shown in Figure 9.

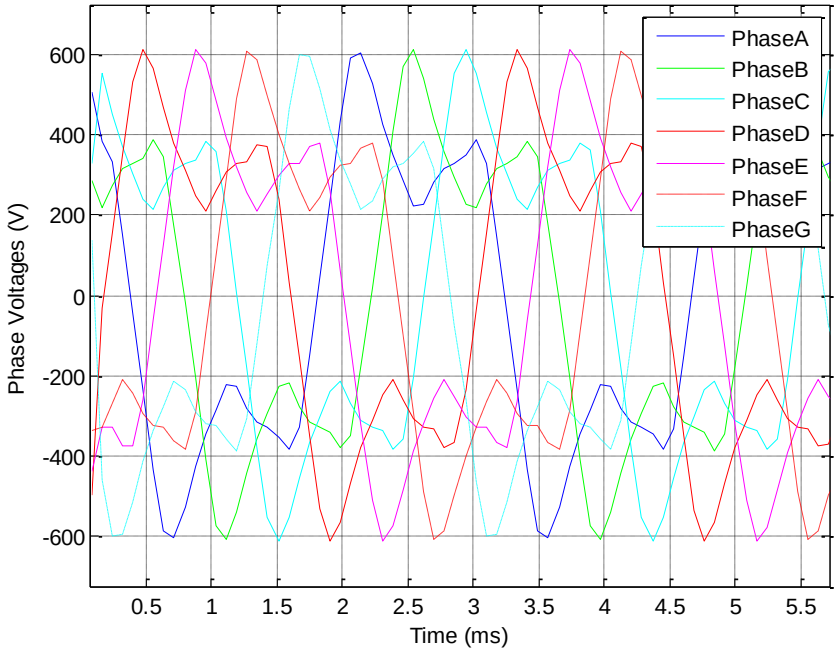

Figure 9: Induced voltages of the 7-phase WRSM

The electromagnetic torque of WRSM is shown in Figure 10.

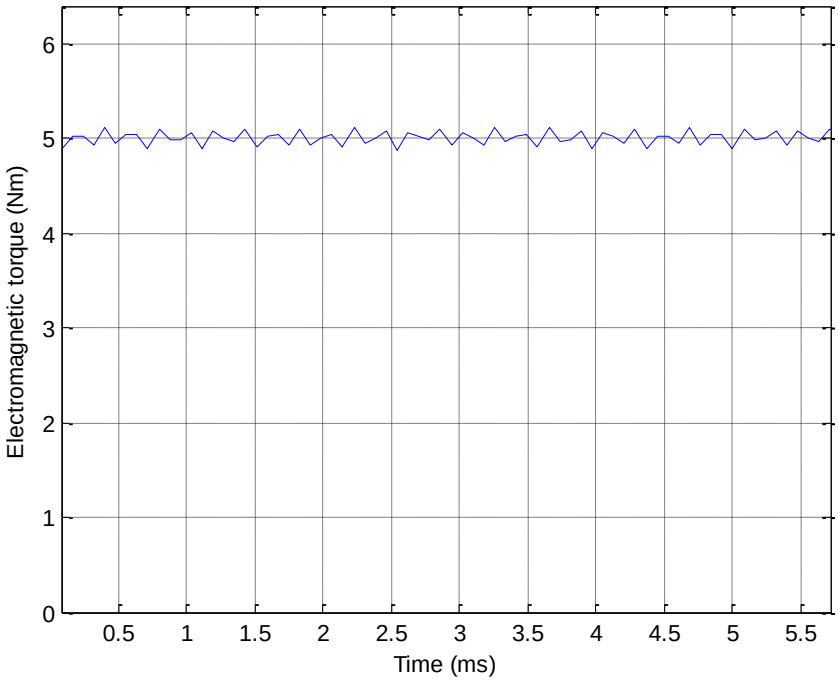

Figure 10: Electromagnetic torque of the WRSM

The core losses analyzed by 2D FE simulation are shown in Figure 11.

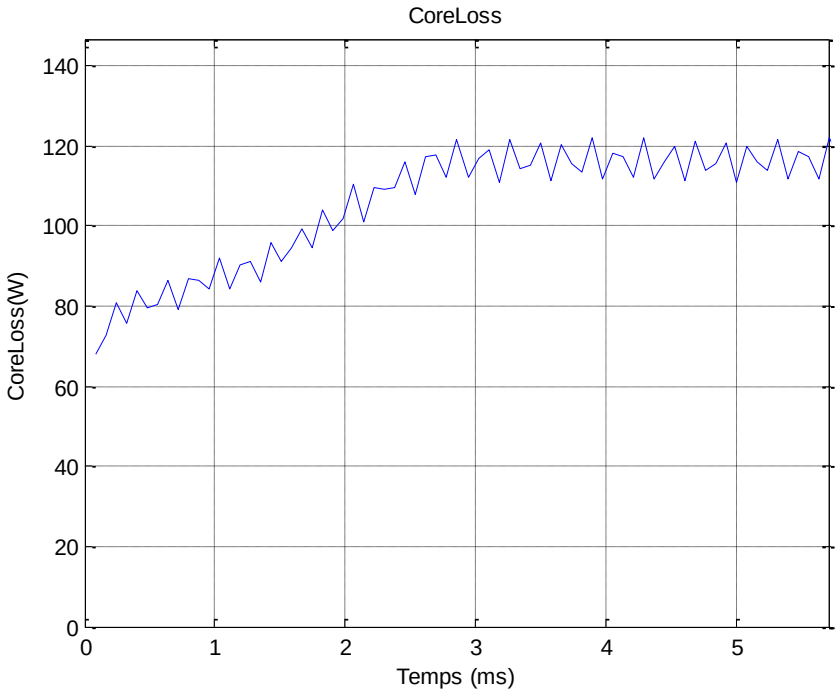

Figure 11: Core losses of the designed WRSM

Annex 2: Torque speed characteristics of SM-PMSM and WRSM

Assuming the limitation of the voltage source is about 370V, the numerical simulations for different operating points of SM-PMSM are carried out in order to estimate the machine performances shown in Table 1.

Table 1: SM-PMSM performances for different operating points

N (rpm)	**500**	**1000**	**2000**	**3000**	**4000**	**5000**	**6000**	**7000**	**8000**	**9000**	**10000**
I_s (A)	6.87	6.87	6.87	6.87	6.87	6.867	4.56	3.54	3.43	3.43	3.43
V_{rms} (V)	40.17	77.49	149.72	223.84	297.10	369.36	369.46	369.55	369.45	369.21	369.25
T_{em} (Nm)	7.09	7.09	7.089	7.07	7.04	7.01	5.83	5.00	4.37	3.36	1.64
P_{out} (kW)	0.37	0.74	1.48	2.22	2.95	3.67	3.66	3.667	3.66	3.17	1.72
P_{iron_s} (W)	2.69	5.79	13.19	22.16	32.73	45.02	43.04	42.51	43.54	45.35	47.11
P_{iron_r} (W)	0.05	0.08	0.71	0.32	0.61	0.61	0.34	0.33	0.43	0.34	0.14
P_{eddy} (W)	1.38	5.512	21.79	48.54	85.35	131.68	105.14	85.71	75.09	61.95	43.04
P_{copper_s} (W)	128.09	128.09	128.09	128.09	128.09	128.09	56.54	34.11	31.91	31.91	31.91
$Efficiency$ (%)	73.66	84.13	89.99	91.69	92.19	92.33	94.61	95.66	95.95	95.69	93.28
ΔT (%)	3.28	3.43	3.46	3.47	3.41	3.72	2.47	4.71	2.43	3.22	12.61

The machine performances of the WRSM for different operating points are shown in Table 2.

Table 2: WRSM performances for different operating points

N (rpm)	**500**	**1000**	**2000**	**3000**	**4000**	**5000**	**6000**	**7000**	**8000**	**9000**
I_s (A)	11.32	11.32	11.32	11.32	11.32	7.17	5.65	4.88	4.46	4.15
I_r (A)	4.13	4.13	4.13	4.13	4.13	3.273	3.07	2.97	2.85	2.79
V_{rms} (V)	39.02	76.36	149.81	223.31	296.78	369.25	369.63	369.43	369.90	369.69
T_{em} (Nm)	6.99	6.99	6.99	6.99	6.99	6.99	5.83	5.00	4.38	3.89
P_{out} (kW)	0.37	0.73	1.46	2.19	2.93	3.66	3.66	3.67	3.67	3.66
P_{iron_s} (W)	4.11	8.75	19.58	32.49	47.48	64.64	66.98	59.50	53.22	47.24
P_{iron_r} (W)	1.67	3.81	9.43	16.88	26.18	36.88	38.91	37.27	38.36	39.10
P_{copper_s} (W)	174.56	174.56	174.56	174.56	174.56	174.56	80.18	61.82	53.19	52.91
P_{copper_r} (W)	42.28	42.28	42.28	42.28	42.28	42.28	35.75	29.22	27.53	27.53
$Efficiency$ (%)	62.11	76.05	85.53	89.09	90.88	91.90	94.19	95.03	95.42	95.55
ΔT (%)	2.83	2.92	3.04	3.02	2.95	2.74	2.72	3.89	5.00	6.42

10000	4.11	2.74	369.67	3.31	3.47	43.04	41.51	52.91	27.53	95.37	6.60
11000	4.11	2.74	370.18	2.86	3.30	42.31	44.80	52.91	27.53	95.07	7.65
12000	4.11	2.74	369.37	2.25	2.83	40.11	46.95	52.91	27.53	94.31	8.19

Annex 3: Self and mutual inductances of the WRSM

In Figure 12, the characteristics of one stator winding (e.g. the fourth winding) of the prototype machine are shown.

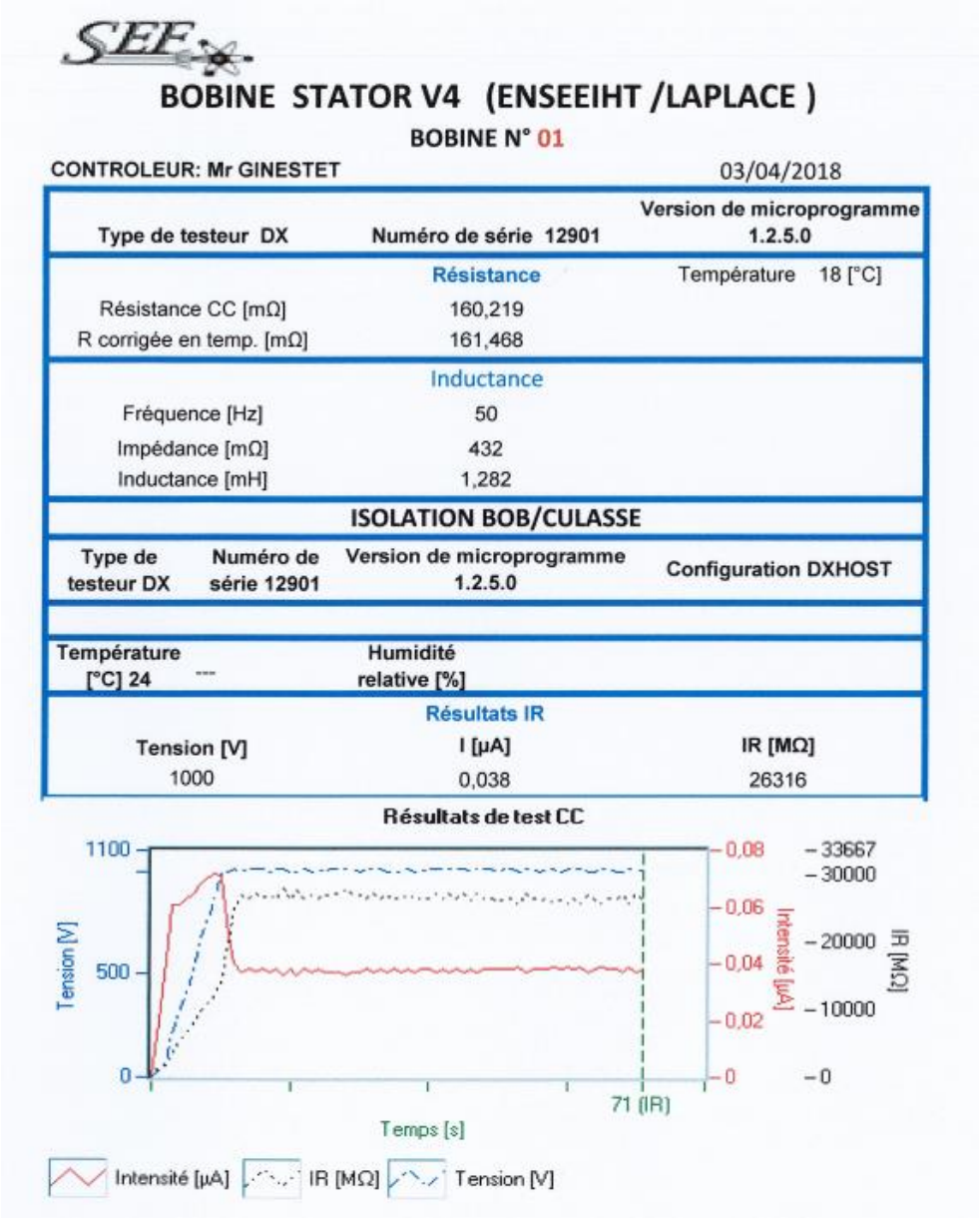

Figure 12: Characteristic of one stator winding

The values of self-inductance L_w of each stator winding in the prototype is shown in Table 3.

Table 3: Self-inductances of the armature windings in the prototype machine

Winding	1	2	3	4	5	6	7
L_w (mH)	1.282	1.272	1.269	1.274	1.271	1.268	1.278

Figure 13 shows the characteristic of one rotor winding (e.g. the first winding) of the prototype machine.

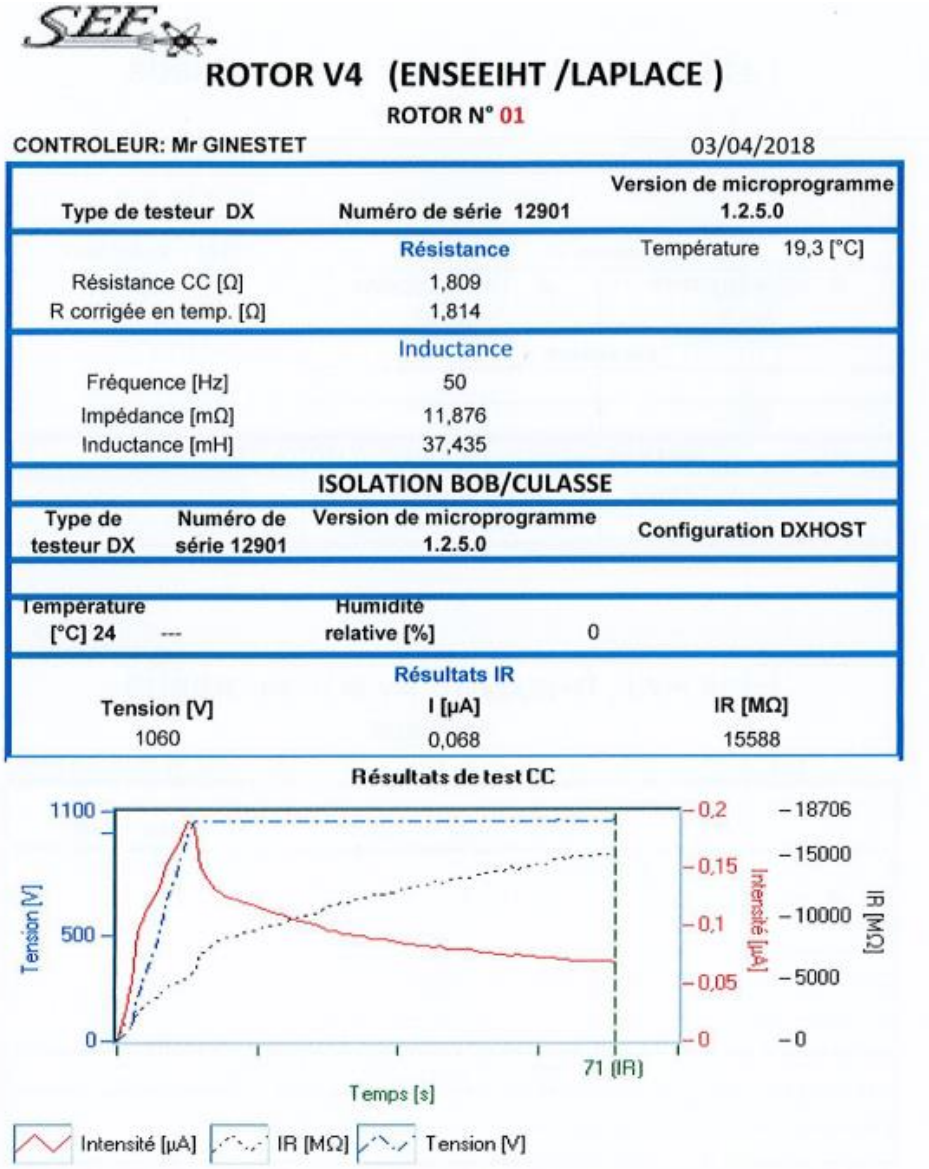

Figure 13: Characteristic of one rotor winding

FE simulations with the same number of parallel circuits, number of spires of two windings are carried out to find the self and mutual inductances of each winding. The self-inductance of rotor winding is about $30.2239mH$. The self-inductances of stator windings by using 2D FE analysis are shown in Table 4 and Figure 14.

Table 4: Self-inductances of stator windings using FE analysis

Winding	1	2	3	4	5	6	7
$\boldsymbol{L_w}$ $(\boldsymbol{mH})$	1.0277	1.0307	1.0299	1.0285	1.0288	1.0310	1.0291

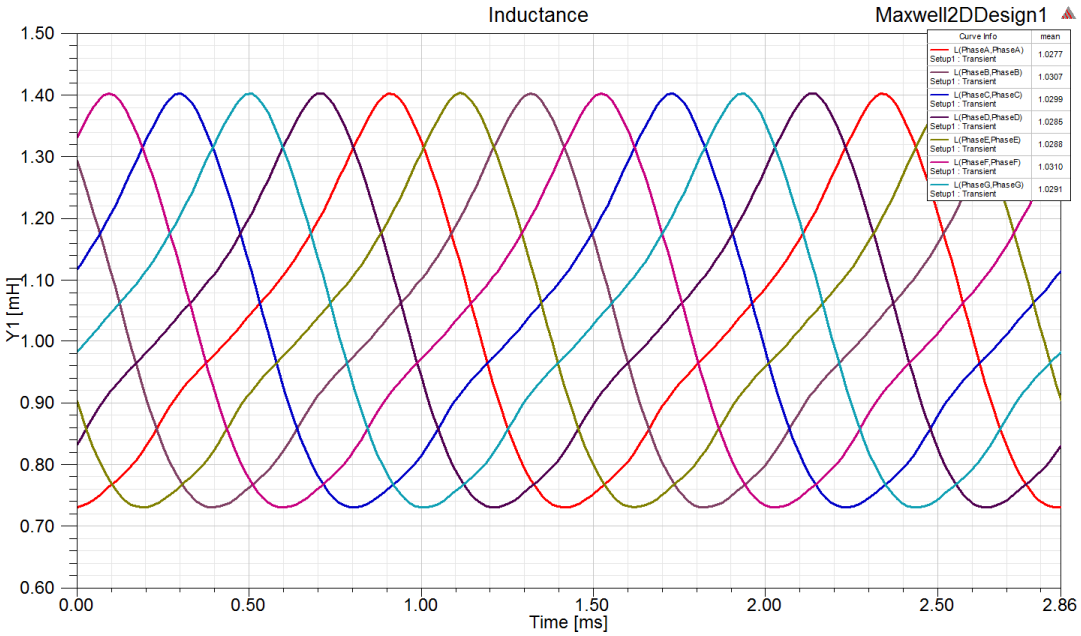

Figure 14: Self-inductances of stator windings using 2D FE analysis

The self-inductances of stator windings by using 3D FE analysis are shown in Table 5 and Figure 15.

Table 5: Self-inductances of stator windings using 3D FE analysis

Winding	1	2	3	4	5	6	7
L_w (mH)	1.2630	1.2655	1.2615	1.2617	1.2594	1.2595	1.2616

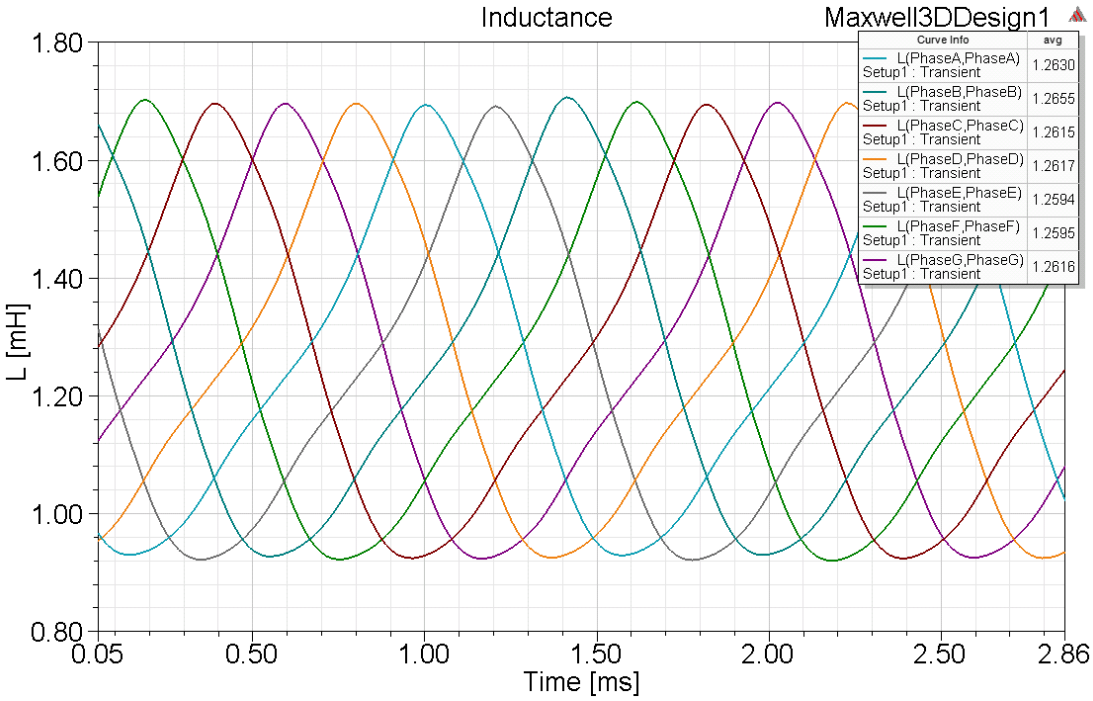

Figure 15: Self-inductances of stator windings using 3D FE analysis

Annex 4: Specifications

The specifications of the machine are:

- The rated speed is 7000rpm.
- The average torque is 5Nm.
- The torque ripple is lower than 5%.
- The coil temperature is lower than 105°C for ensuring the integration of power converters on the housing without cooling system.
- The peak value of the phase voltage is lower than 800V.
- The machine efficiency should be as high as possible.